DISSERTATION

NUCLEATION AND GROWTH STUDIES OF POLYCRYSTALLINE COVALENT MATERIALS

Submitted by

Jungheum Yun

Department of Chemical Engineering

In partial fulfillment of the requirements

For the Degree of Doctor of Philosophy

Colorado State University

Fort Collins, Colorado

Fall 2003

Reproduced with permission of the copyright owner. Further reproduction prohibited without permission.

UMI Number: 3114706

INFORMATION TO USERS

The quality of this reproduction is dependent upon the quality of the copy submitted. Broken or indistinct print, colored or poor quality illustrations and photographs, print bleed-through, substandard margins, and improper alignment can adversely affect reproduction.

In the unlikely event that the author did not send a complete manuscript and there are missing pages, these will be noted. Also, if unauthorized copyright material had to be removed, a note will indicate the deletion.

UMI Microform 3114706

Copyright 2004 by ProQuest Information and Learning Company.
All rights reserved. This microform edition is protected against unauthorized copying under Title 17, United States Code.

ProQuest Information and Learning Company
300 North Zeeb Road
P.O. Box 1346
Ann Arbor, MI 48106-1346

Reproduced with permission of the copyright owner. Further reproduction prohibited without permission.

COLORADO STATE UNIVERSITY

June 25, 2003

WE HEREBY RECOMMED THAT THE DISSERTATION PREPARED UNDER OUR SUPERVISION BY JUNGHEUM YUN ENTITLED NUCLEATION AND GROWTH STUDIES OF POLYCRYSTALLINE COVALENT MATERIALS BE ACCEPTED AS FULFILLING IN PART REQUIREMENTS FOR THE DEGREE OF DOCTOR OF PHILOSOPHY

Committee on Graduate Work

____

____

____

____

____
Advisor

____
Department Head

Reproduced with permission of the copyright owner. Further reproduction prohibited without permission.

ABSTRACT OF DISSERTATION

NUCLEATION AND GROWTH STUDIES OF POLYCRYSTALLINE COVALENT MATERIALS

The chemical vapor deposition of different covalent polycrystalline materials—including diamond, silicon carbide, and carbon nitride—in stagnation flow reactors was rigorously simulated to determine the nucleation and growth mechanisms of these materials. Kinetic models were used to predict the rates of gas-phase and surface chemistry, the temperature and velocity profiles, potential gaseous film growth precursors, the time evolution of nucleation and intermediate layer formation, and the morphological evolution of continuous polycrystalline films. Numerical studies were also carried out to determine the dependence of the kinetics of nucleation and subsequent polycrystalline film growth on operating conditions.

The calculated results for carbon nitride deposition indicate that the experimentally measured bond types in the carbon nitride films must result from chemical bond rearrangement occurring on the deposition surface or in the bulk phase once gaseous film growth precursors, including C, CH_2, CH_3, C_2H_2, N, NH, NH_2, HCN, and H_2CN, are adsorbed. Of these precursors, C and CH_3 dominate the carbon contribution to carbon nitride film growth, and atomic nitrogen is the principal nitrogen bearing species. When

Reproduced with permission of the copyright owner. Further reproduction prohibited without permission.

the evolution rates of a silicon carbide intermediate layer and diamond clusters are calculated by accounting for gas-phase and surface reactions, surface and bulk diffusion, the mechanism for intermediate layer formation, and heterogeneous diamond nucleation kinetics, it is predicted that higher adsorption energies, in the range of 3.7 to 4.5 eV, lead to larger surface adatom densities, lower saturated nucleation densities, and larger silicon carbide intermediate layer thicknesses. The intermediate layer thickness becomes saturated while the growing diamond nuclei still cover a very small fraction of the silicon carbide. Reports of heteroepitaxial diamond nucleation without silicon carbide intermediate layer formation may be readily explained by a significant decrease in the intermediate layer thickness at lower substrate temperatures and at higher diamond nucleation densities. Further, the results of the morphology evolution model reveal that the crystallographic texture and surface morphology—surface roughness, film texture, and grain size—of polycrystalline silicon carbide films, as well as diamond films deposited on the silicon carbide layer, are strongly dependent upon the saturated nucleation density, the deposition condition, and film thickness.

Jungheum Yun
Chemical Engineering
Colorado State University
Fort Collins, CO 80523
Fall 2003

Reproduced with permission of the copyright owner. Further reproduction prohibited without permission.

ACKNOWLEDGEMENTS

There are many people I would like to thank for a huge variety of reasons. This work could not have been possible without the support and encouragement of my teachers, colleagues, friends, and family. I would like to express my largest gratitude to my advisor, Dr. David S. Dandy for his advice and encouragement throughout my graduate study. He displayed incredible patience as my study was progressing slowly by my personal struggles. I would like to express great thanks to Dr. A. Ted Watson, Dr, Bruce Parkinson, and Dr. Laurence Belfiore for serving on my committee. I have to give much respect to Dr. Gray Y. Robinson for his teaching and advice. Thanks also to my ex-boss, Dr. Nancy Boldt, for giving me a teaching job that kept me surviving in the harsh world. I was so fortunate to have great colleagues and friends. I am grateful to my officemates, Mr. Te-Hsin Wu, Dr. William Wangard, III, Mr. Toshihiro Asai, and Mr. Derek Johnson for providing a healing touch and a fun environment. Thanks especially Wu for answering my numerous computer questions. Thanks also to all of Korean friends for that serious discussion and all those coffees. Lastly, and most importantly, I wish to thank my family for supporting and loving me. The support of my wife, Cinthia Chong, was truly invaluable through this work.

Reproduced with permission of the copyright owner. Further reproduction prohibited without permission.

TABLE OF CONTENTS

1 Background **1**

1.1 Introduction 1

1.2 Crystal Structure 3

1.3 Nucleation and Continuous Growth of Polycrystalline Covalent Materials 6

1.3.1 Gas-phase and Surface Chemistries 7

1.3.2 Heterogeneous Nucleation and Intermediate Layer Formation . . . 8

1.3.3 Epitaxial Growth and Morphology Evolution 10

1.4 Research Objectives 11

1.5 Organization of the Dissertation 14

1.6 References 16

2 Analysis of carbon nitride growth in pedestal reactors by chemical vapor deposition **18**

2.1 Introduction 18

2.2 Model Description 24

2.3 Results and Discussion 29

2.3.1 Correlation between Gas and Solid Bond Types 30

2.3.2 Identification of Probable Growth Precursors 36

2.3.3 Effects of Operating Conditions 40

2.4 Conclusion 55

Reproduced with permission of the copyright owner. Further reproduction prohibited without permission.

2.5 References 59

3 A kinetic model of diamond nucleation and silicon carbide interlayer formation during chemical vapor deposition **64**

3.1 Introduction 64

3.2 Model Description 70

3.3 Results and Discussion 82

3.4 Conclusion 98

3.5 References 101

4 A model of morphology evolution in the growth of polycrystalline β-SiC films **108**

4.1 Introduction 108

4.2 Model Description 111

4.3 Results and Discussion 112

4.3.1 Simulations of Film Growth Rate 112

4.3.2 Simulations of Surface Morphology Evolution 115

4.4 References 121

5 A morphological study of diamond films deposited on pretreated Si substrates **123**

5.1 Introduction 123

5.2 Model Description 128

5.3 Results and Discussion 131

5.3.1 Diamond Nucleation Process 132

5.3.2 Continuous Film Growth Process 145

Reproduced with permission of the copyright owner. Further reproduction prohibited without permission.

5.4 Conclusion 154

5.5 References 159

6 Conclusions and recommendations **164**

6.1 Overall Conclusions 164

6.1.1 Analysis of Carbon Nitride Growth in Pedestal Reactors by Chemical Vapor Deposition 165

6.1.2 A Kinetic Model of Diamond Nucleation and Silicon Carbide Interlayer Formation during Chemical Vapor Deposition 166

6.1.3 A Model of Morphology Evolution in the Growth of Polycrystalline β-SiC Films 167

6.1.4 A Morphological Study of Diamond Films Deposited on Pretreated Si Substrates 169

5.2 Recommendations for Future Research 170

Reproduced with permission of the copyright owner. Further reproduction prohibited without permission.

LIST OF FIGURES

1.1 3-dimnesional lattice structure of diamond showing the tetrahedral bond arrangement. 3

1.2 Crystal lattice structures comprising both β- and 6H-SiC. 4

1.3 Structure of β-C3N4 in the x-y plane. The hexagonal unit cell is shown in the parallelogram and contains two formula units (14 atoms) with local order such that C atoms occupy slightly distorted tetrahedral sites while N atoms sit in nearly planar triply coordinated sites. 5

1.4 Critical features of the intermediate layer formation and the early stage of diamond nucleation. 10

2.1 Schematic diagram of the CVD geometry considered. The geometry of the system is represented in terms of the cylindrical coordinates (r, ϕ, z). . . 25

2.2a Film growth rates due to potential gaseous film growth precursors, CH_x (x = 0,2,3) and C_2H_2. 38

2.2b Film growth rates due to potential gaseous film growth precursors, NH_x (x = 0-2) and H_xCN (x = 1,2). 39

2.3a Mole fractions of potential gaseous film growth precursors at the deposition surface corresponding to the operating conditions: T_∞ = 2400 K; T_s = 1200 K; P = 0.76 Torr; L = 10 cm; U = 1.0 cm/s and inlet mole

Reproduced with permission of the copyright owner. Further reproduction prohibited without permission.

fractions: $X_{H\infty} + X_{H_2\infty} = 0.98$; $X_{NH_3\infty} = 1.667\times10^{-2}$; $X_{CH_4\infty} = 3.33\times10^{-3}$. Calculations were performed for five different H inlet mole fractions: 0.05, 0.10, 0.15, 0.20, and 0.25. Graph shows mole fractions of potential gaseous film growth precursors, CH_x ($x = 0,2,3$) and C_2H_2. 43

2.3b Mole fractions of potential gaseous film growth precursors at the deposition surface corresponding to the operating conditions: $T_\infty = 2400$ K; $T_s = 1200$ K; $P = 0.76$ Torr; $L = 10$ cm; $U = 1.0$ cm/s and inlet mole fractions: $X_{H\infty} + X_{H_2\infty} = 0.98$; $X_{NH_3\infty} = 1.667\times10^{-2}$; $X_{CH_4\infty} = 3.33\times10^{-3}$. Calculations were performed for five different H inlet mole fractions: 0.05, 0.10, 0.15, 0.20, and 0.25. Graph shows mole fractions of potential gaseous film growth precursors, NH_x ($x = 0$-2) and H_xCN ($x = 1,2$). 44

2.4a Mole fractions of potential gaseous film growth precursors at the deposition surface corresponding to the operating conditions described in Figure 1.3, with five different inlet molecule ratios of NH_3 to CH_4: 0.2, 0.6, 1.0, 3.0, and 5.0. Graph shows mole fractions of potential film growth precursors, CH_x ($x = 0,2,3$) and C_2H_2. 46

2.4b Mole fractions of potential gaseous film growth precursors at the deposition surface corresponding to the operating conditions described in Figure 1.3, with five different inlet molecule ratios of NH_3 to CH_4: 0.2, 0.6, 1.0, 3.0, and 5.0. Graph shows mole fractions of potential film growth precursors, NH_x ($x = 0$-2) and H_xCN ($x = 1,2$). 47

Reproduced with permission of the copyright owner. Further reproduction prohibited without permission.

2.5a Mole fractions of potential gaseous film growth precursors at the deposition surface corresponding to the operating conditions described in Figure 1.3. Calculations were performed for six different inlet mole fractions of ($H + H_2$, $NH_3 + CH_4$): (0.998, 0.002), (0.98, 0.02), (0.74, 0.26), (0.50, 0.50), (0.26, 0.74), and (0.02, 0.98). Graph shows mole fractions of potential film growth precursors, CH_x (x = 0,2,3) and C_2H_2. 48

2.5b Mole fractions of potential gaseous film growth precursors at the deposition surface corresponding to the operating conditions described in Figure 1.3. Calculations were performed for six different inlet mole fractions of ($H + H_2$, $NH_3 + CH_4$): (0.998, 0.002), (0.98, 0.02), (0.74, 0.26), (0.50, 0.50), (0.26, 0.74), and (0.02, 0.98). Graph shows mole fractions of potential film growth precursors, NH_x (x = 0-2) and H_xCN (x = 1,2). 49

2.6a Mole fractions of potential gaseous film growth precursors at the deposition surface corresponding to the operating conditions described in Figure 1.3. Calculations were performed for three different reactor pressure values: 0.76, 7.6, and 76 Torr. Graph shows mole fractions of potential film growth precursors, CH_x (x = 0,2,3) and C_2H_2. 51

2.6b Mole fractions of potential gaseous film growth precursors at the deposition surface corresponding to the operating conditions described in Figure 1.3. Calculations were performed for three different reactor pre-

Reproduced with permission of the copyright owner. Further reproduction prohibited without permission.

ssure values: 0.76, 7.6, and 76 Torr. Graph shows mole fractions of potential film growth precursors, NH_x (x = 0-2) and H_xCN (x = 1,2). . . 52

2.7a Mole fractions of potential gaseous film growth precursors at the deposition surface corresponding to the operating conditions described in Figure 1.3, with two different substrate temperature: 300 and 1200 K. Graph shows mole fractions of potential growth precursors, CH_x (x = 0,2,3) and C_2H_2. 53

2.7b Mole fractions of potential gaseous film growth precursors at the deposition surface corresponding to the operating conditions described in Figure 1.3, with two different substrate temperature: 300 and 1200 K. Graph shows mole fractions of potential growth precursors, NH_x (x = 0-2) and H_xCN (x = 1,2). 54

3.1 Saturated surface density of stable diamond nuclei, N_s, for different adsorption energies E_a = 1.43 to 4.61 eV and substrate temperatures T_s = 1000 and 1200 K. 85

3.2a Saturated surface density of adsorbed carbon atoms, $n_{1,s}$, and time required to reach saturation, t_s, for different values of T_s, X_{CH_4}, and E_a. Figure shows $n_{1,s}$ vs. E_a for T_s = 1000 and 1200 K. 87

3.2b Saturated surface density of adsorbed carbon atoms, $n_{1,s}$, and time required to reach saturation, t_s, for different values of T_s, X_{CH_4}, and E_a. Figure shows $n_{1,s}$ vs. E_a for X_{CH_4} = 0.005, 0.01, 0.02, and 0.04. 88

Reproduced with permission of the copyright owner. Further reproduction prohibited without permission.

3.2c Saturated surface density of adsorbed carbon atoms, $n_{1,s}$, and time required to reach saturation, t_s, for different values of T_s, X_{CH_4}, and E_a. Figure shows t_s vs. E_a for T_s = 1000 and 1200 K. 89

3.2d Saturated surface density of adsorbed carbon atoms, $n_{1,s}$, and time required to reach saturation, t_s, for different values of T_s, X_{CH_4}, and E_a. Figure shows t_s vs. E_a for X_{CH_4} = 0.005, 0.01, 0.02, and 0.04. 90

3.3 Time evolution of the intermediate layer for E_a = 1.73, 3.45, and 4.61eV during a 1 h deposition time. Operating conditions are T_s = 1200 K and X_{CH_4} = 0.01. 92

3.4 Dependence of the time evolution of the intermediate layer on T_s and X_{CH_4} for E_a = 3.45 eV during a 1 h deposition time. Operating conditions are (a) T_s = 1000 K and X_{CH_4} = 0.01, (b) T_s = 1200 K and X_{CH_4} = 0.005, (c) T_s = 1200 K and X_{CH_4} = 0.01, and (d) T_s = 1200 K and X_{CH_4} = 0.04. 94

3.5 Dependence of the time evolution of the intermediate layer on T_s and X_{CH_4} for E_a = 4.61 eV during a 1 h deposition time corresponding to the operating conditions described in Figure 3.4. 95

3.6 Competition in rates associated with intermediate layer growth and surface coverage of growing diamond nuclei for E_a = 3.45 and 4.61 eV. Operating conditions are T_s = 1200 K and X_{CH_4} = 0.02. 97

Reproduced with permission of the copyright owner. Further reproduction prohibited without permission.

4.1 Growth rate of β-SiC film as a function of the substrate temperature for operating conditions: inlet gas temperature T_{inlet} = 300 K; reactor pressure P = 760 Torr; inlet axial velocity U_{inlet} = 2.49 cm/s; distance between the inlet and the substrate surface L = 3 cm, and inlet mole fractions: $X_{H_2} = 0.9964$; $X_{SiH_4} = 2\times10^{-4}$; $X_{C_3H_8} = 1.6\times10^{-4}$. 114

4.2 Film morphology predicted by two-dimensional numerical model. The average distance between nucleated seed crystals is represented as d_0. Figures (a) and (b) show the relatively thin film (thickness = 10 d_0) morphologies for two different growth parameter values: (a) α_{2D} = 1.0 and (b) α_{2D} = 1.95. Figures (c) and (d) show the relatively thick film (thickness = 260 d_0) morphologies for two different growth parameter values: (c) α_{2D} = 1.0 and (d) α_{2D} = 1.95. 116

4.3 Surface roughness prediction for different film thickness and α_{2D} values. . 117

4.4a Evolutions of the relative sizes of the <10> and <11>-orientated grains with the film thickness when α_{2D} = 1.95. 119

4.4b Evolutions of the average grain size with the film thickness when α_{2D} = 1.95. 120

5.1 Formation time of the β-SiC layer as a function of the substrate temperature for two different hydrocarbon adsorption energies, 3.9 and 4.5 eV, under HFCVD operating conditions conductive to diamond nucleation, as listed in Table 5.1. 134

5.2 Saturated nucleation density as a function of the substrate temperature for three different pretreated Si substrates, including the stepped β-SiC

Reproduced with permission of the copyright owner. Further reproduction prohibited without permission.

layer with W_t = 1 μm, the flat β-SiC layer with E_a = 4.5 eV, and the flat β-SiC layer with E_a = 3.9 eV. 135

5.3 Growth velocity of {10} face, V_{10}, determined for different substrate temperatures and inlet gas compositions under the operating conditions corresponding to Figure 5.1. 137

5.4 Mean surface roughness as a function of film thickness for different saturated nucleation densities and growth rate parameters listed in Table 5.2. 139

5.5 Average peak-to-valley height as a function of film thickness for the film growth conditions corresponding to Figure 5.4. 141

5.6 Relative grain size ratio <10>/<11> as a function of film thickness for the film growth conditions corresponding to Figure 5.4. 143

5.7 Average grain size as a function of film thickness for the film growth conditions corresponding to Figure 5.4. 144

5.8a Mean surface roughness of films grown during the film growth stage as a function of overall film thickness up to 100 μm. Plot show the mean surface roughness for different growth-rate parameters, α_{2D} = 1.3, 1.6, and 1.9, at a fixed L_t value of 1 μm. 147

5.8b Mean surface roughness of films grown during the film growth stage as a function of overall film thickness up to 1700 μm. Plot show the mean surface roughness for different growth-rate parameters, α_{2D} = 1.3, 1.6, and 1.9, at a fixed L_t value of 1 μm. 148

Reproduced with permission of the copyright owner. Further reproduction prohibited without permission.

5.8c Mean surface roughness of films grown during the film growth stage as a function of overall film thickness up to 100 μm. Plot display the mean surface roughness for different underlying diamond film thicknesses, L_t = 1, 10, and 50 μm, at a fixed α_{2D} value of 1.9. 150

5.8d Mean surface roughness of films grown during the film growth stage as a function of overall film thickness up to 1700 μm. Plot display the mean surface roughness for different underlying diamond film thicknesses, L_t = 1, 10, and 50 μm, at a fixed α_{2D} value of 1.9. 151

5.9a Average grain size of films grown during the film growth stage as function of overall film thickness up to 100 μm. Plot show the mean surface roughness for different growth-rate parameters, α_{2D} = 1.3, 1.6, and 1.9, at a fixed L_t value of 1 μm. 152

5.9b Average grain size of films grown during the film growth stage as function of overall film thickness up to 1200 μm. Plot show the mean surface roughness for different growth-rate parameters, α_{2D} = 1.3, 1.6, and 1.9, at a fixed L_t value of 1 μm. 153

5.9c Average grain size of films grown during the film growth stage as function of overall film thickness up to 100 μm. Plot display the mean surface roughness for different underlying diamond film thicknesses, L_t = 1, 10, and 50 μm, at a fixed α_{2D} value of 1.9. 155

5.9d Average grain size of films grown during the film growth stage as function of overall film thickness up to 1200 μm. Plot display the mean surface

Reproduced with permission of the copyright owner. Further reproduction prohibited without permission.

roughness for different underlying diamond film thicknesses, L_t = 1, 10, and 50 μm, at a fixed α_{2D} value of 1.9. 156

Reproduced with permission of the copyright owner. Further reproduction prohibited without permission.

LIST OF TABLES

1.1 Comparison of the physical and electronic properties of diamond and SiC with conventional semiconductor materials. 2

2.1 Gas-phase reaction mechanisms for C/N/H gas mixtures. 28

2.2 Surface reaction mechanisms for presumed β-C_3N_4 film growth precursors. 29

2.3 Experimental conditions of Ricci et al. used in the model. 31

2.4 Mole fractions and mass fluxes of presumed film growth precursors at the deposition surface. 31

2.5 Operating conditions chosen to simulate the experiments of Zhang et al. . . 36

3.1 Simplified surface reaction mechanism for atomic hydrogen adsorption and abstraction on Si surface radical sites. 76

3.2 Adsorption energies and surface residence times of CH_3 and C_2H_2 for Si (100) and β-SiC (100) surfaces. 77

3.3 Operating conditions used in the present calculations. 83

3.4 Calculated mole fractions of predominant gaseous hydrocarbon species at the deposition surface and overall absorption rate of carbon atoms. . . . 84

4.1 Simplified surface reaction mechanism for β-SiC growth 113

5.1 Operating conditions used in diamond nucleation and continuous film growth stages. 132

Reproduced with permission of the copyright owner. Further reproduction prohibited without permission.

5.2 The calculated maximum mean surface roughness R_m and film thickness L_m corresponding to the saturated nucleation density N_s and growth-rate parameter α_{2D}, which are predicted by applying different combinations of film growth conditions. 138

Reproduced with permission of the copyright owner. Further reproduction prohibited without permission.

Chapter 1

BACKGROUND

1.1 Introduction

Novel covalent materials—including diamond, silicon carbide, and carbon nitride—have been received a great deal of attention because of their unique chemical, physical, and electronic properties. Of the different covalent materials, diamond exhibits very attractive properties including extreme hardness, high thermal conductivity, excellent infrared transparency, and other notable semiconductor properties [1-3]. Silicon carbide has received attention as a wide band-gap semiconductor material that gives great promise for use in high-temperature, high-power, high-frequency applications because of its excellent properties. These properties include a high melting point, relatively large band gap energy, high-saturated electron drift velocity, high breakdown field, high thermal conductivity, and chemical resistance against oxidation and radiation [4,5]. These properties, which are lacking in conventional semiconductor materials such as Si and GaAs, would improve performance capabilities in a variety of potential silicon carbide electronic device uses. Comparison of the physical and electronic properties of diamond and SiC with conventional semiconductor materials is given in Table 1.1.

Since Liu and Cohen [6,7] predicted theoretically the extreme hardness of β-C_3N_4, a type of crystalline carbon nitride, to be comparable to or greater than that of diamond, in

Reproduced with permission of the copyright owner. Further reproduction prohibited without permission.

Table 1.1 Comparison of the physical and electronic properties of diamond and SiC with conventional semiconductor materials [4].

Property	Si	GaAs	β-SiC (6H-SiC)	Diamond
Bandgap (ev) at 300 K	1.1	1.4	2.2 (2.9)	5.5
Maximum operating temperature (°C)	300	460	873 (1240)	1100(?)
Melting point (°C)	1420	1238	Sublimes (>1800)	Phase Change
Physical stability	Good	Fair	Excellent	Very good
Electron mobility ($cm^2/V{\cdot}s$)	1400	8500	1000 (600)	2200
Hole mobility ($cm^2/V{\cdot}s$)	600	400	40	1600
Breakdown voltage (10^6 V/cm)	0.3	0.4	4	10
Thermal conductivity (W/cm·°C)	1.5	0.5	5	20
Electron mobility ($cm^2/V{\cdot}s$)	1400	8500	1000 (600)	2200
Hole mobility ($cm^2/V{\cdot}s$)	600	400	40	1600
Breakdown voltage (10^6 V/cm)	0.3	0.4	4	10

the last decade there have been considerable efforts to synthesize the material. Besides the predicted hardness of β-C_3N_4, it may also have other potential applications in the field of low-compressibility materials and thermal conductors because of its short bond length, large band gap, and high atomic density [8].

As potential applications of diamond, silicon carbide, and carbon nitride are continuously discovered, it may be anticipated that the ultimate economic impact of the emerging covalent materials on the defense, space, and commercial areas will exceed that of conventional semiconductor materials. However, the difficulty in controlling the growth of high quality material has far limited the use of covalent materials in potential

Reproduced with permission of the copyright owner. Further reproduction prohibited without permission.

applications although the materials provide the extremes of many technologically important properties.

1.2 Crystal Structure

A comprehensive understanding of material growth processes necessitates detailed knowledge of atomic and crystal structures of the covalent materials. Diamond has a face centered cubic (fcc) lattice crystal structure. In the structure, each carbon atom is tetrahedrally coordinated, forming strong σ bonds to its four neighbors using hybrid sp^3 atomic orbitals. Each tetrahedron joins with four other tetrahedral forming strongly bonded, uniform, three-dimensional, and entirely covalent crystalline structure, as shown in Figure 1.1.

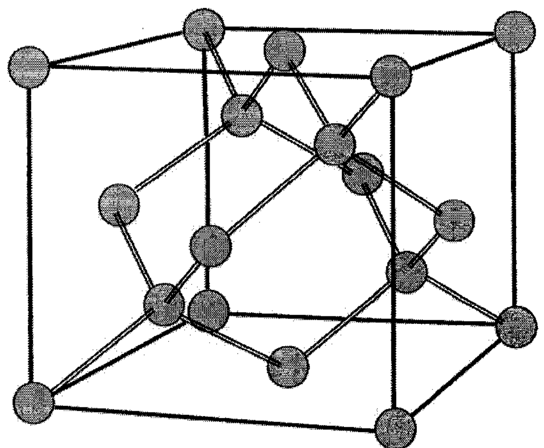

Figure 1.1 Three-dimensional lattice structure of diamond showing the tetrahedral bond arrangement.

The cubic structure of β-SiC results when silicon atoms are placed on one fcc lattice and carbon atoms on the other fcc lattice in the diamond structure. The coordinates of the silicon atoms in the fcc lattice are 000; $0\frac{1}{2}\frac{1}{2}$; $\frac{1}{2}0\frac{1}{2}$; $\frac{1}{2}\frac{1}{2}0$; the coordinates of the carb-

Reproduced with permission of the copyright owner. Further reproduction prohibited without permission.

on atoms are $\frac{1}{4}\frac{1}{4}\frac{1}{4}$; $\frac{1}{4}\frac{3}{4}\frac{3}{4}$; $\frac{3}{4}\frac{1}{4}\frac{3}{4}$; $\frac{3}{4}\frac{3}{4}\frac{1}{4}$. There are four molecules of SiC per conventional cell. However, 6H-SiC has a hexagonal closed-packed (hcp) lattice. The SiC tetrahedral structures comprising both the cubic and the hexagonal crystal lattices are shown in Figure 1.2. The fcc and hcp structures of different SiC polytypes are made of

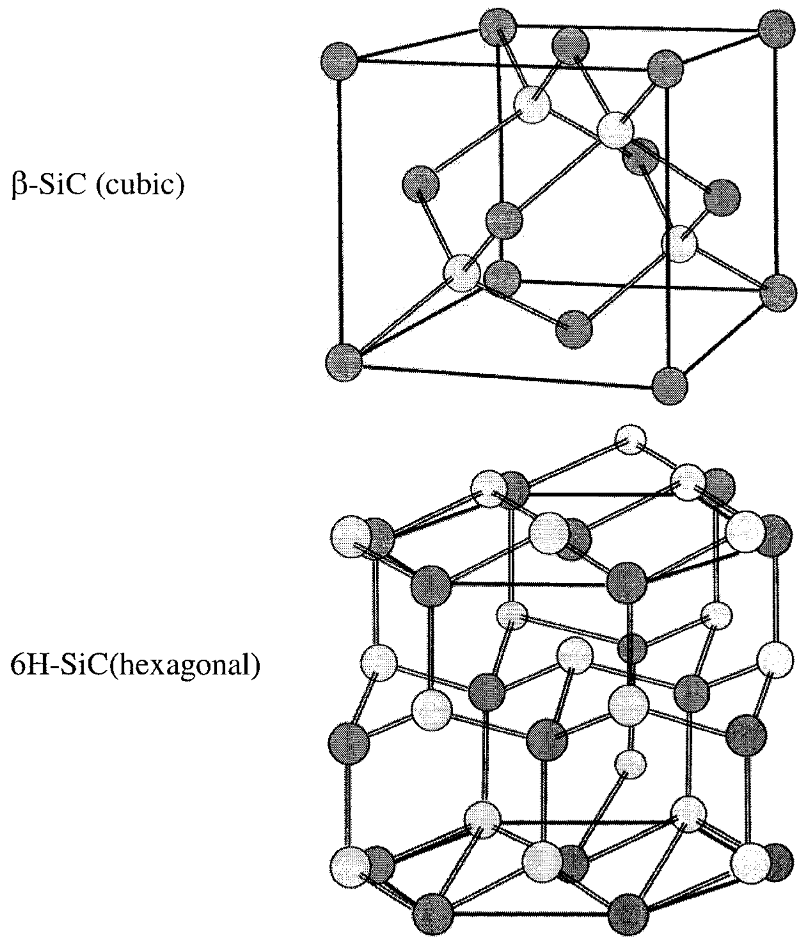

Figure 1.2 Crystal lattice structures comprising both β- and 6H-SiC.

close-packed planes of atoms. Polytypes are alike in the two dimensions of the close packed planes but differ in the stacking sequence in the dimension perpendicular to these planes. The polytypes of SiC differ from one another only in the stacking sequence of double layers of Si and C atoms. Each double layer consists of a plane of closed-packed

Reproduced with permission of the copyright owner. Further reproduction prohibited without permission.

Si atoms over a plane of closed-packed C atoms; one Si atom lies directly over each C atom in a double layer. Each successive double layer is stacked on a previous double layer with a close-packed arrangement. The arrangement allows for the three possible relative positions (A, B, and C) for the double layers, and several structures–including cubic, hexagonal, and rhombohedral–are produced from the stacking sequence. If the pure ABC stacking is repetitive, one obtains the cubic SiC called 3C-SiC or β-SiC, where the 3 refers to the number of the planes in the periodic sequence necessary to describe the unit cell. The hexagonal sequence (ABCACB...) is found to be 6H-SiC. Furthermore, more than 170 polytypes are identified, and all of these noncubic structures are known collectively as α-SiC [4].

The structure of β-C_3N_4 is expected to be similar to that of β-Si_3N_4, with carbon replacing the silicon in a networking of CN_4 tetrahedra linked at the corners. Its structure, illustrated in Figure 1.3, would be sp^3 hybridized at carbon and sp^2 hybridized at nitrogen

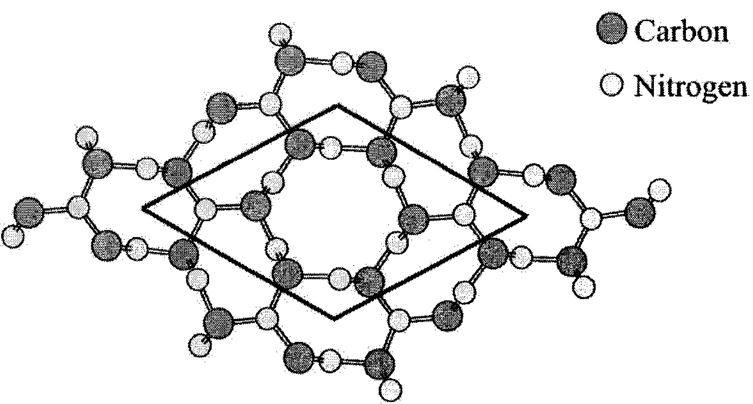

Figure 1.3 Structure of β-C_3N_4 in the x-y plane. The hexagonal unit cell is shown in the parallelogram and contains two formula units (14 atoms) with local order such that C atoms occupy slightly distorted tetrahedral sites while N atoms sit in nearly planar triply coordinated sites [7].

[7,9]. A local density approximation-based (LDA) calculation [10] for the structural and

Reproduced with permission of the copyright owner. Further reproduction prohibited without permission.

electronic properties of β-C_3N_4 indicates that the phase might be an energetically favorable in the C–N solid because the cohesive energy of β-C_3N_4 is predicted to be moderately large, 81.5 eV/unit cell.

1.3 Nucleation and Continuous Growth of Polycrystalline Covalent Materials

A large variety of deposition techniques have been employed to synthesize high quality films of crystalline covalent materials such as diamond, silicon carbide, and carbon nitride. Among film deposition techniques attempted thus far, chemical vapor deposition (CVD) shows the most promise for reproducibly attaining epitaxial film deposition required for mass production because of its precise control of gas composition and high incident surface flux of reactive gaseous species. The ability to coat a large area on a variety of substrate materials with continuous films greatly can also expand the potential application areas of covalent materials. Another highly desirable feature of CVD is that it can be carried out at lower temperatures than PVD processes for epitaxial growth, which reduces a high density of defects attributed to the difference in thermal expansions between covalent material films and substrates.

However, numerous earlier attempts to grow the covalent material films on non-covalent material substrates via CVD have yielded only polycrystalline films consisting of randomly oriented crystals and containing a varying amount of non-covalent materials and structure defects. Therefore, it has been increasingly evident that further technological development in CVD of the covalent material films, particularly in such a challenging area as the controlled growth of high quality epitaxial films, requires a more thorough understanding and control of the fundamental phenomena associated with

Reproduced with permission of the copyright owner. Further reproduction prohibited without permission.

nucleation and continuous film growth. The phenomena in CVD processes—including gas-phase and surface chemistries, heterogeneous nucleation and intermediate layer formation, and film growth with morphology evolution—critically determine film characteristics such as texture, morphology, and homogeneity. In this section, these mechanisms during nucleation and continuous film growth are briefly reviewed.

1.3.1 Gas-Phase and Surface Chemistries

The gas-phase chemistries occurring in diamond, silicon carbide, and carbon nitride growth via CVD involve reactions containing the elements C/H, C/Si/H, and C/N/H, respectively. Since the gas-phase kinetics involving these species has been the subject of decades of experimental, theoretical, and modeling research, the homogeneous kinetics is viewed well understood and documented [11-16]. In contrast, very little is known regarding the surface chemistries leading to covalent material growth. Universally accepted surface reactions mechanisms have still not yet been reported for any of the materials considered in this dissertation, and the task of uncovering these mechanisms may prove to be difficult.

However, if the goal is solely to predict the growth rate, it has been found that relatively few surface reactions—including reactions of probable gaseous growth precursors with surface reactive sites, H-atom abstraction, and surface reactive site termination—will describe the features of interest. The growth rate can be quantitatively determined once probable growth precursors are identified by examining mass fluxes of gaseous species at the deposition surface using simplified surface reaction mechanisms and comparing these to experimentally determined deposition rates.

Reproduced with permission of the copyright owner. Further reproduction prohibited without permission.

1.3.2 Heterogeneous Nucleation and Intermediate Layer Formation

The emphasis of most studies on nucleation of covalent materials has been placed on the heterogeneous formation of the nuclei on substrate surfaces. The island growth, or Volmer-Weber growth, is the mode of nucleation and growth of polycrystalline covalent materials directly on non-covalent material substrates due to a large lattice mismatch between the film and the substrate. This results in film structural defects that affect film qualities and consequently limit field applications of the materials. Among the covalent materials considered, diamond films on non-diamond substrates grown as a result of the island growth mode contain a significant degree of structural defects associated with grain boundaries and undesirable consequences of surface roughness because of the highest surface energies of diamond among any known materials in addition to the lattice mismatch. However, undesirable film morphologies might be minimized by initiating diamond deposition on non-diamond substrates with a relatively high nucleation density. A variety of substrate pretreatments in addition to the optimization of operating conditions can reduce the incubation period and enhance the nucleatation density by providing favorable chemical properties and surface conditions for diamond nucleation on substrates.

A conventional growth process in CVD of polycrystalline diamond films on non-diamond substrates generally consists of five distinguishable stages: (*i*) incubation period, (*ii*) three-dimensional heterogeneous nucleation of individual nuclei on the substrate surface, (*iii*) termination of nucleation and subsequent three-dimensional growth of diamond nuclei to individual crystallites, (*iv*) coalescence of individual crystallites and formation of continuous film, and (*v*) growth of the continuous film [17]. Before nucleation begins,

Reproduced with permission of the copyright owner. Further reproduction prohibited without permission.

the system undergoes an incubation period that may vary from seconds to minutes, depending upon specific surface pretreatment methods and operating conditions. During the incubation period prior to actual diamond nucleation, the experimental studies reveal the formation of intermediate layers on non-diamond substrate surfaces. The intermediate layer forms due to chemical reactions between adsorbed gaseous species and the substrate material. It is generally agreed that the intermediate layer formation enhances diamond nucleation densities [18-22] and thus strongly affects the morphology [18-20] and orientation [23,24] of diamond films subsequently grown on the layer. When Si is used as a substrate, diamond nucleation on Si is almost always preceded by the formation of a β-SiC intermediate layer, and nucleation occurs on the surface of the carbide.

Compared to extensive experimental investigations of intermediate layer formation during diamond CVD, fundamental scientific issues related to intermediate layer formation remain less well addressed, and further work is needed in this areas. A comprehensive theoretical model—including gas-phase and surface reactions, impingement, adsorption and desorption, surface and bulk diffusions, diamond nucleation, and β-SiC intermediate layer formation—with detailed information of adsorption energies, bulk diffusion energies, and sticking coefficients is required to achieve a thorough understanding of intermediate layer formation processes and to reveal the role of the intermediate layer in diamond nucleation. The critical features of the intermediate layer formation and the early stage of diamond nucleation are illustrated in Figure 1.4.

1.3.3 Epitaxial Growth and Morphology Evolution

When the covalent materials such as diamond and silicon carbide are grown on substrates via the island growth mode, the epitaxial growth can be described using an ev-

Reproduced with permission of the copyright owner. Further reproduction prohibited without permission.

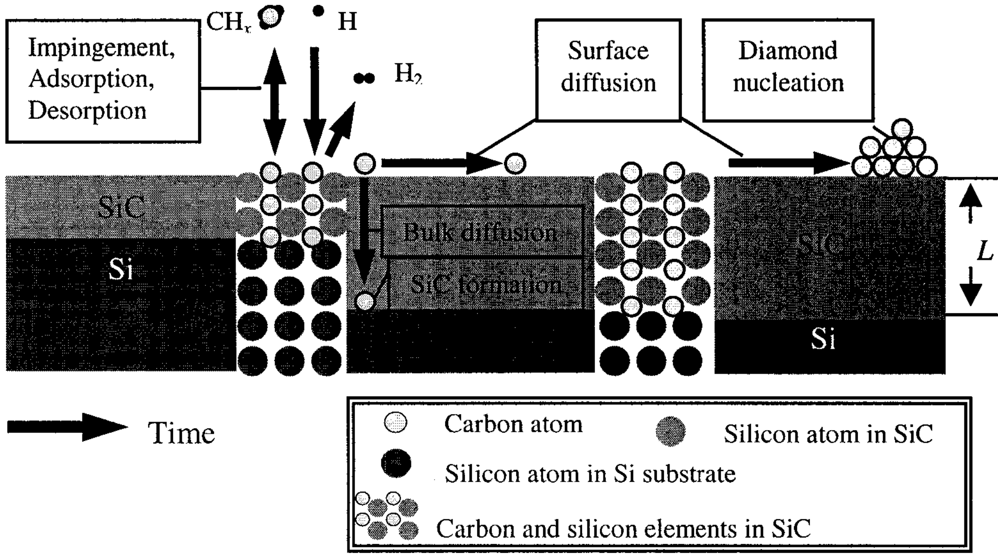

Figure 1.4 Critical features of the intermediate layer formation and the early stage of diamond nucleation.

olution mechanism, termed the van der Drift model [25,26], of orientated crystals from randomly orientated nuclei. The model is expressed by the growth-rate parameter, $\alpha_{3D} = \sqrt{3}V_{100}/V_{111}$, where V_{100} and V_{111} are the growth velocities of the {100} and {111}-facets. The α_{3D} value can be determined from the texture of a continuous polycrystalline film, assuming the absence of secondary nucleation and twinned crystals [26], and the parameter depends most strongly on substrate temperature and the near–surface gas composition. In this model, the growth competition between evolving nucleated seed crystals, correlated to this one parameter (α_{3D}), results the texture and morphology of polycrystalline films. As growth proceeds, those crystals having their fastest growth direction perpendicular to the substrate surface overgrow crystals with different orientations, and the orientation of the surviving crystals are then represented on the film surface. Thus, once a continuous film forms the overall film misorientation decreases

Reproduced with permission of the copyright owner. Further reproduction prohibited without permission.

with increasing film thickness, and the misoriented crystals are eventually buried by growing diamond films out to greater thicknesses.

As with any CVD process, the crystallographic texture and surface morphology of a continuous polycrystalline film are both strongly affected by the operating conditions and film thickness. Accordingly, the microstructural and morphological film characteristics—surface roughness, film texture and orientation, and grain size—can be optimized by applying different combinations of the deposition conditions. However, it should be noted that determination of the dependence of polycrystalline film characteristics on the deposition conditions is not yet sufficiently quantitative to the degree required for precise control of film characteristics. At the present time, covalent films synthesized by a variety of CVD processes often have randomly orientated crystals and highly disordered texture, as well as poor surface morphology.

1.4 Research Objectives

The objectives for this work are

(*i*) to simulate the chemical vapor deposition of polycrystalline carbon nitride in stagnation flow reactors. It has been predicted by Liu and Cohen [6,7] that β-C_3N_4, a polytype of crystalline carbon nitride (C–N), would have a hardness comparable to or greater than that of diamond. In the last decade there have been considerable efforts to synthesize and analyze β-C_3N_4 films. Unfortunately, adequate samples for quantitative measurements of the bulk modulus of the crystalline β-C_3N_4 have not yet been synthesized, and most investigators have observed the formation of amorphous carbon films containing varying amounts of nitrogen, generically referred to

Reproduced with permission of the copyright owner. Further reproduction prohibited without permission.

as CN_x. However, high quality crystalline β-C_3N_4 may be synthesized using thin film techniques if a more thorough understanding of carbon nitrogen deposition conditions is achieved. The purpose of this study is to explore the gas phase chemistry and its dependence on operating conditions, temperature and velocity profiles, to determine potential gaseous film growth precursors of carbon nitride film deposition occurring inside pedestal stagnation flow CVD reactors, and to evaluate the likelihood of bond rearrangement occurring in the bulk phase or on the deposition surface subsequent to the adsorption of the gaseous precursors.

(*ii*) to investigate the formation of the β-SiC intermediate layer during nucleation and the early stages of diamond deposition in CVD reactors. It appears that when a β-SiC intermediate layer develops at the interface between a diamond film and a Si substrate, it is due to the bulk diffusion of carbon atoms through the intermediate layer toward the Si substrate surface under the operating conditions conductive to diamond nucleation; however, theoretical modeling studies of intermediate layer formation are scarce, and the kinetics are not completely understood. The purpose of this study is (*a*) to predict the time evolution of a β-SiC intermediate layer under the operating conditions conductive to diamond nucleation via HFCVD; (*b*) to determine the dependence of the time evolution of the layer on operating parameters such as substrate temperature and inlet gas composition; (*c*) to compare the time scales associated with intermediate layer growth and diamond nuclei growth; (*d*) to examine discrepancies in published adsorption energies of gaseous hydrocarbon precursors on the β-SiC (100) surface and then determine the most reasonable value or range of adsorption energy consistent with published experimental data on inter-

Reproduced with permission of the copyright owner. Further reproduction prohibited without permission.

mediate layer thickness; and (*e*) to discern, quantitatively, the operating conditions that lead to intermediate layer growth followed by diamond deposition versus those that yield heteroepitaxial diamond nucleation without intermediate layer formation.

(*iii*) to gain insight into the polycrystalline growth of β-SiC films on Si (100) substrates in stagnation flow reactors. One of silicon carbide polytypes, β-SiC, is considered as an excellent candidate for use in high power electronic applications. However, the difficulty in achieving uniform texture and morphology of films via CVD has limited the possible application of β-SiC. The surface morphology of a continuous polycrystalline β-SiC film may be determined by the reactor operating conditions, including the substrate temperature and the inlet gas composition. At this time, the effects of these operating parameters on the resulting surface morphology are not fully understood. An understanding of the relationships between operating conditions and film morphology may lead to optimal yield of films that are highly <100>-textured, with {100} facets. The purpose of the present work is to predict the dependence of the surface morphology of β-SiC films grown by CVD on substrate temperature and inlet atomic ratio of Si to C, and to model the morphological evolution of the growing polycrystalline film.

(*iv*) to study the crystallographic texture and surface morphology of diamond films deposited on pretreated Si substrates, including flat and stepped β-SiC layers, via a two-stage CVD process comprised of (1) diamond nucleation and (2) continuous film growth. It is generally recognized that the texture and morphology of diamond films are strongly affected by the deposition conditions. However, quantitative understanding of the dependence of diamond film characteristics on the deposition

Reproduced with permission of the copyright owner. Further reproduction prohibited without permission.

conditions is primarily speculative and is needed to improve to the degree required for precise control of diamond film characteristics. The purpose of this theoretical study is to develop a fundamental understanding of the diamond nucleation and film growth mechanism on different pretreated Si substrates, including flat and stepped β-SiC layers, and apply this knowledge to optimize the texture and morphology of diamond films through control of the deposition conditions.

1.5 Organization of the Dissertation

A brief outline of the chapters are given below.

Chapter 2: "*Analysis of carbon nitride growth in pedestal reactors by chemical vapor deposition.*" In this chapter, a model is developed to investigate chemical vapor deposition of polycrystalline carbon nitride in stagnation flow reactors under conditions representative of those used in published experimental studies. The governing conservation equations, including gas phase and surface reactions, are solved numerically to simulate these aspects of carbon nitride film growth.

Chapter 3: "*A kinetic model of diamond nucleation and silicon carbide interlayer formation during chemical vapor deposition.*" This chapter includes a theoretical study of important aspects of the formation of the β-SiC intermediate layer between diamond films and Si substrates during nucleation and the early stages of diamond deposition. A kinetic mechanism–including gas-phase and surface reactions, impingement, adsorption and desorption, surface and bulk diffusions, diamond nucleation, and β-SiC intermediate layer formation–is built up on an existing diamond

Reproduced with permission of the copyright owner. Further reproduction prohibited without permission.

nucleation model with detailed information of adsorption energies, bulk diffusion energies, and sticking coefficients.

Chapter 4: "*A model of morphology evolution in the growth of polycrystalline β-SiC films*." A numerical model based on growth rate parameters is applied to predict the evolution of the surface morphology of continuous polycrystalline β-SiC films. The model quantifies the texture, surface roughness, and grain size of the films resulting from growth competition between nucleated seed crystals of known orientation.

Chapter 5: "*A morphological study of diamond films deposited on pretreated Si substrates*." In this chapter, a morphology evolution model is applied to calculate the texture and morphology of diamond films grown on flat and stepped β-SiC layers during diamond nucleation and continuous film growth stages. The model is also used to capture the dependence of the diamond film characteristics—mean surface roughness, average peak-to-valley height, grain size ratio <10>/<11>, and average grain size—on different pretreated substrates under operating conditions conductive to both diamond nucleation and continuous film growth.

Chapter 6: This chapter includes the overall conclusions and recommendations for future work.

Reproduced with permission of the copyright owner. Further reproduction prohibited without permission.

1.6 References

1. J.E. Field, The properties of diamond, (Academic Press, London, 1979).
2. H.O. Pierson, Handbook of carbon, graphite, diamond and fullerenes, (Noyes Pub., Park Ridge, New Jersey, 1993).
3. P.K. Bachmann and R. Messier, Emerging technology of diamond thin films, *C&EN* **67**, 24 (1989).
4. J.A. Powell and L.G. Matus, Springer Proceedings in Physics **34**, 2 (1989).
5. M. Bhatnagar and B.J. Baliga, IEEE Trans. on Electron Devices **40,** 645 (1993).
6. M.L. Cohen, Phys. Rev. B **32**, 7988 (1985).
7. A.Y. Liu and M.L. Cohen, Sci. **245**, 841 (1989).
8. J. Martin-Gil, F.J. Martin-Gil, M. Sarikaya, M.X. Qian, M. Jose-Yacaman, and A. Rubio, J. Appl. Phys. **81**, 2555 (1997).
9. C. Niu, Y.Z. Lu, and C.M. Liber, Sci. **261**, 334 (1993).
10. A.Y. Liu and M.L. Cohen, Phys. Rev. B **41**, 10727 (1994).
11. M.E. Coltrin and D.S. Dandy, J. Appl. Phys. **74**, 5803 (1993).
12. M. D. Allendorf and R. J. Kee, J. Electrochem. Soc. **138**, 841 (1991).
13. J.A. Miller and C.F. Melius, Combust. Flame **91**, 21 (1992).
14. P.Glarborg, K.Dam-Johansen, and J.A.Miller, Int. J. Chem. Kinet. **27**, 1207 (1995).
15. L.Prada and J.A.Miller, Combust. Sci. and Tech. **132**, 225 (1998).
16. P.Glarborg, M.U. Alzueta, K.Dam-Johansen, and J.A. Miller, Combust. Flame **115**, 1 (1998).

Reproduced with permission of the copyright owner. Further reproduction prohibited without permission.

17. M. Yoshikawa, Diamond Films and Technol. **1**, 1 (1991).

18. K.V. Ravi and C.A. Koch, Appl. Phys. Lett. **57**, 348 (1990).

19. K.V. Ravi, J. Mater. Res. **7**, 384 (1992).

20. K.V. Ravi, C.A. Koch, H.S. Hu, and A. Joshi, J. Mater. Res. **5**, 2356 (1990).

21. D. Michau, B. Tanguy, G. Demazeau, M. Couzi, and R. Cavagnat, Diamond Relat. Mater. **2**, 19 (1993).

22. Z. Li, L. Wang, T. Suzuki, A. Argoitia, P. Pirouz, and J. Angus, J. Appl. Phys. **73**, 711 (1993).

23. B.R. Stoner, S.R. Sahaida, J.P. Bade, P. Southworth, and P.J. Ellis, J. Mater. Res. **8**, 1334 (1993).

24. S.D. Wolter, B.R. Stoner, J.T. Glass, P.J. Ellis, D.S. Buhaenko, C.E. Jenkins, and P. Southworth, Appl. Phys. Lett. **62**, 1215 (1993).

25. C. Wild, N. Herres, and P. Koidl, J. Appl. Phys. **68**, 973 (1990).

26. C. Wild, P. Koidl, W. Müller-Sebert, H. Walcher, R. Kohl, N. Herres, R. Locher, R. Samlenski, and R. Brenn, Diamond Relat. Mater. **2**, 158 (1993).

Reproduced with permission of the copyright owner. Further reproduction prohibited without permission.

Chapter 2

ANALYSIS OF CARBON NITRIDE GROWTH IN PEDESTAL REACTORS BY CHEMICAL VAPOR DEPOSITION

2.1 Introduction

Liu and Cohen [1,2] have predicted that β-C_3N_4, a polytype of crystalline carbon nitride (C–N), would have a hardness comparable to or greater than that of diamond. The postulation was based on a combination of an empirical model [1] and an *ab initio* calculation [2], indicating that a large bulk modulus could be achieved for a covalent solid formed between carbon and nitride with short covalent bond lengths and low ionicity. The material is expected to have a structure similar to that of β–Si_3N_4, with carbon replacing the silicon in a network of CN_4 tetrahedra linked at the corners. Its structure would be sp^3 hybridized at carbon and sp^2 hybridized at nitrogen [2].

The theoretical prediction of Liu and Cohen was supported by a local density approximation-based (LDA) calculation for the structural and electronic properties of β-C_3N_4 [3]. The LDA calculation indicated that β-C_3N_4 might be an energetically favorable phase in the C–N solid because the cohesive energy of β-C_3N_4 was predicted to be moderately large, 81.5 eV/unit cell. It was also predicted that two metastable structures, one resembling a zinc-blende CN vacancy per cubic cell and the other resembling graphitic CN with one C vacancy per four N sites, could be synthesized in addition to the

The text of Chapter 2 consists of manuscript which has been submitted for publication in Diamond and Related Materials.

Reproduced with permission of the copyright owner. Further reproduction prohibited without permission.

hexagonal β-C_3N_4 structure [3,4]. According to that study, both the refined β-phase and the cubic phase would also have compressibilities comparable to that of diamond (1.7×10^{-7} cm^2/kg), where the compressibility of diamond is lower than any known material.

However, Guo and Goddard [5] produced a theoretical result contradicting the hypothesis of Liu and Cohen [1-4]. Guo and Goddard's prediction of the crystalline properties of C_3N_4 was based on the method of molecular simulation force field (MSFF). They pointed out the restrictions of the calculation carried out by Liu and Cohen [2,3] that led to different quantitative results. It was concluded by Guo and Goddard that, in the earlier calculations, the bulk modulus of C_3N_4 was over-predicted because the possibility of nonplanar nitrogen in the C_3N_4 structure was not considered and a uniform scale in the coordinate system was assumed. The results of Guo and Goddard indicated that α-C_3N_4 would be more stable than β-C_3N_4 due to the large energy difference between these phases. Thus, according to Guo and Goddard, a carbon nitride film formed with thin film deposition techniques would be α-C_3N_4. In addition, they predicted that the bulk modulus of α- and β-C_3N_4 would be about half the value for diamond and, incredibly, that the Poisson ratio of α-C_3N_4 would be negative.

Despite the predictions of Guo and Goddard [5] to the contrary, in the last several years there have been considerable efforts to synthesize and analyze carbon nitride films [6-46]. Most investigators have observed the formation of amorphous carbon films containing varying amounts of nitrogen, generically referred to as CN_x. The synthesis of crystalline β-C_3N_4 in amorphous C–N films has been reported in only several cases [38-46]. Film deposition techniques in these investigations have included pulsed laser

Reproduced with permission of the copyright owner. Further reproduction prohibited without permission.

ablation [38], radio frequency (rf) [39,44] and plasma arc sputtering [40], chemical vapor deposition (CVD) [41,42,46], shock wave compression [43], and ion-assisted deposition [45].

Niu et al. [38] reported the synthesis of microcrystalline β-C_3N_4 using pulsed laser ablation of graphite targets combined with an intense atomic nitrogen source. It was observed that controlling the atomic nitrogen flux varied the average nitrogen content in the films. Yu et al. [39] detected growing crystalline β-C_3N_4 grains on Si (100) wafers using rf diode sputtering of a pure graphite target together with pure N_2. These grains had typical dimensions of 0.5 to 1 μm and occupied less than 5% of the volume of the 1 μm-thick layer of amorphous C–N film in which they were embedded. In that study, it was found that the crystalline particles were difficult to locate in the amorphous graphitic phase. The particles were more frequently found in regions where the overlayer C–N film peeled off, because the particles were preferentially crystallized on the Si (100) surface and were buried by an amorphous C–N film for which the N/C ratio was lower than that in the particles. Matsumoto et al. [40] grew crystalline β-C_3N_4 from CN radicals prepared by the reaction of gaseous N atoms with C atoms sputtered from a graphite rod anode in an argon-nitrogen plasma arc at atmospheric pressure. They concluded that crystalline carbon nitride would be deposited from CN or C_2N_2 radicals created in the nitrogen plasma arc irradiating the carbon anode. Yen and Chou [41,42] observed the formation of nanocrystalline β-C_3N_4 (~0.1 μm crystals) in carbon nitride films with an overall N/C ratio of approximately 0.75. These films were deposited using rotating arc-plasma jet chemical vapor deposition on nickel substrates. Bursill et al. [43] grew carbon nitride films containing both crystalline and amorphous components using a high-energy shock

Reproduced with permission of the copyright owner. Further reproduction prohibited without permission.

plasma deposition technique. Zhang et al. [44] reported the growth of polycrystalline β-C_3N_4 films on single-crystal KBr wafers using rf diode sputtering. In that study, the substrate temperature was held below 373 K to reduce the loss of nitrogen species from the growth surface through thermal desorption.

Wu et al. [45] prepared films of various carbon phases containing tetrahedrally bonded carbon nitrides, β-C_3N_4, and other carbon nitrides (the N:C ratio varied from 0.5 to 1.1 in the films) grown using an ion beam enhanced deposition technology. They found that the concentration of the β-C_3N_4 phase in the deposited films increased with a simultaneous increase of total nitrogen concentration in the films. Zhang et al. [46] reported that crystalline carbon nitride films with large crystalline grains, up to ~10 μm in size, and film-like regions of the crystalline phase were grown on polycrystalline Ni substrates using a plasma-assisted hot filament chemical vapor deposition technique. They observed the crystallographic structure associated with β-C_3N_4 in the deposited films using the X-ray diffraction (XRD) spectrum.

Most experimental investigations into the growth of β-C_3N_4, which have used a mixture of CH_4 and N_2 as the feed, indicate that the CN films have much lower nitrogen concentration than the 57% required for stoichiometric β-C_3N_4. This result suggests that very high concentrations of reactive nitrogen bearing gaseous species, including atomic nitrogen, are necessary for the growth of β-C_3N_4 [41]. Among the various low pressure film deposition techniques attempted thus far, CVD is an attractive method for the β-C_3N_4 synthesis because of its precise control of gas composition and high incident surface flux of reactive gaseous species. Studies on the synthesis of β-C_3N_4 have been conducted using techniques similar to those used in diamond CVD, with the addition of a

Reproduced with permission of the copyright owner. Further reproduction prohibited without permission.

nitrogen component [46]. Unfortunately, adequate samples for quantitative measurements of the bulk modulus of the crystalline carbon nitride have not yet been synthesized. However, it may be possible to determine the crystal structure, stability of β-C_3N_4, and other metastable carbon nitride phases if thicker, higher quality films of crystalline carbon nitride can be deposited on substrates. High quality crystalline carbon nitride may be synthesized using thin film techniques if a more thorough understanding of carbon nitride deposition conditions is achieved.

A detailed theoretical analysis of the elementary surface reactions leading to carbon nitride growth has not yet been reported, and the task of uncovering these mechanisms may prove to be difficult. However, if the goal is limited to predicting the growth rate of the carbon nitride film, relatively few surface reactions—including reactions of probable gaseous film growth precursors with surface reactive sites, H-atom abstraction, and surface reactive site termination—will describe the features of interest. Further, the growth rate can be maximized if the near-surface concentrations of the most probable gaseous film growth precursors are maximized. This can only be achieved by identifying probable growth precursors. Probable growth precursors of carbon nitride may be identified by examining mass fluxes of gaseous species at the deposition surface using simplified growth mechanisms and comparing these to experimentally determined deposition rates. In addition, the availability of data describing the relative concentrations of different bond types (C–N, C=N, C≡N, C=C, etc.) in solid CN_x films [14] provides the opportunity to explore the extent to which bond rearrangement occurs on the deposition surface or in the bulk phase once reactive species are adsorbed. Put another way, since CN_x films grown to date do not exhibit exclusive sp^2 hybridization for nitrogen and sp^3

Reproduced with permission of the copyright owner. Further reproduction prohibited without permission.

hybridization for carbon, it's useful to ask whether these films inherit their spectrum of bond types directly from the species adsorbing from the gas phase, or by subsequent chemical rearrangement of the bonds after the molecules have been adsorbed. This issue can be investigated by examining whether the predicted fluxes of gaseous species at the surface correlate with the relative concentrations of bond types in the films.

The results of two experimental studies by Ricci et al. [14] and Zhang et al. [46] are compared to the predictions in this study. Although there have been a number of attempts to synthesize β-C_3N_4 via CVD, detailed data on the deposition rate of the β-C_3N_4 film and the relative concentrations of different bond types in carbon nitride films are not readily available in the literature. Zhang et al. [46] synthesized crystalline β-C_3N_4 at a relatively high film growth rate, 1.2 μm/h, using a hot filament CVD reactor, while Ricci et al. [14] determined the different bond types in the carbon nitride films by using infrared (IR) absorption.

The primary purposes of this study are to explore the gas phase chemistry and its dependence on operating conditions, temperature and velocity profiles, and to determine potential gaseous film growth precursors of carbon nitride film deposition occurring inside pedestal stagnation flow CVD reactors. In addition, it is worthwhile exploring whether significant bond rearrangement occurs on the deposition surface or in the bulk phase once the gaseous precursors are adsorbed because this may give some indication of the possible complexity of quantitative deposition models. The governing conservation equations, including gas phase and surface reactions, are solved numerically to simulate these aspects of carbon nitride film growth.

Reproduced with permission of the copyright owner. Further reproduction prohibited without permission.

In the examination of both probable growth precursors and bond type correlation, a simplified set of surface reactions is applied to obtain mass fluxes of gaseous species at the deposition surface. The collision and subsequent surface reaction of a gaseous species with the deposition surface results in the formation of a surface species; bulk species are then formed when all reactive bonds of a surface species are to other surface species or bulk species through surface reactions. The surface reactions are considered as ireversible, and the rate constants are represented by sticking probabilities.

First, the CVD system under study is described, and the corresponding governing equations and boundary conditions are discussed. The experimental data of Ricci et al. [14] is used to see whether a correlation exists between bond types of adsorbing species and bond types in the carbon nitride films. The film growth rate is calculated for each presumed growth precursor using the experimental operating conditions of Zhang et al. [46]. Then, comparisons between the computational results and experimental data are used to predict the possible gaseous species contributing to the growth of carbon nitride. Finally, the numerical model is applied to investigate the effects of various operating parameters—the inlet and substrate temperatures, reactor pressure, and inlet gas composition—on the concentrations of probable growth precursors at the deposition surface. The operating conditions to be used are selected from existing experimental data on carbon nitride growth via CVD.

2.2 Model Description

Consider a system configured with the inlet axis orthogonal to the substrate such that a forced flow of reactant gases impinges upon an isothermal substrate, as illustrated

Reproduced with permission of the copyright owner. Further reproduction prohibited without permission.

in Figure 2.1. The geometry of the system is described in terms of cylindrical coordinate

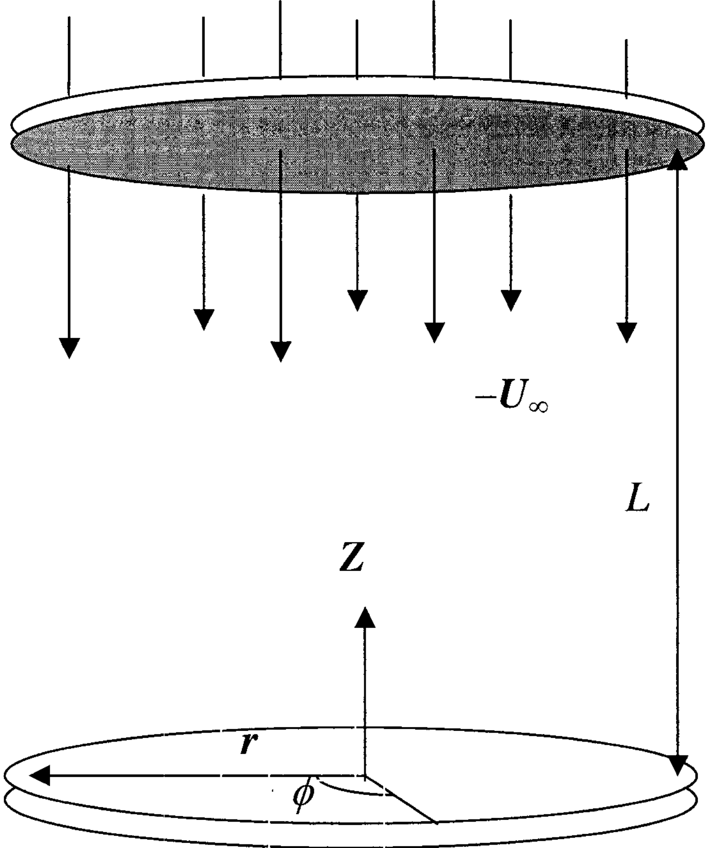

Figure 2.1 Schematic diagram of the CVD geometry considered. The geometry of the system is represented in terms of the cylindrical coordinates (r, ϕ, z).

(r, ϕ, z), with the origin of the coordinate system located at the center on the substrate surface. An idealized stagnation flow geometry is assumed to exist in the region between the inlet and the substrate. The gas flows uniformly downward from the inlet towards the substrate surface with known temperature, velocity, and composition at the inlet. The uniform axial down flow at inlet, located at the position $z = L$, is given by $-U_\infty$, and the temperature and mole fractions at this location are denoted by T_∞ and $X_{k\infty}$. The axial velocity component does not vanish at the substrate surface due to the net deposition of

Reproduced with permission of the copyright owner. Further reproduction prohibited without permission.

mass onto that surface. The radial velocity component at the surface vanishes due to the no-slip condition. At the deposition surface the gas temperature matches that of the substrate, T_s. At steady state the net production rate of a gaseous species at the substrate surface is equal to its mass flux at the substrate surface, and the net production rate of any surface species on the substrate surface is zero.

The steady-state conservation equations describe the momentum and energy transport, convective and diffusive transport of the species, the chemical composition of the gas phase, and the surface concentrations of the adsorbed species [47,48]. The conservation equations consist of radial, axial, and circumferential momentum equations, gaseous species continuity equations, a mixture continuity equation, thermal energy equation, and surface species conservation equations. The conservation equations yield an axisymmetric similarity solution for the geometry shown in Figure 2.1 because all dependent variables in the equations may be considered to be functions only of axial coordinate, z, with radial and angular velocities rescaled by the radial coordinate, r [49]. The conservation equations are comprised of K_g+K_s+4 coupled ordinary differential equations, together with the necessary constitutive equations and boundary conditions, where K_g and K_s are the numbers of gaseous species and surface species in the model, respectively.

Numerical solutions for the governing equations and the appropriate boundary conditions are found for the gas composition, temperature and velocity profiles, and deposition rates [47]. Chemkin-III, a Fortran chemical kinetics package, is used for the analysis of gas phase chemical kinetics [50]. The gas phase reaction mechanism used in this study is listed in Table 2.1 [51]. The reaction mechanism for C/N/H gas mixtures has

Reproduced with permission of the copyright owner. Further reproduction prohibited without permission.

Table 2.1 Gas-phase reaction mechanisms for C/N/H gas mixtures.

Reaction		A_i^a	b_i^a	E_i^a
G1	$H + H + M \leftrightarrow H_2 + M$	0.100×10^{19}	−1.0	0.0
G2	$H + H + H_2 \leftrightarrow H_2 + H_2$	0.920×10^{17}	−0.6	0.0
G3	$CH_3 + CH_3 (+M) \leftrightarrow C_2H_6 (+M)$	9.220×10^{16}	−1.174	635.8
G4	$CH_3 + H (+M) \leftrightarrow CH_4 (+M)$	6.000×10^{16}	−1.0	0.0
G5	$CH_4 + H \leftrightarrow CH_3 + H_2$	0.220×10^{5}	3.0	8750.0
G6	$CH_3 + H \leftrightarrow CH_2 + H_2$	0.900×10^{14}	0.0	15100.0
G7	$CH_2 + H \leftrightarrow CH + H_2$	0.100×10^{19}	−1.56	0.0
G8	$CH + H \leftrightarrow C + H_2$	0.150×10^{15}	0.0	0.0
G9	$CH + CH_2 \leftrightarrow C_2H_2 + H$	0.400×10^{14}	0.0	0.0
G10	$CH + CH_3 \leftrightarrow C_2H_3 + H$	0.300×10^{14}	0.0	0.0
G11	$CH + CH_4 \leftrightarrow C_2H_4 + H$	0.600×10^{14}	0.0	0.0
G12	$C + CH_3 \leftrightarrow C_2H_2 + H$	0.500×10^{15}	0.0	0.0
G13	$C + CH_2 \leftrightarrow C_2H + H$	0.500×10^{14}	0.0	0.0
G14	$C_2H_6 + CH_3 \leftrightarrow C_2H_5 + CH_4$	0.550×10^{0}	4.0	8300.0
G15	$C_2H_6 + H \leftrightarrow C_2H_5 + H_2$	0.540×10^{3}	3.5	5210.0
G16	$C_2H_4 + H \leftrightarrow C_2H_3 + H_2$	5.420×10^{14}	0.0	14902.0
G17	$CH_2 + CH_3 \leftrightarrow C_2H_4 + H$	0.400×10^{14}	0.0	0.0
G18	$H + C_2H_4 (+M) \leftrightarrow C_2H_5 (+M)$	0.221×10^{14}	0.0	2066.0
G19	$C_2H_5 + H \leftrightarrow CH_3 + CH_3$	1.000×10^{14}	0.0	0.0
G20	$H_2 + C_2H \leftrightarrow C_2H_2 + H$	0.409×10^{6}	2.39	864.3
G21	$H + C_2H_2 (+M) \leftrightarrow C_2H_3 (+M)$	0.554×10^{13}	0.0	2410.0
G22	$C_2H_3 + H \leftrightarrow C_2H_2 + H_2$	0.400×10^{14}	0.0	0.0
G23	$C_2H_3 + C_2H \leftrightarrow C_2H_2 + C_2H_2$	0.300×10^{14}	0.0	0.0
G24	$C_2H_3 + CH \leftrightarrow CH_2 + C_2H_2$	0.500×10^{14}	0.0	0.0
G25	$CH_2(S) + M \leftrightarrow CH_2 + M$	0.100×10^{14}	0.0	0.0
G26	$CH_2(S) + CH_4 \leftrightarrow CH_3 + CH_3$	0.400×10^{14}	0.0	0.0
G27	$CH_2(S) + C_2H_6 \leftrightarrow CH_3 + C_2H_5$	0.120×10^{15}	0.0	0.0
G28	$CH_2(S) + H_2 \leftrightarrow CH_3 + H$	0.700×10^{14}	0.0	0.0
G29	$CH_2(S) + C_2H_2 \leftrightarrow CH_2 + C_2H_2$	4.0×10^{13}	0.0	0.0
G30	$CH_2(S) + H \leftrightarrow CH_2 + H$	0.200×10^{15}	0.0	0.0
G31	$CH_2(S) + H \leftrightarrow CH + H_2$	3.000×10^{13}	0.0	0.0
G32	$CH_2(S) + CH_3 \leftrightarrow C_2H_4 + H$	2.000×10^{13}	0.0	0.0
G33	$C_2 + H_2 \leftrightarrow C_2H + H$	4.0×10^{5}	2.4	1000.0
G34	$CH_2 + CH_2 \leftrightarrow C_2H_2 + H + H$	0.400×10^{14}	0.0	0.0
G35	$C_2H_2 + M \leftrightarrow C_2H + H + M$	0.420×10^{17}	0.0	10700.0
G36	$C_2H_4 + M \leftrightarrow C_2H_2 + H_2 + M$	0.150×10^{16}	0.0	55800.0
G37	$C_2H_4 + M \leftrightarrow C_2H_3 + H + M$	0.140×10^{17}	0.0	82360.0
G38	$CH + N_2 \leftrightarrow HCN + N$	5.400×10^{12}	0.0	25000.0
G39	$C + N_2 \leftrightarrow CN + N$	6.300×10^{13}	0.0	46019.0
G40	$CH_2 + N_2 \leftrightarrow HCN + NH$	0.100×10^{14}	0.0	74000.0

Reproduced with permission of the copyright owner. Further reproduction prohibited without permission.

Table 2.1 (Continued)

G41	$H_2CN + N \leftrightarrow N_2 + CH_2$	0.200×10^{14}	0.0	0.0
G42	$H_2CN + M \leftrightarrow HCN + H + M$	0.300×10^{15}	0.0	22000.0
G43	$CH_2 + N \leftrightarrow HCN + H$	0.500×10^{14}	0.0	0.0
G44	$CH + N \leftrightarrow CN + H$	0.130×10^{14}	0.0	0.0
G45	$CH_3 + N \leftrightarrow H_2CN + H$	7.100×10^{13}	0.0	0.0
G46	$C_2H_3 + N \leftrightarrow HCN + CH_2$	0.200×10^{14}	0.0	0.0
G47	$CN + H_2 \leftrightarrow HCN + H$	0.295×10^{6}	2.45	2237.0
G48	$CH + HCN \leftrightarrow CH_2 + CN$	3.010×10^{13}	0.0	−993.5
G49	$CN + HCN \leftrightarrow C_2N_2 + H$	1.320×10^{3}	2.7	646.0
G50	$CN + CH_4 \leftrightarrow CH_3 + HCN$	6.020×10^{4}	2.64	−437.0
G51	$CN + C_2H_6 \leftrightarrow C_2H_5 + HCN$	1.200×10^{5}	2.77	−1788.0
G52	$NCN + H \leftrightarrow HCN + N$	1.000×10^{14}	0.0	0.0
G53	$NH + N \leftrightarrow N_2 + H$	0.300×10^{14}	0.0	0.0
G54	$NH + H \leftrightarrow N + H_2$	3.000×10^{13}	0.0	0.0
G55	$NH_2 + H \leftrightarrow NH + H_2$	0.692×10^{14}	0.0	3650.0
G56	$NH_3 + H \leftrightarrow NH_2 + H_2$	0.636×10^{6}	2.39	10171.0
G57	$NNH \leftrightarrow N_2 + H$	1.000×10^{6}	0.0	0.0
G58	$NNH + H \leftrightarrow N_2 + H_2$	0.100×10^{15}	0.0	0.0
G59	$NNH + NH_2 \leftrightarrow N_2 + NH_3$	0.500×10^{14}	0.0	0.0
G60	$NNH + NH \leftrightarrow N_2 + NH_2$	0.500×10^{14}	0.0	0.0
G61	$NH_2 + NH \leftrightarrow N_2H_2 + H$	0.500×10^{14}	0.0	0.0
G62	$NH + NH \leftrightarrow N_2 + H + H$	0.254×10^{14}	0.0	0.0
G63	$NH_2 + N \leftrightarrow N_2 + H + H$	0.720×10^{14}	0.0	0.0
G64	$N_2H_2 + M \leftrightarrow NNH + H + M$	0.500×10^{17}	0.0	50000.0
G65	$N_2H_2 + H \leftrightarrow NNH + H_2$	0.500×10^{14}	0.0	1000.0
G66	$N_2H_2 + NH \leftrightarrow NNH + NH_2$	0.100×10^{14}	0.0	1000.0
G67	$N_2H_2 + NH_2 \leftrightarrow NH_3 + NNH$	0.100×10^{14}	0.0	1000.0
G68	$NH_2 + NH_2 \leftrightarrow N_2H_2 + H_2$	0.500×10^{12}	0.0	0.0

[a]Arrhenius parameters for the forward reaction rate constants shown in the form $k_{fi} = A_i T^{b_i} e^{-E_i/RT}$ (A_i in moles, cubic centimeters, and seconds; E_i in cal/mole). Each of the gas-phase reactions is reversible, and the reverse rate is obtained from the reaction equilibrium constants. All reaction rates, equilibrium constants, and thermodynamic properties for gas-phase species are evaluated by using Chemkin-III [50].

been also reported in other kinetic studies [52-54], but the predicted gas phase chemistry from the mechanism used in this study [51] is in a reasonable agreement with those from other mechanisms. The gas-phase multicomponent transport properties are evaluated using a computer package [55]. Surface Chemkin is used for the treatment of the hetero-

Reproduced with permission of the copyright owner. Further reproduction prohibited without permission.

geneous reactions occurring at the deposition surface and these are listed in Table 2.2 [56].

Table 2.2 Surface reaction mechanisms for presumed β-C_3N_4 film growth precursors.

Growth species		Reaction
CH_x	S1	$NH(S) + H \rightarrow N*(S) + H_2$
	S2	$N*(S) + H \rightarrow NH(S)$
$(x \neq 0)$	S3	$N*(S) + CH_x \rightarrow B + CH(S) + H_{x-1}$
or $(x = 0)$	S3	$N*(S) + C \rightarrow B + C*(S)$
C_2H_x	S4	$NH(S) + H \rightarrow N*(S) + H_2$
	S5	$N*(S) + H \rightarrow NH(S)$
	S6	$N*(S) + C_2H_x \rightarrow B + C_2H(S) + H_{x-1}$
NH_x	S7	$CH(S) + H \rightarrow C*(S) + H_2$
	S8	$C*(S) + H \rightarrow CH(S)$
$(x \neq 0)$	S9	$C*(S) + NH_x \rightarrow B + NH(S) + H_{x-1}$
or $(x = 0)$	S9	$C*(S) + N \rightarrow B + N*(S)$
H_xCN	S10	$NH(S) + H \rightarrow N*(S) + H_2$
	S11	$N*(S) + H \rightarrow NH(S)$
	S12	$N*(S) + H_xCN \rightarrow B + HCN(S) + H_{x-1}$
or	S13	$CH(S) + H \rightarrow C*(S) + H_2$
	S14	$C*(S) + H \rightarrow CH(S)$
	S15	$C*(S) + H_xCN \rightarrow B + HCN(S) + H_{x-1}$

The surface sites and bulk species are represented by S and B. Each of the surface reactions is irreversible, and the sticking coefficients γ_i are used to convert surface reaction rate constants. The sticking coefficient's form for reaction i is taken to be $\gamma_i = a_i T^{B_i} e^{-c_i/RT}$ where a_i and B_i are unitless and c_i has units compatible with the gas constant R. Because γ_i is defined as a probability, it must lie between 0 and 1. Equilibrium constants and thermodynamic properties for surface reactions are evaluated by using Surface Chemkin [56].

2.3 Results and Discussion

Calculations are carried out to determine the gaseous species most likely to lead to the growth of carbon nitride, and to investigate whether significant bond rearrangement

Reproduced with permission of the copyright owner. Further reproduction prohibited without permission.

occurs once the gaseous precursors are adsorbed. Operating conditions are chosen to facilitate comparison with two existing experiments [14,46]. Probable gaseous film growth precursors are determined by examining which calculated mass fluxes due to presumed growth precursors could account for the observed growth rate. The extent of bond rearrangement is investigated by inspecting whether the calculated mass fluxes at the deposition surface correlate with the experimentally measured reactive concentrations of bond types in the solid films. Further, once the probable growth precursors are determined, the effects of operating parameters—the inlet and substrate temperatures, reactor pressure, and inlet gas composition—on the concentrations of probable growth precursors at the deposition surface are investigated.

2.3.1 Correlation between Gas and Solid Bond Types

Ricci et al. [14] used IR absorption to measure several different chemical bond types, including C=N, C=C, C–N, N–H, and C≡N, in CN_x films grown using a rf plasma assisted CVD reactor. In the present calculations, the relative concentrations of the bond types in the films are determined from the absorbance measurements of Ricci et al. using Beer's law, which describes the direct proportionality between the absorbance and concentration, and these are found to be (C=N:C=C:C–N:N–H:C–H:C≡N) = (9:9:7.5:-6.5:6.5:6.3-6.4). The existence of the C≡N bond in carbon nitride films was reported by Ogata et al. [16] and Krishna et al. [24]. Diani et al. [17] detected large numbers of C–N and C=N bonds in synthesized carbon nitride films. Bousetta et al. [19] observed the existence of NH_2, C–N, CH, C≡N, and CH_2 bonds in their carbon nitride films. Thus, it appears that C≡N, C=N, and C–N bonds are common in CN_x films grown to date.

When the experimental conditions of Ricci et al. are used in the model, summarized

Reproduced with permission of the copyright owner. Further reproduction prohibited without permission.

in Table 2.3, the mole fractions of gaseous species are calculated to determine the predominant precursors at the deposition surface, and these are shown in Table 2.4. The mole

Table 2.3 Experimental conditions of Ricci et al. used in the model.

Reactor pressure P (Torr)	0.75
Inlet gas temperature T_∞ (K)	300
Substrate temperature T_s (K)	300
rf excitation power (W)	100[a]
Inlet mole fractions	
CH_4 $X_{CH_4\infty}$	0.195
N_2 $X_{N_2\infty}$	0.8
H $X_{H\infty}$	0.005[b]
Inlet axial gas velocity U (cm/s)	97[c]
Total volume flow rate Q_t (sccm)	83.3
Reactor diameter (cm)	4.5

Table 2.4 Mole fractions and mass fluxes of presumed film growth precursors at the deposition surface.

Species		Mole fraction	Mass flux (g/cm^2·s)
CH_x	CH_3	1.99×10^{-3}	1.71×10^{-7}
C_2H_x	C_2H_2	1.26×10^{-1}	1.14×10^{-6}
	C_2H_4	2.55×10^{-3}	3.15×10^{-8}
	C_2H_6	2.98×10^{-3}	3.79×10^{-8}
NH_x	N	9.27×10^{-7}	4.28×10^{-10}
	NH	1.91×10^{-6}	1.64×10^{-10}
	NH_2	2.23×10^{-6}	1.77×10^{-10}
H_xCN	HCN	1.24×10^{-3}	1.32×10^{-8}
	H_2CN	1.07×10^{-5}	1.37×10^{-10}

fractions of CH_3 and C_2H_x (x = 2,4,6) species are sufficiently high to consider those species as potential growth precursors. However, the calculated mole fractions for nitrogen bearing precursors, primarily NH_x (x = 0-2), HCN, and H_2CN, are always several

Reproduced with permission of the copyright owner. Further reproduction prohibited without permission.

orders of magnitude smaller than those of CH_3 and C_2H_x (x = 2,4,6) species due to the stability of the N_2 bond.

Although a deposition mechanism for carbon nitride deposition has not yet been postulated, the global mechanism can be described by a simple set of surface reactions if goal is solely to determine the mass flux, and therefore, the growth rate. To investigate the surface chemistry associated with the films deposited by Ricci et al., simplified sets of surface reaction mechanisms are used in the calculations of the mass fluxes for each assumed film growth species, and these are listed in Table 2.2. The simplified surface reaction mechanisms are listed for the gaseous species that have relatively high mole fractions at the deposition surface: CH_3, C_2H_x (x = 2,4,6), NH_x (x = 0-2), HCN, and H_2CN. It is assumed in the analysis that the hydrocarbon species in the gas phase, such as CH_x and C_2H_x, will bond to open surface nitrogen atom sites, the NH_x species will bond to surface carbon sites, and the H_xCN species can bond to either carbon or nitrogen atom surface sites. The simplified set of surface species considered here are CH(S) or NH(S), a surface carbon or nitrogen capped by an atomic hydrogen, and C*(S) or N*(S), a surface carbon or nitrogen radical site activated by atomic hydrogen abstraction of desorption. Each calculation is carried out for one potential gaseous film growth precursor at a time by assuming that the surface radical site bonds to that precursor with a reasonable sticking probability for that species and zero for all other gas species. Repeating sequences of the surface reactions leads to continuous epitaxial growth of carbon nitride layers.

Considering the uncertainty in the sticking probabilities for presumed growth precursors reacting with the surface reactive sites of β-C_3N_4, the sticking probabilities

Reproduced with permission of the copyright owner. Further reproduction prohibited without permission.

obtained on other surfaces such as silicon and carbon surfaces are assumed to be applicable to the β-C_3N_4 surface. Since the relatively unstable species considered as presumed growth precursors are highly reactive with surface reactive sites, the sticking probabilities for assumed growth precursors should be essentially unaffected by the different surfaces. The sticking probabilities for CH_3 and C_2H_2 used in the calculations are 0.2 and 0.02. The probability for CH_3 is derived from CH_3 adsorption on carbon surface sites [57], and the probability for C_2H_2 is that of the C_2H_2 gas species reacting with silicon surface sites [58]. The sticking probabilities of CH_x (x = 1,2) and NH_x (x = 1,2) species are assumed to be equivalent to CH_3. Although data for the sticking probabilities of these species is not available in the literature, it is not unreasonable to assume that those radicals associated with C–H or N–H bond have a comparable probability to CH_3 due to similarities in bond energies and molecule sizes. Further, the sticking probabilities of C_2H_x (x = 4,6) and H_xCN (x = 1,2) species are assumed to be the same as that of C_2H_2. Again, there are no existing experimental or theoretical results that report the sticking probabilities of C_2H_x and H_xCN. However, C_2H_x and H_xCN species having multiple bonds between C–C atoms and/or C–N atoms may have significantly lower probabilities of sticking to the surface than CH_x and NH_x. In addition, similar probabilities for C_2H_x and H_xCN species due to comparable bond energies and molecular energies are expected. Therefore, the sticking probabilities of C_2H_x and H_xCN species are assumed to be an order of magnitude lower than the probabilities of CH_x and NH_x in the calculations. Atomic carbon and nitrogen are assumed to stick with unity efficiencies by considering the high reactivity of these atoms with surface reactive sites.

Reproduced with permission of the copyright owner. Further reproduction prohibited without permission.

The predicted mass fluxes of the gas species listed in Table 2.4 indicate that stoichiometric carbon nitride is difficult to synthesize due to the significantly lower mass fluxes of NH_x (x = 0-2) and H_xCN (x = 1,2) species than those of CH_3 and C_2H_x (x = 2,4,6) species when N_2 is introduced as the inlet nitrogen source. This result is consistent with the observations that these films are always deficient in nitrogen with introducing N_2 at the inlet. The low mass fluxes of NH_x and H_xCN species are explained by the negligible decomposition of N_2 for the operating conditions used in the calculations. For example, when the experimental conditions of Ricci et al. are used, the calculations predict that less than 0.1% of the N_2 undergoes dissociation, and therefore the near-surface N_2 concentration is always several orders of magnitude higher than those of any NH_x and H_xCN species.

The adsorption of gaseous precursors often leads to the bonding structure transformation of these adsorbing species on the surface due to reactions between these species and surface atoms. The HCN adsorption studies indicate that the adsorption of HCN produces C≡N bond as well as C=N bond at the surface [59-61]. Once HCN is adsorbed, the C≡N bond can be readily formed due to either H-transfer interactions between neighboring molecules or HCN molecule dissociation. The C≡C bond in gaseous C_2H_2 becomes a C=C bond when adsorbed on the surface, while the adsorption of C_2H_4 leads to the transformation of the C=C bond into the C–C bond [62]. However, the C=N bond in gaseous H_2CN doesn't transform during H_2CN adsorption, and the main bond believed to be present on the surface is C=N bond. Whenever gaseous precursors are adsorbed on the surface, the C–N bond can be formed by reactions between adsorbing precursors and surface carbon or nitrogen atoms.

Reproduced with permission of the copyright owner. Further reproduction prohibited without permission.

A comparison between the calculated composition of gaseous precursors adsorbing on the surface and the experimentally-measured relative concentration of bond types in the carbon nitride films may indicate whether a correlation exists between bond types of the adsorbing precursors and bond types in the films. The calculated composition of adsorbing precursors is determined by the mass fluxes of those precursors at the deposition surface. In the calculations, HCN accounts for both C≡N and C=N bonds at the surface, while H_2CN and C_2H_2 account for C=N and C=C bonds, respectively. In that case the calculated relative concentration amounts of C=C:C≡N:C=N do not correlate with the relative amounts of those bonds in the carbon nitride films experimentally measured by Ricci et al. Although Ricci et al. detected significant amounts of C≡N and C=N bonds in the carbon nitride film, the calculated relative amounts of C≡N and C=N bonds are negligible when compared to that of the C=C bond. However, the relative amounts of C≡N:C=N in the solid films can be explained by the calculated mass flux of HCN. The adsorption of HCN primarily accounts for both C≡N and C=N bonds, and the relative amounts of C≡N and C=N bonds formed by adsorbing HCN are believed to be comparable to one another [61]. Since the mass flux of H_2CN is almost two orders of magnitude smaller than that of HCN, the contribution of H_2CN to the formation of C=N bonds may be negligible. The relative concentrations calculated for C–H and N–H bonds are not consistent with the observed results due to the significantly lower mass fluxes of NH, NH_2, and H_2CN than the fluxes of hydrocarbon species at the surface. The relative number of C–N bonds is calculated to be largest among bond types considered in the calculations, although Ricci et al. reported the relative amount of the C–N bond smaller than the amounts of C=C and C=N bonds in the carbon nitride films. The formation of

Reproduced with permission of the copyright owner. Further reproduction prohibited without permission.

observed bond types in the film are therefore primarily due to bond rearrangement occurring on the surface or in the bulk phase once growth precursors are adsorbed on the surface.

2.3.2 Identification of Probable Growth Precursors

Zhang et al. [46] detected the growth of polycrystalline carbon nitride films in a plasma-assisted hot filament CVD reactor using small amounts of CH_4 and NH_3 in an excess of H_2. Operating conditions are chosen to simulate the experiments of Zhang et al., and these are summarized in Table 2.5. A specific degree of H_2 dissociation at the filament is assumed since the actual degree of H_2 dissociation at the filament in Zhang et al.'s reactor was not reported. The degree of H_2 dissociation at $T_f = 2400$ K is approximated using a linear filament poisoning model [63], and $X_{H\infty}$ is found to be 0.1. Two other values, $X_{H\infty} = 0.05$ and 0.15, are also chosen for the calculations to account for some uncertainty in the actual degree of H_2 dissociation.

Table 2.5 Operating conditions chosen to simulate the experiments of Zhang et al.

Reactor pressure P (Torr)	0.9
Filament temperature T_f (K)	2400
Substrate temperature T_s (K)	1200
Inlet mole fractions	
CH_4 $X_{CH_4 \infty}$	0.0033
N_2 $X_{NH_3 \infty}$	0.0167
$H+H_2$ $X_{H_2 \infty} + X_{H \infty}$	0.98
Inlet axial gas velocity U (cm/s)	1.0
Total volume flow rate Q_t (sccm)	150

Probable gaseous film growth precursors are identified by comparing the predicted growth for the assumed growth precursors to the 1.2 μm/h growth rate observed by

Reproduced with permission of the copyright owner. Further reproduction prohibited without permission.

Zhang et al. Gas species having relatively high near-surface mole fractions and sticking probabilities are investigated as potential growth precursors, and these are CH_x (x = 0,2,3), C_2H_2, NH_x (x = 0-2), and H_xCN (x = 1,2). Methane and ammonia are not considered as potential growth precursors because of relatively higher stability of those chemical bonds than radicals considered in the model.

The predicted film growth for the assumed film growth precursors is shown in Figure 2.2. In Figure 2.2a the predicted growth rates due to CH_x (x = 0,2,3) and C_2H_2 are shown as functions of the inlet atomic hydrogen concentration. For the sticking probabilities used for CH_x (x = 0,2,3) and C_2H_2, the contribution of carbon into the film growth is dominated by CH_3 and C, with much smaller contributions from CH_2 and C_2H_2. The predicted growth rates for these species are strongly dependent on $X_{H\infty}$. At a lowest value of $X_{H\infty}$, 0.05, the growth rate due to CH_3 is predicted to be the highest among CH_x (x = 0,2,3) and C_2H_2, with a value of 0.98 μm/h. When $X_{H\infty}$ is increased to 0.15, the predicted film growth rate due to C rather than CH_3 is the highest at 1.23 μm/h, while the growth rate from CH_3 decreases to 0.35 μm/h. When the sum of predicted film growth rates for CH_x (x = 0,2,3) and C_2H_2 is considered, the value is 1.08, 1.2, and 1.72 μm/h for $X_{H\infty}$ = 0.05, 0.1, and 0.15, respectively. The 1.2 μm/h growth rate reported by Zhang et al. can be explained by the sum of predicted growth rates due to CH_x (x = 0,2,3) and C_2H_2 at $X_{H\infty}$ = 0.1. At this H mole fraction, nearly 92% of the deposited carbon comes from C and CH_3. Figure 2.2b shows that, for NH_x (x = 0-2) and H_xCN (x = 1,2), the contribution to carbon nitride growth from atomic nitrogen is significant. The predicted film growth

Reproduced with permission of the copyright owner. Further reproduction prohibited without permission.

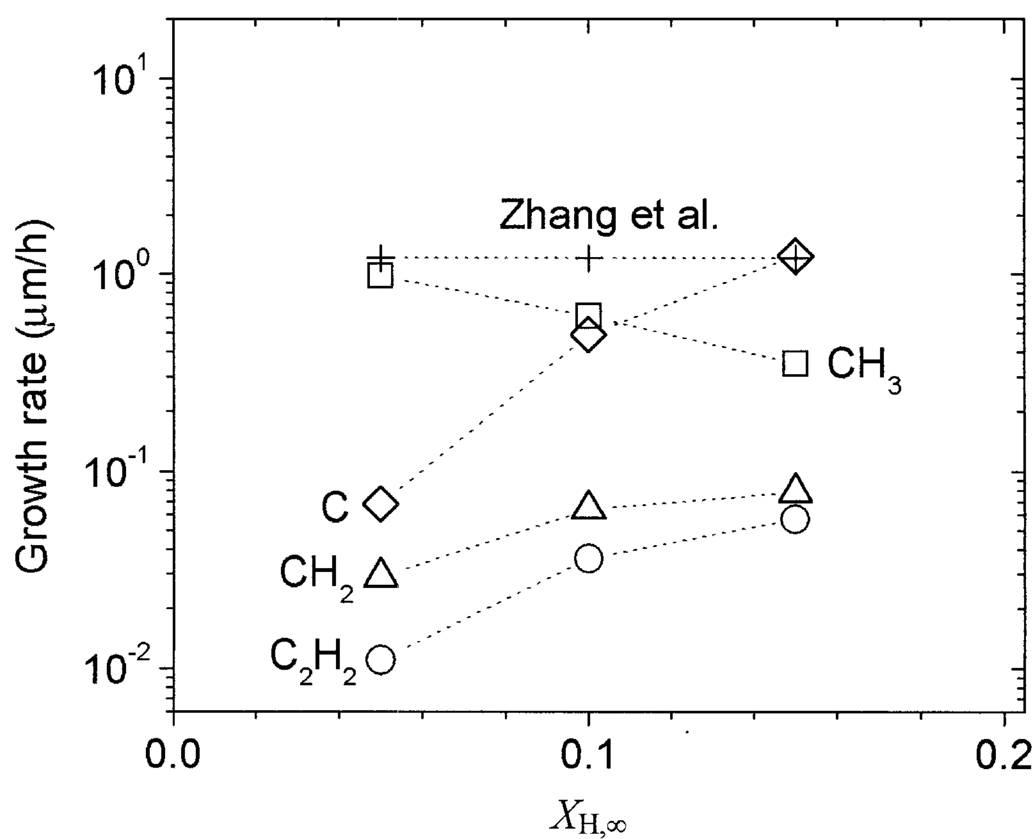

Figure 2.2a Film growth rates due to potential gaseous film growth precursors, CH_x (x = 0,2,3) and C_2H_2.

Reproduced with permission of the copyright owner. Further reproduction prohibited without permission.

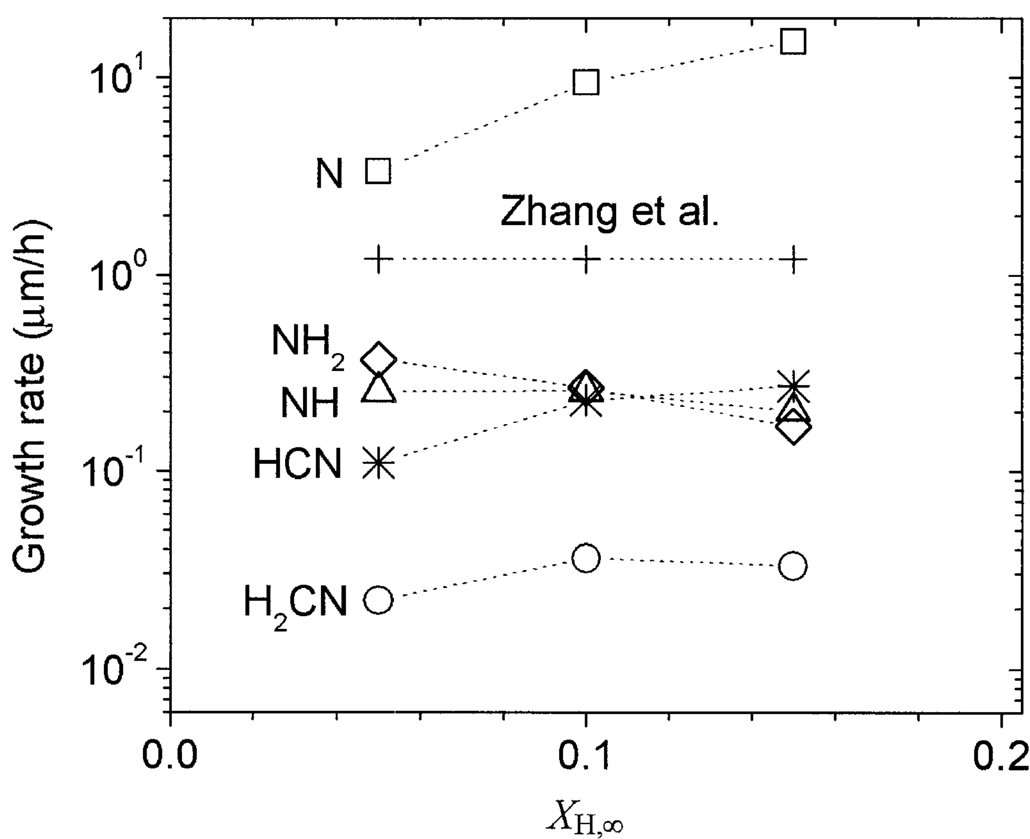

Figure 2.2b Film growth rates due to potential gaseous film growth precursors, NH_x (x = 0-2) and H_xCN (x = 1,2).

Reproduced with permission of the copyright owner. Further reproduction prohibited without permission.

rate for atomic nitrogen is always higher than 1.2 μm/h for the operating conditions used in the calculations, and the value due to N is approximately 3.4 μm/h at the lowest value of $X_{H\infty}$, 0.05. However, the growth rate due to N increases as $X_{H\infty}$ is increased, and the value is approximately 15.2 μm/h at the highest value of $X_{H\infty}$, 0.15. The contributions of other assumed growth species NH_x (x =1,2) and H_xCN (x = 1,2) are much smaller than that of N.

From the film growth rates predicted using the assumed sticking probabilities, it is found that the film growth is limited by the contribution of carbon bearing species into the film growth for the operating conditions used by Zhang et al. This result is expected because of the inlet composition used by Zhang et al. The inlet nitrogen source is introduced as NH_3 instead of N_2 in a large excess of H_2, and the inlet mole fraction of NH_3 is 5 times higher than the inlet carbon source, CH_4. Thus, a high concentration of N in the gas phase is produced through hydrogen abstraction reactions. The nitrogen deficiency in the carbon nitride films have been reported by numerous investigators, and Zhang et al. used a large amount of NH_3 at the inlet to overcome this deficiency.

2.3.3 Effects of Operating Conditions

The growth rate of the carbon nitride film can be maximized when the near-surface concentrations of probable growth precursors are optimized. To achieve the task, calculations are performed to examine the effects of the operating parameters such as the inlet and substrate temperatures, reactor pressure, and inlet gas compositions on the near-surface concentrations of potential growth precursors determined from the growth rate calculations. The values of operating parameters are chosen to match existing experimental data.

Reproduced with permission of the copyright owner. Further reproduction prohibited without permission.

Two inlet temperatures, T_∞ = 2400 and 3300 K, are chosen to investigate the sensitivity of the gas phase chemistry to this parameter. Matsumoto et al. [40] used an inlet temperature of 3300 K in a series of experiments designed to synthesize a polycrystalline β-C_3N_4 film in a plasma-assisted CVD reactor. Zhang et al. [46] chose a filament temperature of 2400 K in their attempts to synthesize crystalline β-C_3N_4 in a hot filament CVD reactor. Inlet temperatures above 3300 K are not considered in the calculations because this value is near the upper limit for which gas-phase kinetic data are reliable. Calculations are also performed for two different values of the substrate temperature, T_s = 300 K and 1200 K. The lower limit of substrate temperature, 300 K, was used in several experimental studies that used plasma CVD reactors [5,13,16], and the upper temperature limit, 1200 K, was used by Zhang et al. [46]. However, when calculations are performed for the different inlet temperatures, the near-surface concentrations of probable growth precursors are found to be only weakly dependent on that temperature for the reactant gaseous mixture of $CH_4/NH_3/H_2$.

The reactor pressure is varied between 0.76 and 76 Torr. Yen and Chou [40] used a pressure of approximately 60 Torr in carbon nitride deposition experiments. At the lower pressure limit, Zhang et al. [46] and Ricci et al. [14] reported pressures of approximately 0.76 Torr.

In existing experiments related to carbon nitride synthesis via CVD, the reactant gases are either $CH_4/NH_3/H_2$ or CH_4/N_2. Effects of the inlet composition on the near-surface concentrations of probable growth precursors are studied in the present study by varying the inlet molecule ratios $NH_3:CH_4$ and $N_2:CH_4$, which are varied from 0.2 to 5. The upper limit is the value used by Zhang et al. [46] and also close to the value used by

Reproduced with permission of the copyright owner. Further reproduction prohibited without permission.

Ricci et al. [14]. The lower limit is chosen solely to examine effects of relatively low nitrogen inlet concentration on the near-surface composition. The sum of the inlet mole fractions of CH_4 and NH_3, $X_{CH_4\infty}+X_{NH_3\infty}$, is fixed at 0.02 for the reactant gaseous mixture of $CH_4/NH_3/H_2$ in accordance with the experimental data of Zhang et al. [46].

The effect of the degree of hydrogen dissociation on the near-surface concentrations of probable growth precursors is studied by varying the inlet mole fractions of H and H_2; the inlet mole fraction of H is varied from 0.05 to 0.25, where the sum of inlet mole fractions of H_2 and H is fixed at 0.98. Another calculation is carried out to examine effects of inlet mole fractions of $H+H_2$ and NH_3+CH_4 on the gas phase chemistry in the gaseous mixture of $CH_4/NH_3/H_2$; the inlet mole fraction of ($H+H_2$, NH_3+CH_4) is varied from (0.02, 0.98) to (0.998, 0.002).

The initial focus of the calculations is to determine the effect of the degree of H_2 dissociation at the inlet on the near-surface concentrations of probable growth precursors. The predicted mole fractions of the potential growth precursors at the deposition surface are shown in Figure 2.3 as functions of the inlet H mole fraction. When $X_{H\infty} \leq 0.1$, the most prevalent potential growth precursor among CH_x species is CH_3. The mole fraction of CH_3 at the deposition surface, denoted as $X_{CH_3 s}$, decreases almost linearly with increaseing $X_{H\infty}$ because the rate of H abstraction from CH_3 increases as $X_{H\infty}$ is increased. When $X_{H\infty} \geq 0.15$, C is the most prevalent potential growth species among the CH_x species because of the rapid H abstraction reactions. The other potential growth species, CH_2, is primarily formed by the H abstraction from CH_3. Among acetyl species, the mole fraction of C_2H_2 at the deposition surface is comparable with the values of C and CH_3.

Reproduced with permission of the copyright owner. Further reproduction prohibited without permission.

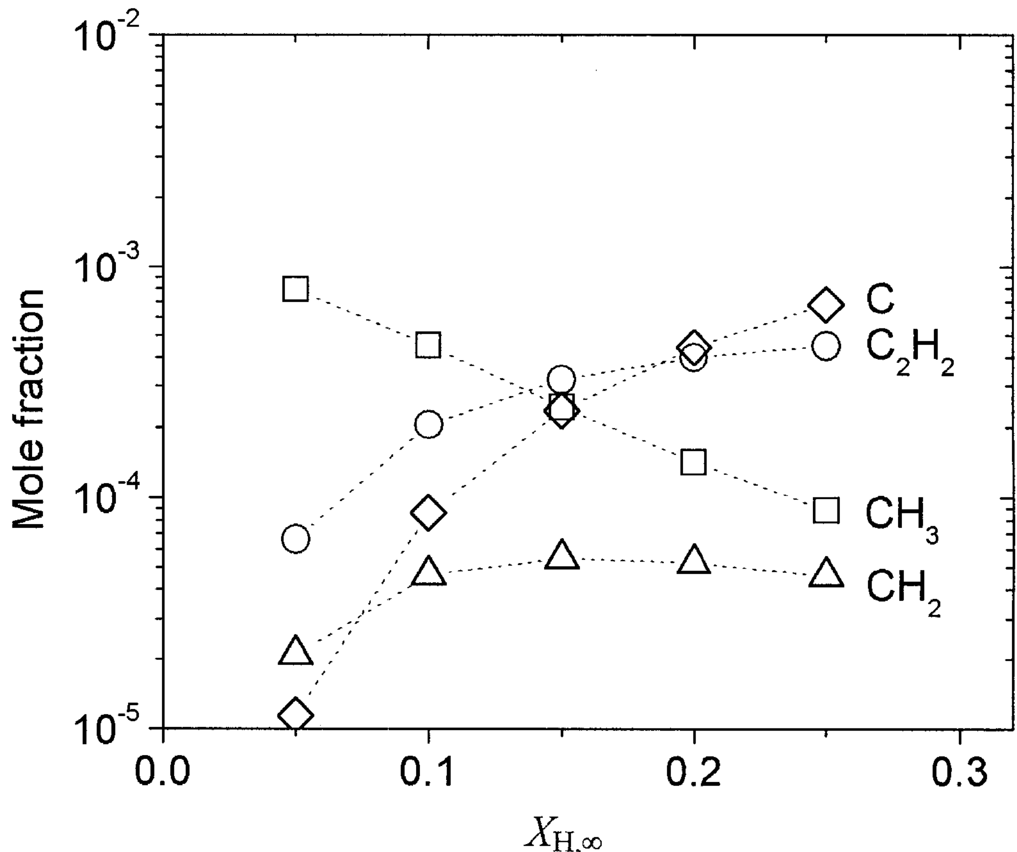

Figure 2.3a Mole fractions of potential gaseous film growth precursors at the deposition surface corresponding to the operating conditions: T_∞ = 2400 K; T_s = 1200 K; P = 0.76 Torr; L = 10 cm; U = 1.0 cm/s and inlet mole fractions: $X_{H\infty} + X_{H_2\infty}$ = 0.98; $X_{NH_3\infty}$ = 1.667×10^{-2}; $X_{CH_4\infty}$ = 3.33×10^{-3}. Calculations were performed for five different H inlet mole fractions: 0.05, 0.10, 0.15, 0.20, and 0.25. Graph shows mole fractions of potential gaseous film growth precursors, CH_x (x = 0,2,3) and C_2H_2.

Reproduced with permission of the copyright owner. Further reproduction prohibited without permission.

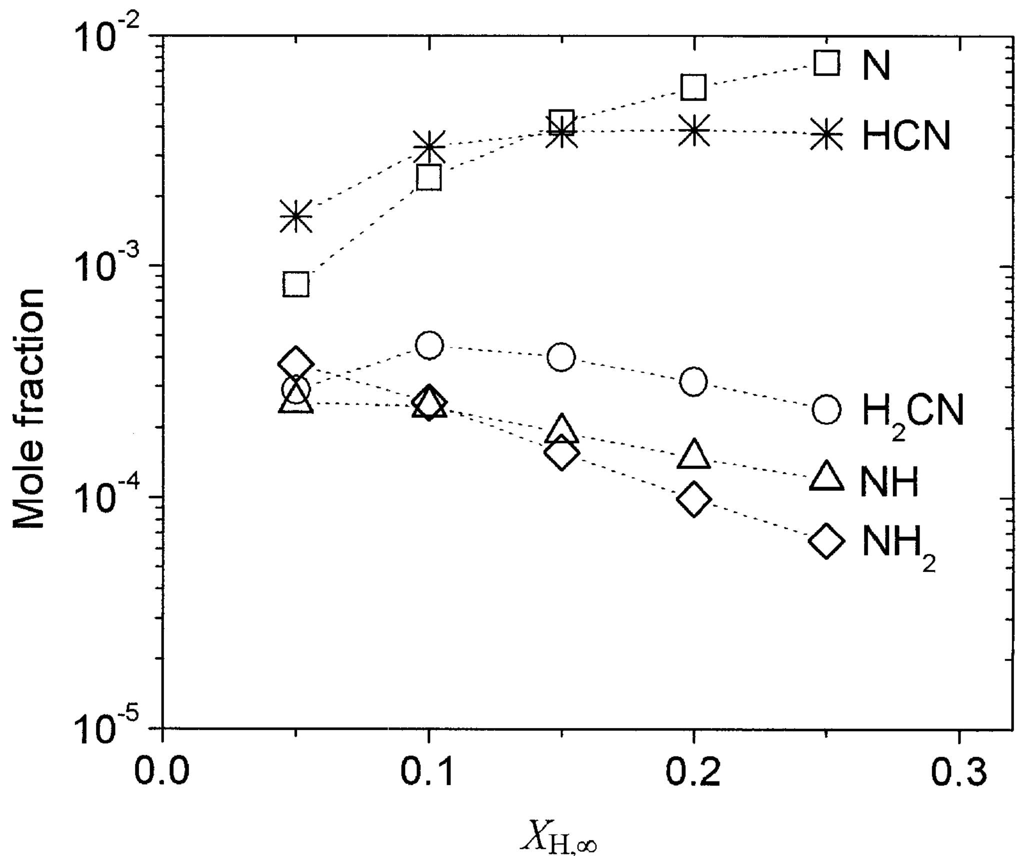

Figure 2.3b Mole fractions of potential gaseous film growth precursors at the deposition surface corresponding to the operating conditions: T_∞ = 2400 K; T_s = 1200 K; P = 0.76 Torr; L = 10 cm; U = 1.0 cm/s and inlet mole fractions: $X_{H\infty} + X_{H_2\infty}$ = 0.98; $X_{NH_3\infty}$ = 1.667×10^{-2}; $X_{CH_4\infty}$ = 3.33×10^{-3}. Calculations were performed for five different H inlet mole fractions: 0.05, 0.10, 0.15, 0.20, and 0.25. Graph shows mole fractions of potential gaseous film growth precursors, NH_x (x = 0-2) and H_xCN (x = 1,2).

Reproduced with permission of the copyright owner. Further reproduction prohibited without permission.

Atomic nitrogen is the dominant nitrogen bearing species at the surface. The H abstraction reactions from NH_3 produce NH and NH_2. However, the mole fraction of N is at least 2 times greater than NH and NH_2 at $X_{H\infty} = 0.05$, and the differences increase as $X_{H\infty}$ increases; the mole fraction of N is more than one and two orders of magnitude greater than NH and NH_2, respectively, at the highest value of $X_{H\infty}$. Other gas species considered as possible candidates for carbon nitride growth species, H_xCN (x =1,2), are present at the surface in sufficiently large concentrations. The formation of HCN and H_2CN are promoted by high concentrations of CH_3, CH_2, and N. The H_2CN formation reaction is followed by the H abstraction reaction enhanced by high atomic hydrogen concentrations.

In Figure 2.4 the mole fractions of potential growth precursors at the deposition surface are shown as functions of the inlet molecule ratio NH_3:CH_4, denoted as $X_{NH_3\infty}/X_{CH_4\infty}$. The inlet concentrations of H and H_2 are fixed at $X_{H\infty} = 0.10$ and $X_{H_2\infty} = 0.88$. The mole fractions of CH_x species at the surface decrease as the inlet NH_3:CH_4 increases, and these decreases result in decreases in the mole fractions of C_2H_x species because of the reactions forming the C_2H_x species from the CH_x species. The mole fractions of HCN and H_2CN are maximized when $X_{NH_3\infty}/X_{CH_4\infty} = 1$.

The effects of inlet mole fractions of (H + H_2, NH_3 + CH_4) on the gas composition at the surface are shown in Figure 2.5. The inlet mole fraction of H and H_2, $X_{H+H_2\infty}$, is varied from 0.02 to 0.998, where the inlet molecular ratio H:H_2, $X_{H\infty}/X_{H_2\infty}$, is fixed at 0.1/0.88. The potential growth precursors, except atomic carbon and nitrogen, are maxim-

Reproduced with permission of the copyright owner. Further reproduction prohibited without permission.

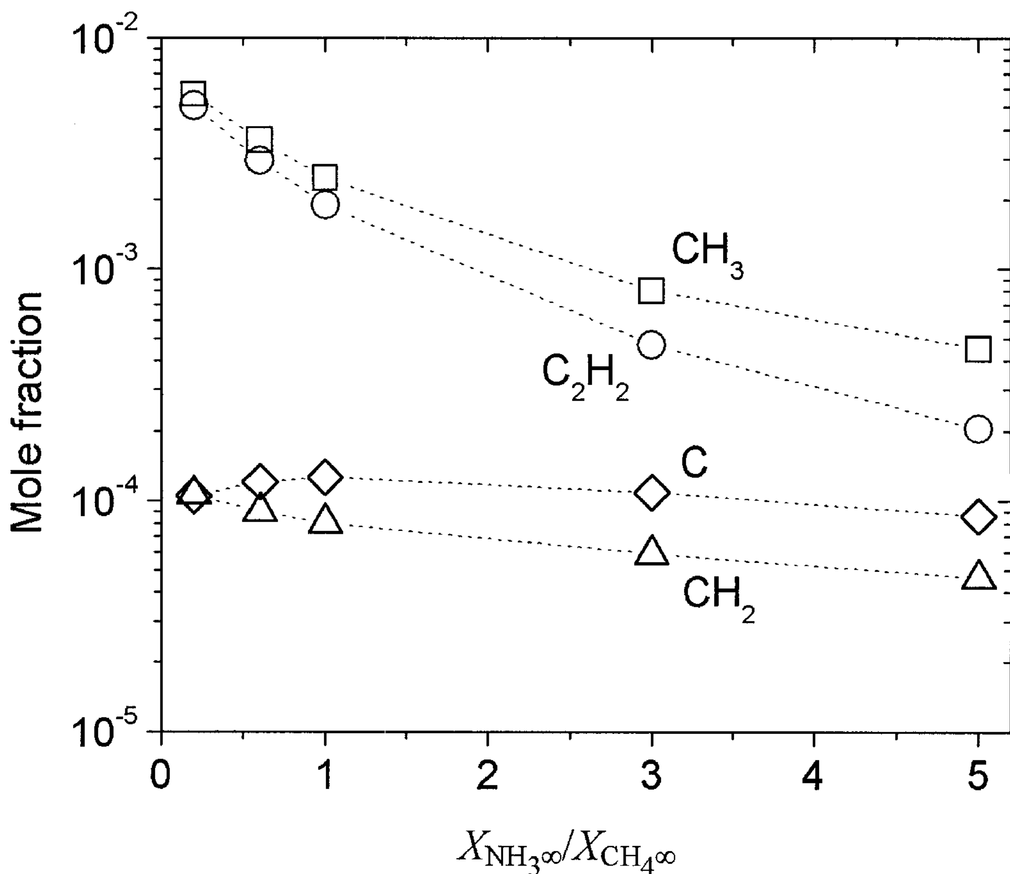

Figure 2.4a Mole fractions of potential gaseous film growth precursors at the deposition surface corresponding to the operating conditions described in Figure 2.3, with five different inlet molecule ratios of NH_3 to CH_4: 0.2, 0.6, 1.0, 3.0, and 5.0. Graph shows mole fractions of potential film growth precursors, CH_x (x = 0,2,3) and C_2H_2.

Reproduced with permission of the copyright owner. Further reproduction prohibited without permission.

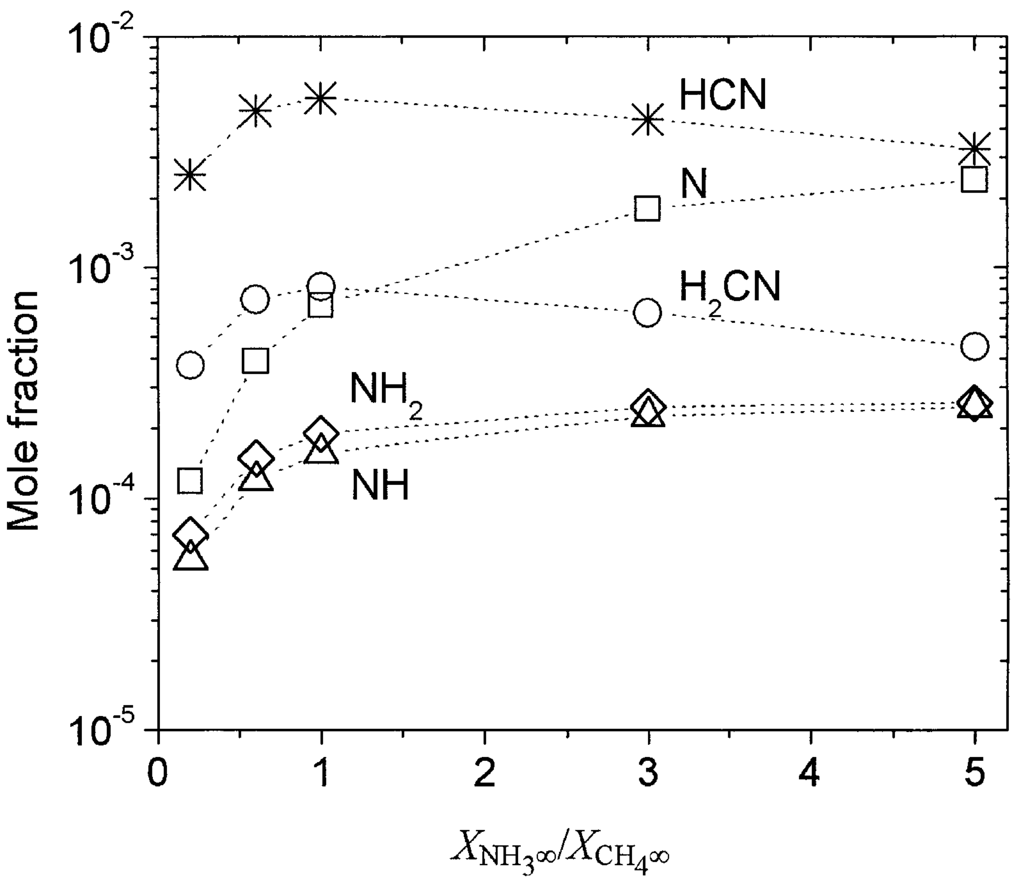

Figure 2.4b Mole fractions of potential gaseous film growth precursors at the deposition surface corresponding to the operating conditions described in Figure 2.3, with five different inlet molecule ratios of NH_3 to CH_4: 0.2, 0.6, 1.0, 3.0, and 5.0. Graph shows mole fractions of potential film growth precursors, NH_x (x = 0-2) and H_xCN (x = 1,2).

Reproduced with permission of the copyright owner. Further reproduction prohibited without permission.

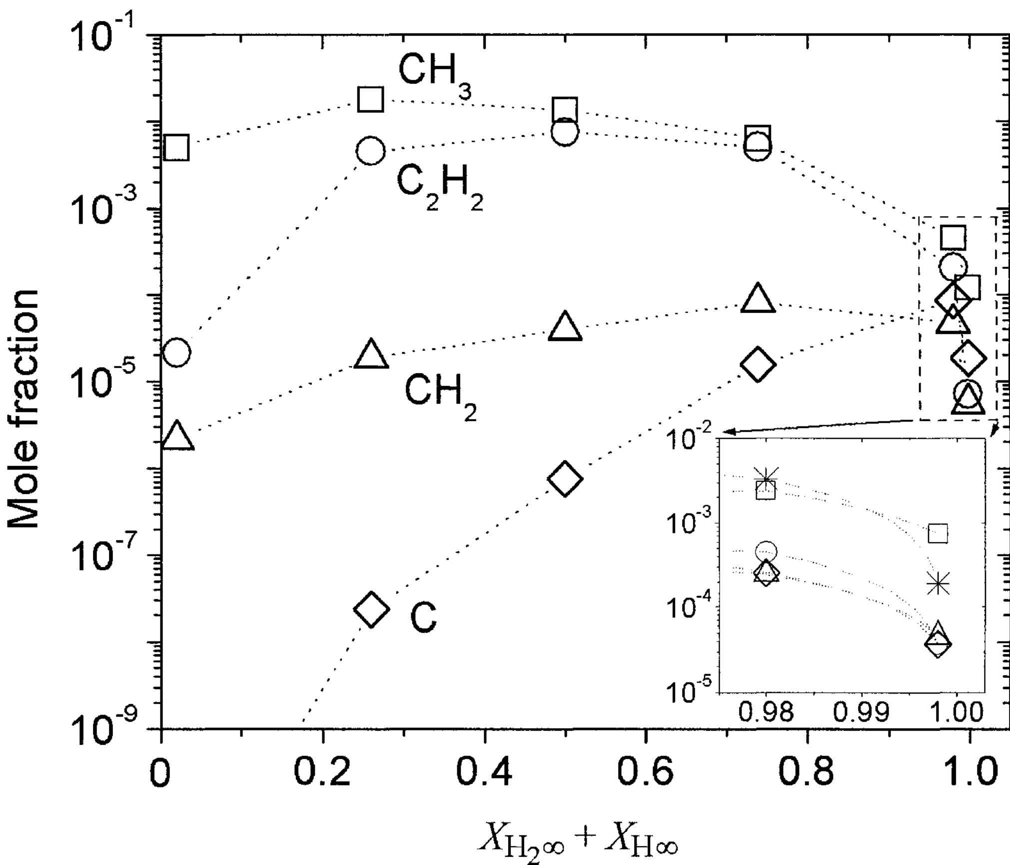

Figure 2.5a Mole fractions of potential gaseous film growth precursors at the deposition surface corresponding to the operating conditions described in Figure 2.3. Calculations were performed for six different inlet mole fractions of ($H+H_2$, NH_3+CH_4): (0.998, 0.002), (0.98, 0.02), (0.74, 0.26), (0.50, 0.50), (0.26, 0.74), and (0.02, 0.98). Graph shows mole fractions of potential film growth precursors, CH_x ($x = 0,2,3$) and C_2H_2.

Reproduced with permission of the copyright owner. Further reproduction prohibited without permission.

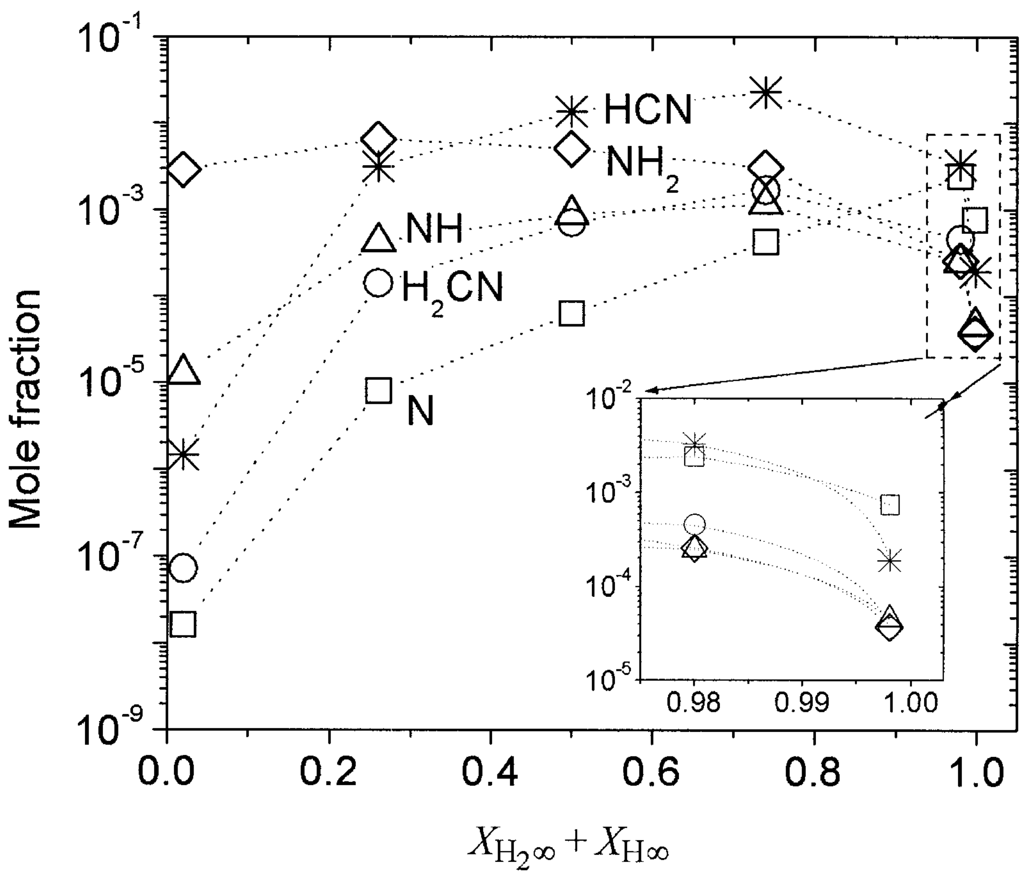

$X_{H_2\infty} + X_{H\infty}$

Figure 2.5b Mole fractions of potential gaseous film growth precursors at the deposition surface corresponding to the operating conditions described in Figure 2.3. Calculations were performed for six different inlet mole fractions of ($H+H_2$, NH_3+CH_4): (0.998, 0.002), (0.98, 0.02), (0.74, 0.26), (0.50, 0.50), (0.26, 0.74), and (0.02, 0.98). Graph shows mole fractions of potential film growth precursors, NH_x (x = 0-2) and H_xCN (x = 1,2).

Reproduced with permission of the copyright owner. Further reproduction prohibited without permission.

ized when $0.26 \leq X_{H+H_2\infty} \leq 0.74$, and the mole fractions of these precursors, however, are significant reduced when $X_{H+H_2\infty} \geq 0.98$. Among the growth precursors, CH_3 and NH_2 are maximized at $X_{H+H_2\infty} = 0.26$ where $X_{H\infty} = 0.027$, while CH_2, NH, HCN, and H_2CN are maximized at $X_{H+H_2\infty} = 0.74$ where $X_{H\infty} = 0.076$. The growth precursor among acetyl species, C_2H_2, is maximized at $X_{H+H_2\infty} = 0.5$ where $X_{H\infty} = 0.05$. However, atomic carbon and nitrogen are maximized at $X_{H+H_2\infty} = 0.98$ where $X_{H\infty} = 0.1$.

The mole fractions of probable growth precursors at the deposition surface as functions of reactor pressure are shown in Figure 2.6. The mole fractions of CH_x and NH_x species decrease significantly in the region near the surface as pressure is increased from 0.76 to 76 Torr. The mole fraction of CH_3 present at the surface decreases by over two orders of magnitude when P is increased from 0.76 to 7.6 Torr. However, the mole fraction decreases less than a factor of 3 when P is increased from 7.6 to 76 Torr, while mole fractions of other CH_x and NH_x species decrease several orders of magnitude. The mole fractions of CH_x and NH_x species at the deposition surface are maximized when P = 0.76 Torr. The mole fractions $X_{C_2H_2s}$ and X_{HCNs} are not strongly affected by the change of pressure.

The mole fractions of probable growth precursors at the deposition surface as functions of the substrate temperature are shown in Figure 2.7. The mole fraction of C decreases by an order of magnitude when T_s is raised from 300 to 1200 K, and at the same time the mole fraction of CH_3 increases by an order of magnitude. The mole fract-

Reproduced with permission of the copyright owner. Further reproduction prohibited without permission.

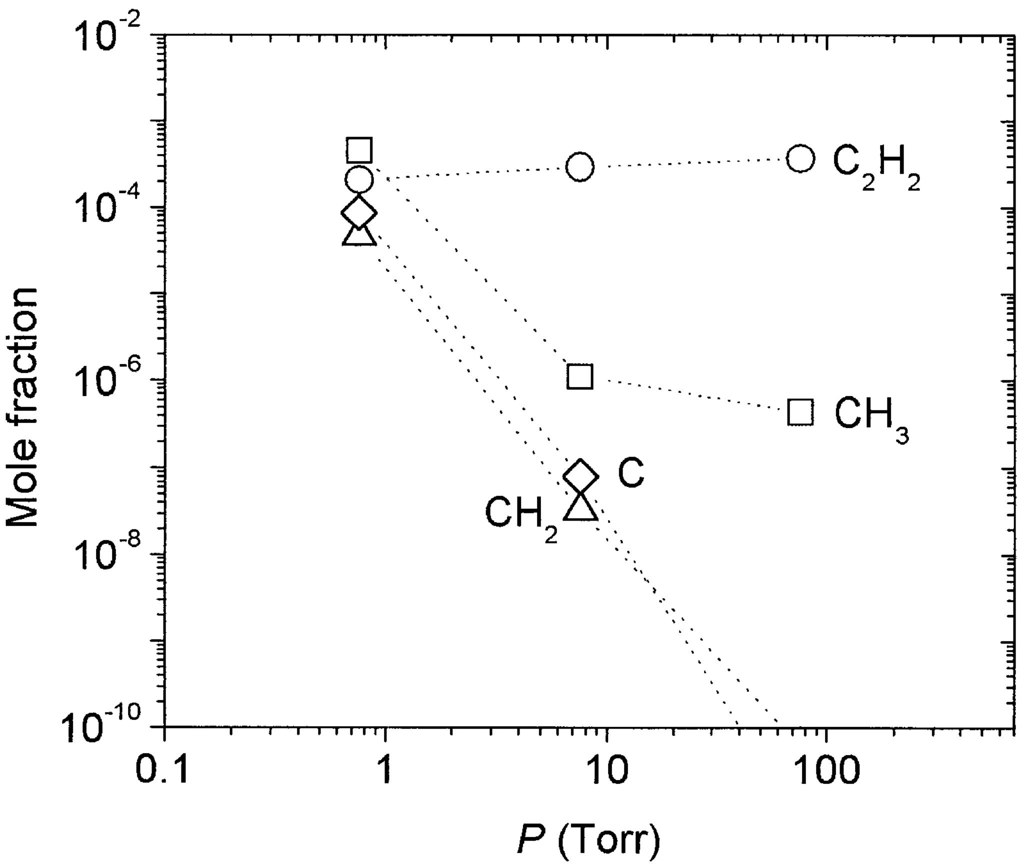

Figure 2.6a Mole fractions of potential gaseous film growth precursors at the deposition surface corresponding to the operating conditions described in Figure 2.3. Calculations were performed for three different reactor pressure values: 0.76, 7.6, and 76 Torr. Graph shows mole fractions of potential film growth precursors, CH_x (x = 0,2,3) and C_2H_2.

Reproduced with permission of the copyright owner. Further reproduction prohibited without permission.

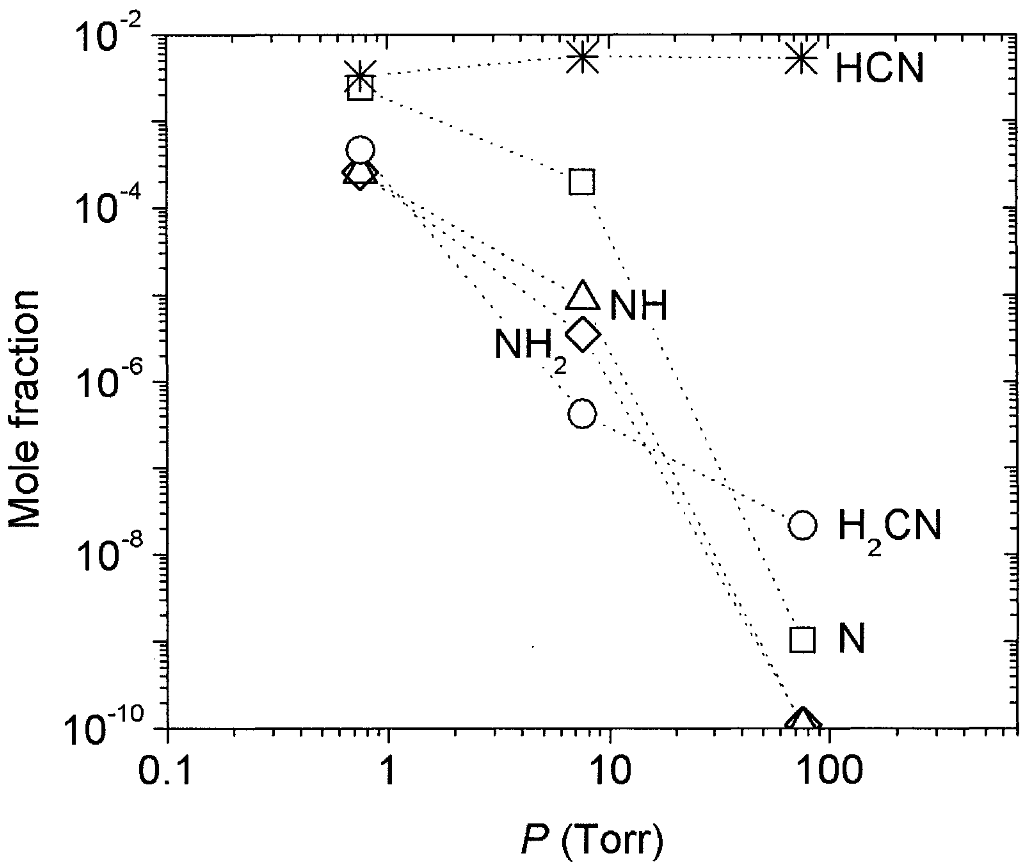

Figure 2.6b Mole fractions of potential gaseous film growth precursors at the deposition surface corresponding to the operating conditions described in Figure 2.3. Calculations were performed for three different reactor pressure values: 0.76, 7.6, and 76 Torr. Graph shows mole fractions of potential film growth precursors, NH_x (x = 0-2) and H_xCN (x = 1,2).

Reproduced with permission of the copyright owner. Further reproduction prohibited without permission.

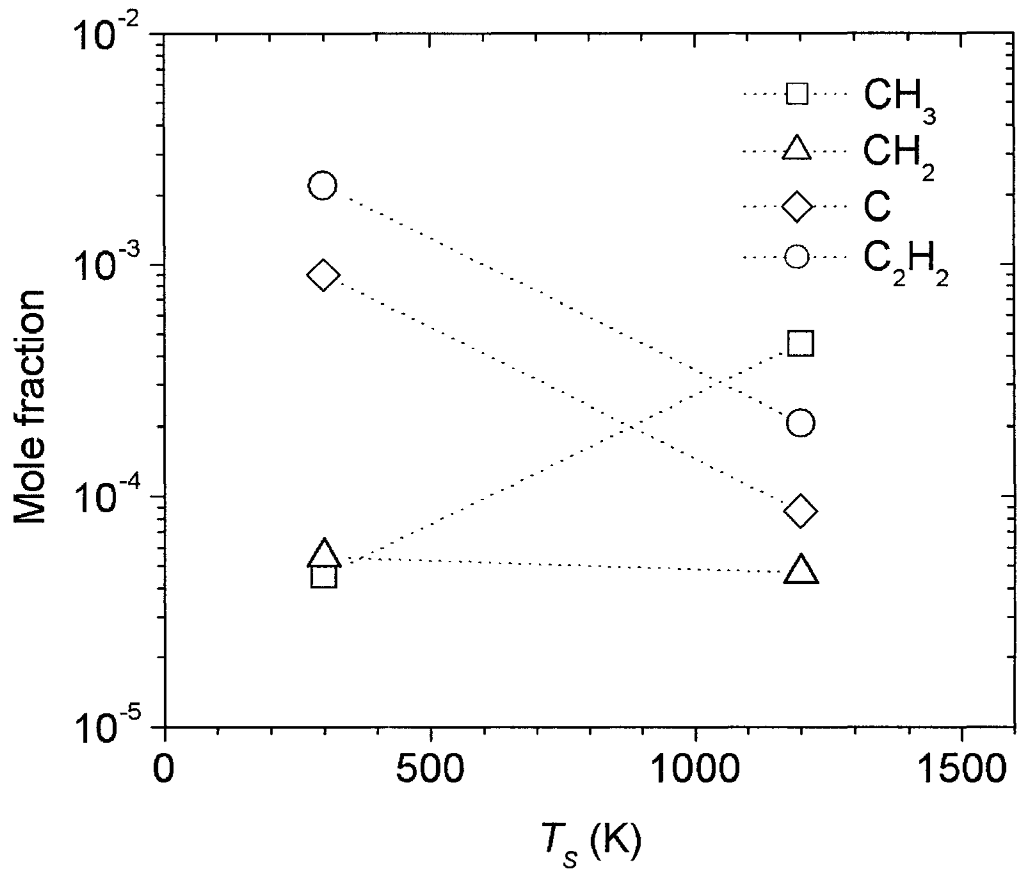

Figure 2.7a Mole fractions of potential gaseous film growth precursors at the deposition surface corresponding to the operating conditions described in Figure 2.3, with two different substrate temperature: 300 and 1200 K. Graph shows mole fractions of potential growth precursors, CH_x ($x = 0,2,3$) and C_2H_2.

Reproduced with permission of the copyright owner. Further reproduction prohibited without permission.

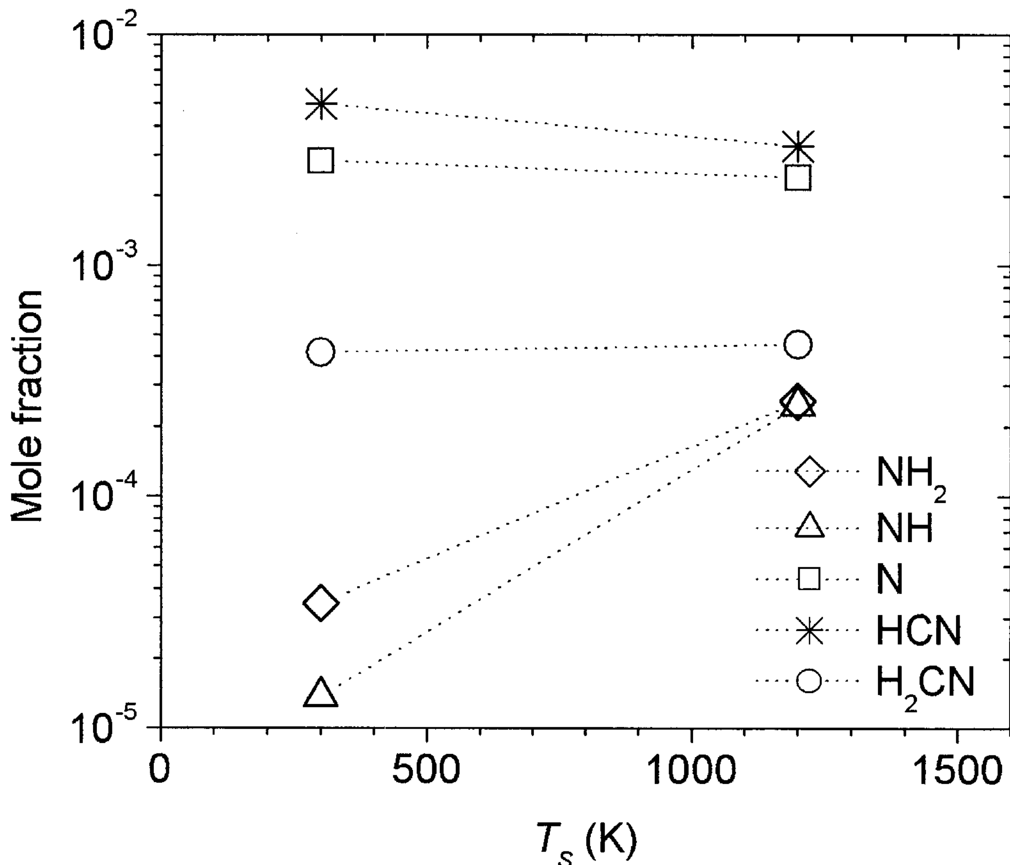

Figure 2.7b Mole fractions of potential gaseous film growth precursors at the deposition surface corresponding to the operating conditions described in Figure 2.3, with two different substrate temperature: 300 and 1200 K. Graph shows mole fractions of potential growth precursors, NH_x (x = 0-2) and H_xCN (x = 1,2).

Reproduced with permission of the copyright owner. Further reproduction prohibited without permission.

ions of NH and NH_2 increase by about an order of magnitude when T_s is raised to 1200 K, while the mole fraction of C_2H_2 decreases as T_s is increased. The mole fractions of CH_2, N, HCN, and H_2CN are weakly affected by the change of T_s.

The gas composition is strongly affected by changing the inlet gaseous mixture from $NH_3/CH_4/H_2$ to N_2/CH_4. Without the introduction of H_2 or H at the inlet, the reactions of the relatively stable species N_2 with other reactive species are inhibited until CH_4 undergoes unimolecular decomposition to produce sufficient concentrations of H and reactive carbon bearing species. This inhibits the formation of atomic nitrogen, which in turn suppresses the reactions that produce NH_x and H_xCN species. Therefore, $X_{NH_x s}$ and $X_{H_xCN s}$ are much lower for N_2/CH_4 reactants than for $NH_3/CH_4/H_2$. The dissociation of N_2 to form other nitrogen bearing species is not strongly affected by the change in the substrate temperature, while the amount increased more than 11 times when the inlet temperature is increased from 2400 to 3300 K. When the inlet molecule ratio $N_2:CH_4$ is varied from 0.2 to 5, the dissociation amount of N_2 increases by a factor of 57. However, the amount is most strongly dependent on the reactor pressure, increasing by a factor of 61 when P is increased from 0.76 to 76 Torr. The maximum degree of N_2 dissociation is 0.01% at a pressure of 76 Torr.

2.4 Conclusion

A model has been developed to investigate CVD growth of carbon nitride under conditions representative of those used in published experimental studies. The model has been applied to predict the gas phase chemistry, temperature and velocity profiles, poten-

Reproduced with permission of the copyright owner. Further reproduction prohibited without permission.

tial gaseous film growth precursors, and to evaluate the likelihood of bond rearrangement occurring in the bulk phase or on the deposition surface subsequent to the adsorption of the gaseous precursors.

The experimental results of Ricci et al. [14] and Zhang et al. [46] have been compared to the model predictions to investigate the most likely gaseous species leading to carbon nitride film growth, and to examine the degree to which bond rearrangement occurs subsequent to adsorption of the precursors. Also, the model has been applied to investigate the effects of various operating conditions—the inlet and the substrate temperatures, the reactor pressure, and the inlet gas composition—on the near-surface concentrations of potential gaseous film growth precursors.

When the calculated gas composition due to assumed carbon nitride growth species are compared to the experimental data of Ricci et al. [14], no correlation between bond types of presumed growth precursors adsorbing on the surface and bond types in the film is found. The bond types measured in the experimentally grown film must therefore result from chemical bond rearrangement occurring after the gaseous precursors are adsorbed.

Calculations are also performed for the experimental conditions of Zhang et al. [46] to identify the most probable growth precursors. The carbon nitride growth rates are calculated by using sticking probabilities chosen for presumed growth precursors. The carbon contribution to the film growth is dominated by C and CH_3 species with much smaller contributions from CH_2 and C_2H_2. The sum of film growth rates due to the carbon bearing species at $X_{H\infty} = 0.1$ matches the 1.2 μm/h growth rate reported by Zhang et al. However, atomic nitrogen is the primary nitrogen bearing species responsible for the film growth with much smaller contributions of other assumed growth species NH, NH_2,

Reproduced with permission of the copyright owner. Further reproduction prohibited without permission.

HCN, and H_2CN, and the predicted film growth rate for atomic nitrogen is always greater than 1.2 μm/h for the operating conditions used in the calculations.

When calculations are performed for different inlet gas compositions, the near-surface concentrations of potential gaseous film growth precursors are strongly affected by changing inlet gas composition. Molecular nitrogen is not a promising nitrogen source for carbon nitride growth via CVD due to the negligible dissociation amount of the molecule. The concentrations of potential growth precursors are also strongly dependent on the reactor pressure. In the calculations done here, the dissociation degree of N_2 is maximized at P = 76 Torr. The effects of different inlet temperatures on the near-surface concentrations of potential growth precursors are not significant, while the near-surface concentrations are found to be a function of the substrate temperature.

In this investigation, a detailed study of carbon nitride CVD from the reactant gaseous mixture $CH_4/NH_3/H_2$ has been carried out to identify the range of operating conditions in which carbon nitride can be deposited from probable film growth precursors, since the negligible dissociation amount of N_2 has limited the use of this species as a nitrogen source. The relative contributions of potential film growth precursors to carbon nitride deposition are determined by their mass fluxes at the deposition surface. The high growth rates predicted with gaseous precursors C, CH_3, and N strongly suggest that carbon nitride is deposited through two separate reaction sequences—one involving the contribution of carbon bearing species C and CH_3 and the other the contribution of N—that occur in parallel. For the range of operating conditions considered here, signify-cant variation of precursor near-surface concentrations is predicted to occur, depending on substrate temperature, reactor pressure, and inlet gas composition. An increase in the

Reproduced with permission of the copyright owner. Further reproduction prohibited without permission.

substrate temperature from 300 to 1200 K leads to a transition of the most probable carbon bearing precursor from C to CH_3. However, the near-surface concentration of the primary nitrogen bearing species, N, is only weakly dependent on substrate temperature. As the reactor pressure is decreased from 76 to 0.76 Torr, the significant increase in the film growth rate can be explained by the increase in the near-surface concentrations of all three potential film growth precursors, C, CH_3, and N. In examining the dependence of the precursor near-surface concentrations on inlet gas composition, it is found that the concentrations of C and N are maximized when $X_{H\infty} = 0.25$ and $X_{H+H_2\infty} = 0.98$. However, as either $X_{H\infty}$ or $X_{H+H_2\infty}$ decreases, the primary carbon bearing species for carbon nitride growth changes from C to CH_3. A transition in the film composition from a CN_x film deficient in nitrogen to stoichiometric β-C_3N_4 can be accomplished by increasing the near-surface concentration of N through use of a high NH_3:CH4 inlet molecule ratio.

Reproduced with permission of the copyright owner. Further reproduction prohibited without permission.

2.5 References

1. M.L. Cohen, Phys. Rev. B **32**, 7988 (1985).
2. Y. Liu and M.L. Cohen, Science **245**, 841 (1989).
3. Y. Liu and M.L. Cohen, Phys. Rev. B **41**, 10727 (1990).
4. Y. Liu and R.M. Wentzcovitch, Phys. Rev. B **50**, 10362 (1994).
5. Y. Guo and W.A. Goddard III, Chem. Phys. Lett. **237**, 72 (1995).
6. H.X. Han and B.J. Feldman, Solid State Commun. **65**, 921 (1988).
7. T. Sekine, H. Kanda, Y. Banda, M. Yokoyama, and K. Hojou, J. Mater. Sci. Lett. **9**, 1376 (1990).
8. M.R. Wixom, J. Amer. Ceram. Soc. **73**, 1973 (1990).
9. M.Y. Chen, X. Lin, V.P. Dravid, Y.W. Chung, M.S. Wong, and W.D. Sproul, J. Vac. Sci. Technol. A **11**, 521 (1993).
10. L. Maya, D.R. Cole, and E.W. Hagaman, J. Amer. Ceram. Soc. **74**, 1686 (1991).
11. S. Kumar and T.L. Transley, Solid State Commun. **88**, 803 (1993).
12. F. Fujimoto and K. Ogata, Jpn. J. Appl. Phys. **32**, L420 (1993).
13. J.F.D. Chubachi, T. Sakai, T. Yamamoto, K. Ogata, A. Ebe, and F. Fujimoto, Nucl. Instrum. Methods B **80/81**, 463 (1993).
14. M. Ricci, M. Trinquecoste, F. Auguste, R. Canet, P. Delhaes, C. Guimon, G.P. Guillouzo, B. Nysten, and J.P. Issi, J. Mater. Res. **8**, 480 (1993).
15. D. Li, Y.W. Chung, M.S. Wong, and W.D. Sproul, J. Appl. Phys. **74**, 219 (1993).
16. K. Ogata, J.F. Diniz-Chubaci, and F. Fujimoto, J. Appl. Phys. **76**, 3791 (1994).

Reproduced with permission of the copyright owner. Further reproduction prohibited without permission.

17. M. Diani, A. Mansour, L. Kubler, L. Bischoff, and D. Bolmont, Diamond Relat. Mater. **3**, 264 (1994).

18. A. Hoffman, I. Gouzman, and R. Brener, Appl. Phys. Lett. **64**, 845 (1994).

19. A. Bousetta, M. Lu, A. Bensaoula, and A. Schultz, Appl. Phys. Lett. **65**, 696 (1994).

20. S. Kumar and T.L. Tansley, J. Appl. Phys. **76**, 4390 (1994).

21. D. Marton, K.J. Boyd, A.H. Al-Bayati, S.S. Todorov, and J.W. Rabalais, Phys. Rev. Lett. **73**, 118 (1994).

22. J. Furthmuller, J. Hafner, and G. Kresse, Phys. Rev. B **50**, 15606 (1994).

23. Z.M. Ren, Y.C. Du, Y. Qiu, J.D. Wu, Z.F. Ying, X. Xiong, and F.M. Li, Phys. Rev. B **51**, 5274 (1995).

24. M.G. Krishna, K.R. Gunasekhar, and S. Mohan, J. Mater. Res. **10**, 1083 (1995).

25. D. Li, S. Lopez, Y.W. Chung, M.S. Wong, and W.D. Sproul, J. Vac. Sci. Technol. A **13**, 1063 (1995).

26. K.G. Kreider, M.J. Tarlov, G.J. Gillen, G.E. Poirier, L.H. Robins, L.K. Ives, W.D. Bowers, R.B. Marinenko, and D.T. Smith, J. Mater. Res. **10**, 3079 (1995).

27. T. Okada, S. Yamada, Y. Takeuchi, and T. Wada, J. Appl. Phys. **78**, 7416 (1995).

28. S.P. Withrow, J.M. Williams, S. Prawer, and D. Barbara, J. Appl. Phys. **78**, 3060 (1995).

29. A. Bousetta, M. Lu, and A. Bensaoula, J. Vac. Sci. Technol. A **13**, 1639

Reproduced with permission of the copyright owner. Further reproduction prohibited without permission.

(1995).

30. S. Kumar, T.L. Tansley, and L.S. Wielunski, J. Phys. D: Appl. Phys. **28**, 2335 (1995).

31. M. Tabbal, P. Merel, S. Moisa, M. Chaker, A. Ricard, and M. Moisan, Appl. Phys. Lett. **69**, 1698 (1996).

32. L. Wan and R.F. Egerton, Thin Solid Films **279**, 34 (1996).

33. S. Kobayashi, S. Nozaki, H. Morisaki, S. Fukui, and S. Masaki, Thin Solid Films **281-282**, 289 (1996).

34. H. Sjöström, W. Lanford, B. Hjörvarson, K. Xing, and J.E. Sundgren, J. Mater. Res. **11**, 981 (1996).

35. D.F. Franceschini, F.L. Freire, Jr., and S.R.P. Silva, Appl. Phys. Lett. **68**, 2645 (1996).

36. R. Merchant, D.G. McCulloch, D.R. Mckenzie, Y. Yin, L. Hall, and E.G. Gerster, J. Appl. Phys. **79**, 6914 (1996).

37. Z.J. Zhang, S. Fan, J. Huang, and C.M. Lieber, Appl. Phys. Lett. **68**, 2639 (1996).

38. C. Niu, Y.Z. Lu, and C.M. Lieber, Science **261**, 334 (1993).

39. K.M. Yu, M.L. Cohen, E.E. Haller, W.L. Hansen, A.Y. Liu, and I.C. Wu, Phys. Rev. B **49**, 5034 (1994).

40. O. Matsumoto, T. Kotaki, H. Shikano, K. Takemura, and S. Tanaka, J. Electrochem. Soc. **141**, L16 (1994).

41. T.Y. Yen and C.P. Chou, Solid State Comm. **95**, 281 (1995).

42. T.Y. Yen and C. P. Chou, Appl. Phys. Lett. **67**, 2801 (1995).

Reproduced with permission of the copyright owner. Further reproduction prohibited without permission.

43. L.A. Bursill, P.J. Lin, V.N. Gurarie, A.V. Orlov, and S. Prawer, J. Mater. Res. **10**, 2277 (1995).

44. Z.B. Zhang, Y.A. Li, S.S. Xie, and G.Z. Yang, J. Mater. Sci. Lett. **14**, 1742 (1995).

45. Z. Wu, Y. Yu, and X. Liu, Appl. Phys. Lett. **68**, 1291 (1996).

46. Y. Zhang, Z. Zhou, and H. Li, Appl. Phys. Lett. **68**, 634 (1996).

47. M.E. Coltrin, R.J. Kee, G.H. Evans, E. Meeks, F.H. Rupley, and J.F. Grear, Report No. SAND 91-8003 (1991).

48. M.E. Coltrin, R.J. Kee and G.H. Evans, J. Electrochem. Soc. **136**, 819 (1989).

49. M.E. Coltrin and D.S. Dandy, J. Appl. Phys. **74**, 5803 (1993).

50. R.J. Kee, F.M. Rupley and J.A. Miller, Report No. SAND 89-8009B (1993).

51. J.A. Miller and C.F. Melius, Combust. Flame **91**, 21 (1992).

52. P.Glarborg, K.Dam-Johansen, and J.A.Miller, Int. J. Chem. Kinet. **27**, 1207 (1995).

53. L.Prada and J.A.Miller, Combust. Sci. and Tech. **132**, 225 (1998).

54. P.Glarborg, M.U. Alzueta, K.Dam-Johansen, and J.A. Miller, Combust. Flame **115**, 1 (1998).

55. R.J. Kee, G. Dixon-Lewis, J. Warnatz, M.E. Coltrin, and J.A. Miller, Report No. SAND 86-8246, (1986).

56. M.E. Coltrin, R.J. Kee, and F.M. Rupley, Report No. SAND 90-8003 B (1991).

57. C.C. Battaile, D.J. Srolovitz, I.I. Oleinik, D.G. Pettifor, A.P. Sutton, S.J. Harris, and J.E. Butler, J. Chem. Phys. **111**, 4291 (1999).

Reproduced with permission of the copyright owner. Further reproduction prohibited without permission.

58. M.D. Allendorf and R.J. Kee, J. Electrochem. Soc. **138**, 841 (1991).

59. F. Bacalzo-Gladden, X. Lu, and M.C. Lin, J. Phys. Chem. B **105**, 4368 (2001).

60. Y. Bu, L. Ma, and M.C. Lin, J. Phys. Chem. **97**, 7081 (1993).

61. C.L. Levoguer and R.M. Nix, J. Chem. Soc. Faraday Trans. **92**, 4799 (1996).

62. J.H. Cho, L. Kleinman, C.T. Chan, and K.S. Kim, Phys. Rev. B **63**, 3306 (2001).

63. D.S. Dandy and M.E. Coltrin, J. Appl. Phys. **76**, 3102 (1994).

Reproduced with permission of the copyright owner. Further reproduction prohibited without permission.

Chapter 3

A KINETIC MODEL OF DIAMOND NUCLEATION AND SILICON CARBIDE INTERLAYER FORMATION DURING CHEMICAL VAPOR DEPOSITION

3.1 Introduction

Experimental observations [1-41] indicate the presence of an intermediate layer on a non-diamond substrate surface during nucleation and the early stages of diamond deposition in chemical vapor deposition (CVD) processes. It is believed that intermediate layer formation enhances diamond nucleation densities [2,3,42-44] and thus strongly affects the morphology [2,3,42] and orientation [23,28] of diamond films subsequently grown on the intermediate layer. When silicon is used as a substrate for diamond CVD, investigators [14-41] have reported that silicon carbide is the predominant form of the intermediate layer. The formation of SiC intermediate layers during diamond CVD is also supported by quasi-equilibrium thermodynamic predictions [45,46].

It is generally accepted that the SiC intermediate layer is very thin, often in the range of 1 to 10 nm [14,16-18,20,30,34,35]. For example, Sun et al. [34] reported the presence of β-SiC intermediate layers between diamond films and Si substrates in hot-filament CVD (HFCVD) reactors under conditions of 0.5 mol-% inlet CH_4 in H_2, 75 torr, filament temperatures between 2473 and 2673 K, and substrate temperatures between 973 and 1273 K. Thin layers of β-SiC, 1 to 10 nm, were observed in the earliest stages of dia-

The text of Chapter 3 consists of manuscript which has been submitted for publication in thin Solid Films.

Reproduced with permission of the copyright owner. Further reproduction prohibited without permission.

mond deposition. Jiang et al. [30] detected an intermediate layer composed of amorphous and crystalline β-SiC, approximately 10 nm thick, at the interface between a diamond film and a Si substrate in a HFCVD reactor under conditions of 1.0 mol-% inlet CH_4 in H_2 and substrate temperatures between 973 and 1173 K. Belton et al. [17] observed that a SiC intermediate layer thicker than 9 nm developed before diamond could be detected in a HFCVD system using 0.2 mol-% inlet CH_4 in H_2 carrier gas. Stoner et al. [20] reported the formation of amorphous SiC intermediate layers of 1 to 10 nm thick prior to diamond growth using a microwave plasma-assisted CVD (MW PACVD) reactor. The existence of a SiC intermediate layer, approximately 10 nm thick, was also observed in a diamond growth experiment on a Si substrate using MW PACVD by Meilunas et al. [14]. Jubber and Milne [35] reported 5 nm SiC intermediate layers in MW PACVD of diamond.

A variety of CVD techniques are used in the experimental study of the formation of SiC intermediate layers during diamond CVD. Among these techniques, HFCVD is probably the easiest method to understand experimentally and conceptually, as well as one of the simplest and most reproducible methods for diamond deposition at low pressures. Therefore, HFCVD is often used to investigate the nucleation and subsequent growth of diamond on a variety of substrates [47].

In a typical diamond HFCVD process, a gas mixture containing small amount of CH_4 in an excess of H_2 enters a reactor and flows past a high temperature filament. In the gas phase, CH_4 undergoes pyrolysis reactions leading to a distribution of species that includes carbon atoms, hydrocarbon radicals, and stable hydrocarbon species. Gaseous hydrocarbon species flow toward the deposition surface, cooled to temperatures between 973 and 1273 K, and impinge on the surface. Some of hydrocarbon species colliding with

Reproduced with permission of the copyright owner. Further reproduction prohibited without permission.

the surface are adsorbed, while adsorbed hydrocarbon species may desorb back into the gas phase. On the surface, adsorbed carbon atoms diffuse along the surface or into the bulk SiC intermediate layer. Diamond nucleation occurs on the upper surface of the intermediate layer due to the surface diffusion of adsorbed carbon atoms and reactions leading to cluster growth. The bulk diffusion of adsorbed carbon atoms leads to the formation and subsequent growth of the SiC intermediate layer, and that layer growth is terminated when the number of adsorbed carbon atoms is saturated to the extent that diamond nuclei form and grow at the expense of intermediate layer formation.

The formation of polycrystalline SiC films by Si out-diffusion from the Si substrate has been also observed by a number of investigators [34,48-60] during SiC carbonization processes. Without introducing Si-bearing precursors to the system, SiC films were deposited on Si substrates using a variety of hydrocarbon species, including CH_4 and C_3H_8, diluted with H_2. The polycrystalline SiC film formed by Si out-diffusion is distinguished from the SiC intermediate layer formed during diamond deposition by its surface roughenss, layer thickness, and void formation. With increasing substrate temperature and decreasing inlet hydrocarbon concentration, the SiC film usually has larger saturated thickness, up to hundreds of nanometers, and rougher surface morphology than those of the intermediate layer in a diamond CVD system. Further, the out-diffusion of Si atoms results in the formation of inverted pyramid-like voids in the Si substrate during carbonization. These observations suggest that the polycrystalline SiC film is formed by out-diffusion of Si atoms from the Si substrate and further reaction of Si atoms with hydrocarbon species on the growth surface. The SiC film growth continues until Si atoms

Reproduced with permission of the copyright owner. Further reproduction prohibited without permission.

can no longer diffuse to the surface through the SiC film at rates that sustain the film growth, and the thickness of the film then asymptotes to a saturated value.

However, the presence of polycrystalline SiC films formed by Si out-diffusion is generally observed at higher substrate temperatures than those present during SiC intermediate layer growth in diamond CVD. Experimental results indicate that substrate temperatures between 1273 and 1683 K are generally required to grow polycrystalline SiC films by Si out-diffusion. The upper limit on the substrate temperature, 1683 K, is the melting temperature of the Si substrate [61]. Sun et al [34] conducted an experimental study comparing substrate temperatures for the growth of SiC intermediate layers by C bulk diffusion and polycrystalline SiC films by Si out-diffusion. They observed diamond deposition on very thin SiC intermediate layers at substrate temperatures between 973 and 1273 K. No thin SiC intermediate layer, however, was observed at higher substrate temperatures between 1273 and 1473 K. Instead, only polycrystalline SiC films were grown without further diamond deposition on the SiC films during less than 1 h deposition time. A possible explanation would be that, although the Si out-diffusion is significant if the substrate temperature is relatively high, it is a secondary effect under diamond nucleation conditions. Therefore, although the SiC layer could form either by the bulk diffusion of adsorbed carbon atoms or the Si out-diffusion from the Si substrate, the Si out-diffusion is negligible at deposition temperatures typical of diamond nucleation in HFCVD reactors.

Accordingly, it appears that when a SiC intermediate layer develops at the interface between a diamond film and a Si substrate, it is due to the bulk diffusion of carbon atoms through the intermediate layer toward the Si substrate surface under the operating

Reproduced with permission of the copyright owner. Further reproduction prohibited without permission.

conditions conductive to diamond nucleation. Therefore, a model of the time evolution of the intermediate layer requires knowledge of the amount of adsorbed carbon atoms available for intermediate layer formation. This quantity may be calculated through the consideration of both kinetics of diamond nucleation and intermediate layer formation.

Extensive experimental investigations [14-41] have revealed the existence of SiC intermediate layers on Si substrates during diamond CVD; however, theoretical modeling studies of intermediate layer formation are scarce, and the kinetics are not completely understood. Attempts to describe the kinetic aspects of diamond nucleation processes have resulted in the development of models predicting time evolution of the density and rate of diamond nucleation in CVD processes [62-66]. The models captured the critical features associated with diamond nucleation: impingement, adsorption and desorption, surface diffusion, and diamond nucleation. Liu and Dandy [67] developed a theoretical model to capture important physical aspects of diamond nucleation on carbide-forming substrates during the incubation period and the transient nucleation stage in CVD processes. Their model predicted the time evolution of the surface concentration of carbon atoms, as well as the effects of substrate materials such as Si, Ta, W, Mo, Fe, and Ti, surface diffusion, and adsorption state on the diamond nucleation.

Existing diamond nucleation models [62-67] can be applied to investigate the formation of the β-SiC intermediate layer in diamond CVD by using the appropriate kinetic mechanism–one that includes impingement, adsorption and desorption, surface diffusion, and diamond nucleation–associated with diamond nucleation. These models, however, are limited in their ability to reproduce reported experimental observations of intermediate layer formation. These models have been limited by resolving (*i*) interaction

Reproduced with permission of the copyright owner. Further reproduction prohibited without permission.

mechanisms of predominant hydrocarbon species with the surface of the intermediate layer; (*ii*) adsorption energies and bulk diffusion energies; (*iii*) the bulk diffusion mechanism of adsorbed carbon atoms into the intermediate layer; (*iv*) the mechanism for intermediate layer formation; (*v*) effects of deposition parameters on intermediate layer formation; and (*vi*) influences of the structure of the intermediate layer on diamond nucleation.

The present study constitutes a theoretical examination of important aspects of the formation of the β-SiC intermediate layer between diamond films and Si substrates during nucleation and the early stages of diamond deposition. The purpose of this study is to (*i*) predict the time evolution of a β-SiC intermediate layer under the operating conditions conductive to diamond nucleation via HFCVD; (*ii*) determine the dependence of the time evolution of the layer on operating parameters such as substrate temperature and inlet gas composition; (*iii*) compare the time scales associated with intermediate layer growth and diamond nuclei growth; (*iv*) examine discrepancies in published adsorption energies of gaseous hydrocarbon precursors on the β-SiC (100) surface and then determine the most reasonable value of the adsorption energy consistent with published experimental data for intermediate layer thickness; and (*v*) discern, quantitatively, the operating conditions that lead to intermediate layer growth followed by diamond deposition versus those that yield heteroepitaxial diamond nucleation without intermediate layer formation.

In the current study, a model is developed to investigate the formation of the β-SiC intermediate layer during nucleation and the early stages of diamond deposition in HFCVD reactors. The model is based on an existing diamond nucleation model dealing with problems related to impingement, adsorption and desorption, surface diffusion, and

Reproduced with permission of the copyright owner. Further reproduction prohibited without permission.

diamond nucleation. The existing model is modified here to capture mechanisms for both intermediate layer formation and diamond nucleation on the intermediate layer through the introduction of additional kinetic information such as adsorption energies and sticking coefficients of gaseous hydrocarbon species on the β-SiC (100) surface, bulk diffusion energies and mechanisms of adsorbed carbon atoms through defects of the intermediate layer, and time-dependent growth mechanisms of the intermediate layer and the diamond nucleus.

3.2 Model Description

A kinetic mechanism—including gas-phase and surface reactions, impingement, adsorption and desorption, surface and bulk diffusions, diamond nucleation, and β-SiC intermediate layer formation—is built on an existing diamond nucleation model with detailed information of adsorption energies, bulk diffusion energies, and sticking co-efficients. In particular, the near-surface concentrations of gaseous hydrocarbon species are determined under the operating conditions conductive to diamond nucleation in HFCVD reactors. The predominant hydrocarbon species impinge on the surface, and the adsorption rates of these species are determined by the impingement rates and the sticking coefficients of the species on the deposition surface. Desorption of adsorbed hydrocarbon species then occur with a desorption rate determined by a representative residence time. Hydrogen is sequentially removed from adsorbed hydrocarbon species, and adsorbed species dissociate to carbon atoms before these atoms diffuse along the surface or into the intermediate layer. In the present model, β-SiC (100) is assumed to be

Reproduced with permission of the copyright owner. Further reproduction prohibited without permission.

the intermediate layer, and the surface radical sites of the intermediate layer are considered for surface reactions.

The bulk diffusion of adsorbed carbon atoms through the SiC layer leads to continued intermediate layer growth. Initially the surface is (100) silicon, and after the adsorbed carbon reacts with the surface to form β-SiC. The adsorbed carbon atoms diffuse to reach the interface between the intermediate layer and the Si substrate, and react with Si to form β-SiC. Intermediate layer growth effectively ceases when the surface density of adsorbed carbon atoms is saturated to the extent that diamond nuclei form and grow at the expense of intermediate layer formation. In the current model it is assumed that reactions at the interface between the SiC intermediate layer and the Si substrate are rapid relative to the bulk diffusion rate of adsorbed carbon atoms. The Damköhler number is estimated at the reaction rate coefficient and the bulk diffusion coefficient, and it is found to be 10^{14} to10^{21}, depending on substrate temperature in the range of 973 to 1273 K. Under this circumstance the formation of the β-SiC intermediate layer is controlled by the bulk diffusion rate.

The large lattice mismatch at the interface (≈ 22%) between the β-SiC intermediate layer and the Si substrate promotes dislocations, and the spacing between dislocations is the order of only few lattice constants. As the β-SiC intermediate layer grows, defects develop through the intermediate layer due to the high density of interface dislocations. Of the various defect types, grain-boundary defects and lattice vacancy defects are expected to be the primary routes for the diffusion of carbon atoms into the bulk β-SiC intermediate layer [68]. The predicted diffusion rates of carbon atoms through these two types of defects are then compared to identify the dominant bulk diffusion route.

Reproduced with permission of the copyright owner. Further reproduction prohibited without permission.

The surface diffusion of adsorbed carbon atoms leads to the formation and subsequent growth of diamond nuclei on the upper surface of the evolving β-SiC intermediate layer. During the initial stages of diamond nucleation, the nuclei may either grow or shrink depending on kinetic and thermodynamic conditions. When the number of carbon atoms present in the diamond nucleus exceeds a certain critical number i, the nucleus is considered to be stable and will continue to grow. A diamond nucleus containing i carbon atoms is referred to as the critical nucleus, and all larger nuclei containing at least $i + 1$ carbon atoms are referred to as the stable nuclei. The growth of nuclei is the result of the surface diffusion of adsorbed carbon atoms. The surface density of stable nuclei increases with time and eventually reaches a saturated value. The saturated surface density of stable nuclei may be determined by calculating the depletion of adsorbed carbon atoms due to the growth of nuclei existing within the area equal to the square of the average surface diffusion length. With further growth after the saturation value, the stable nucleus size grows continuously without further changes in the surface density of stable nuclei, and later the surface density decreases due to the coalescence between nuclei. A continuous diamond film is formed on the upper surface of the β-SiC intermediate layer when isolated nuclei grow continuously and eventually coalesce.

A model is developed to predict β-SiC intermediate layer formation and transition to diamond nucleation. In the present study, it is not necessary to model the system up to the point of nuclei coalescence because intermediate layer growth rate is negligible long before diamond nuclei coalescence. Because of this the early stages of diamond deposition—until growing diamond nanocrystallites cover a small surface area, up to 1% of the overall surface area of the β-SiC intermediate layer—is considered. When growing

Reproduced with permission of the copyright owner. Further reproduction prohibited without permission.

diamond nuclei cover less than 1% of the surface area of the intermediate layer, it is not unreasonable to assume that the growth of diamond nuclei is in its earliest stages. The β-SiC is considered as the surface material in the present model, and thus the model provides a quantitative estimate of the surface adsorption occurring only after a continuous β-SiC layer forms on the Si substrate surface. The surface detachment of diamond clusters containing more than one atom is not taken into account, since desorption energies of these clusters are expected to be much larger than adsorbed carbon atoms. Further, the clusters containing more than one carbon atom are not considered to be mobile [69], and therefore only carbon atoms are assumed to diffuse along the surface to form diamond nuclei.

A set of rate equations describing the kinetic behavior of adsorbed carbon atoms and diamond nuclei, can predict the time evolution of the surface densities of carbon atoms and diamond nuclei on the surface. The time evolution of the surface density of adsorbed carbon atoms is determined by the adsorption rates of gaseous hydrocarbon species, the desorption rates of adsorbed hydrocarbon species, the capture rates of adsorbed carbon atoms by stable nuclei and critical nuclei, and the bulk diffusion rates of carbon atoms into the β-SiC intermediate layer, and is expressed as

$$\frac{dn_1}{dt} = R_a - \frac{n_1(t)}{\tau_s} - \sigma_x D_s n_1(t) n_x(t) - (i+1)\sigma_i D_s n_1(t) n_i(t) - R_d\,, \qquad (1)$$

where n_1 is the surface density of adsorbed carbon atoms, R_a is the overall adsorption rate of carbon atoms from CH_3 and C_2H_2, τ_s is the residence time of adsorbed hydrocarbon species, D_s is the surface diffusion coefficient of adsorbed carbon atoms, i is the size of critical nuclei, n_i and n_x are the surface number densities of critical and stable nuclei, R_d is

Reproduced with permission of the copyright owner. Further reproduction prohibited without permission.

the bulk diffusion rate of carbon atoms into the SiC intermediate layer, and σ_i and σ_x, which describe surface diffusion flows of adsorbed carbon atoms to critical and stable nuclei, are the capture numbers and the values are chosen at 4 and 5, respectively [67]. The time evolution of the surface density of stable nuclei is given by

$$\frac{dn_x}{dt} = \sigma_i D_s n_1(t) n_i(t) . \quad (2)$$

The surface density of critical nuclei depends on the number of atoms present in each seed and can be expressed as

$$n_i = \frac{1}{2} n_1 (x - i) \quad x > i$$

$$\text{and } n_i = 0 \qquad 1 < x \leq i . \quad (3)$$

The critical nucleus size, i, has been predicted to be between 5 and 8 carbon atoms [70]. However, in that study the desorption of diamond clusters was not considered, so the actual critical nucleus size is expected to be slightly larger than the predicted range; therefore, it is assumed in this study that a critical nucleus contains 10 carbon atoms. Not coincidentally, this is also the number of carbon atoms in the diamond structure of the boat-boat conformer of bicyclodecane. As such, the critical nucleus size is chosen to be 10 carbon atoms, and all larger nuclei containing more than 10 carbon atoms are considered to be stable. The average stable nucleus size depends on the surface density of adsorbed carbon atoms,

$$x = \sigma_i D_s \int_0^t n_1(t) dt . \quad (4)$$

The overall adsorption rate of carbon atoms, R_a, is determined by accounting for the impingement rates, R_{imp}, and the sticking coefficients, ν, of the predominant gaseous

Reproduced with permission of the copyright owner. Further reproduction prohibited without permission.

hydrocarbon species, assumed to be CH_3 and C_2H_2 for the operating conditions used in this study, with the surface radical sites, such that

$$R_a = R_{imp}\nu . \tag{5}$$

The impingement rate, R_{imp}, represents the number of carbon atoms present in the predominant hydrocarbon species colliding with the surface per unit time and area and is given by [67,71]

$$R_{imp} = j\frac{N_A P}{\sqrt{2\pi MRT}} = 3.513\times10^{22}\, j\frac{P}{\sqrt{MT}}, \tag{6}$$

where j is the number of carbon atoms present in the predominant hydrocarbon species, either 1 or 2 in the calculations, N_A is Avogadro's number, P (torr) is the near-surface partial pressure of the hydrocarbon species, M is the molecular weight of the hydrocarbon species, R is the universal gas constant, and T (K) is the gas temperature at the surface, assumed to be same as the substrate temperature.

For a particular set of operating conditions, the near-surface partial pressures of the gaseous hydrocarbon species are computed through numerical solution of the differential equations describing flow, heat, and mass transfer in a pedestal reactor geometry. A stagnation flow program [72], together with Fortran packages called Chemkin-III [73] and Surface Chemkin [74] for analysis of gas-phase and surface chemical kinetics, is used to predict the near-surface composition. Multicomponent transport properties for the gas phase are calculated using a Fortran computer program [75]. The reversible gas-phase reactions used in the present study are based on an established pyrolysis mechanism [76]. The surface reactions in the model incorporate the roles of atomic hydrogen on the activation and termination of the surface radical sites. It is assumed that the rate coefficients of the activation and termination reactions on a carbon-terminated surface are

Reproduced with permission of the copyright owner. Further reproduction prohibited without permission.

applicable to a SiC surface. Since atomic hydrogen is extremely reactive it is expected that this assumption is reasonable, even though the surfaces are not chemically identical. The rate coefficients are predicted by Battaile et al. [77] for diamond deposition and shown in Table 3.1.

Table 3.1 Simplified surface reaction mechanism for atomic hydrogen adsorption and abstraction on Si surface radical sites[a].

Reaction	A	β	E
$SiH(S) + H \leftrightarrow Si(S) + H_2$	1.3×10^{14}	0.0	7300.0
$Si(S) + H \leftrightarrow SiH(S)$	1.0×10^{13}	0.0	0.0

[a] Arrhenius parameters in form $k_i = AT^{\beta}\exp(-E/RT)$ in units (A in moles, cubic centimeters, and seconds; E in calories per mole). The surface radical site is represented by (S).

The sticking coefficient, ν, is defined as a probability of a certain reaction process when a given collision occurs. Calculations of the gas-phase composition in the stagnation flow geometry indicate that the near-surface gas-phase concentrations of CH_3 and C_2H_2 are significantly higher than other hydrocarbon species; therefore, these are the only two hydrocarbon species considered as film growth precursors. At T_s = 1200 K the sticking coefficients for CH_3 and C_2H_2 are 0.24 [77] and 0.02 [78]. Since no data is available for reactions of gaseous CH_3 and C_2H_2 species with the surface radical sites of β-SiC, the sticking coefficient for CH_3 is based on the reaction of this species with carbon surface sites, and the sticking coefficient for C_2H_2 is taken from a study of C_2H_2 adsorption on silicon surfaces.

The desorption rate of hydrocarbon species is accounted for using the average residence time of each species. The residence time, τ_s, is a measure of how long, on average,

Reproduced with permission of the copyright owner. Further reproduction prohibited without permission.

an adsorbed hydrocarbon species remain on the surface before desorbing back into the gas phase. This quantity may be calculated as [67,71]

$$\tau_s = \frac{1}{\nu_a}\exp\left(\frac{E_a}{kT_s}\right), \qquad (7)$$

where ν_a is the effective surface vibrational frequency of adsorbed species (assumed to be 10^{13} s^{-1} in this study [67]), E_a is the adsorption energy, k is Boltzmann's constant, and T_s is the substrate temperature. Since there is uncertainty regarding the actual value of the adsorption energies of CH_3 and C_2H_2 on the β-SiC (100) surface, a range of adsorption energies are selected from the literature for the Si (100) surface [79,80] and the Si-surface of β-SiC (100) [81], as shown in Table 3.2. These values are tested in the model to deter-

Table 3.2 Adsorption energies and surface residence times of CH_3 and C_2H_2 for Si (100) and β-SiC (100) surfaces.

Adsorbed species	E_a (eV/atom)[a]	τ_s (s)[b]
CH_3	1.43[78]	9.91×10^{-8}
	2.86[79]	1.03×10^{-1}
	3.29[80]	6.58×10^{0}
C_2H_2	1.73[78]	1.80×10^{-6}
	3.45[79]	3.09×10^{1}
	4.61[80]	2.30×10^{6}

[a] The adsorption energy is assumed to be the same as the desorption energy.
[b] The surface residence time is calculated for a substrate temperature of 1200K.

mine the most reasonable value of E_a that is consistent with reported experimental measurements for intermediate layer formation. For T_s = 1200 K, the residence times determined from the adsorption energies range from 9.9×10^{-8} s for E_a = 1.43 eV to 2.3×10^{6} s for E_a = 4.61 eV, as shown in Table 3.2. Although the actual residence time

Reproduced with permission of the copyright owner. Further reproduction prohibited without permission.

may range from below 1 ns to several hours, depending on the adsorption state, adsorption energy, and substrate temperature [67], the predicted value of τ_s corresponding to $E_a = 4.61$ eV is orders of magnitude above what is accepted as realistic in diamond CVD. However, by considering adsorption energies in the range $1.43 \leq E_a \leq 4.61$ eV and using the present model to calculate the saturated surface density of stable diamond nuclei and the final thickness of the β-SiC intermediate layer, it will be possible to identify the most probable value for E_a.

An adsorbed carbon atom will not necessarily remain on its initial surface site, but may diffuse along the surface or into the bulk of the intermediate layer. The surface diffusion coefficient D_s is given by [67,71]

$$D_s = \frac{\alpha \nu_d}{N_0} \exp\left(-\frac{E_s}{kT_s}\right), \tag{8}$$

where α is a constant and assumed to be ¼ for two-dimensional diffusion [82], ν_d is the effective vibrational frequency for the surface diffusion of adsorbed carbon atoms and is assumed to be equal to ν_a, $N_0 = 1.05 \times 10^{15}$ cm^{-2} is the total surface site density of β-SiC, and E_s is the activation energy for the surface diffusion of adsorbed carbon atoms. The value of E_s is predicted to be between one-sixth and one-half of E_a [83,84]; in the current study the value of $E_a/2$ is used.

Adsorbed carbon atoms diffuse along the surface during their residence time before desorbing. The average surface diffusion length, λ, of adsorbed carbon atoms is given by [71]

$$\lambda = \sqrt{2D_s\tau_s} = \sqrt{\frac{a^2}{4}\exp\left(\frac{E_a}{2kT_s}\right)}, \tag{9}$$

Reproduced with permission of the copyright owner. Further reproduction prohibited without permission.

where the lattice constant of β-SiC is a = 4.36×10^{-8} cm. Using this result the saturated surface density of stable nuclei, N_s, is determined by [85]

$$N_s = \frac{N_0 a^2}{\lambda^2} = 4N_0 \exp\left(-\frac{E_a}{2kT_s}\right), \tag{10}$$

where the reactive site density, N_0, is $2/a^2$ for a face centered cubic (fcc) lattice structure.

The bulk diffusion of adsorbed carbon atoms occurs through defects such as grain boundaries and lattice vacancies and is expected to be the primary route for the formation and subsequent growth of the β-SiC intermediate layer [68]. The diffusion coefficients associated with grain boundary and lattice vacancy transport are expressed as [68]

$$\begin{aligned} D_g &= 4.44\times10^7 \exp\left(-\frac{5.84}{kT_s}\right), \\ D_v &= 2.62\times10^8 \exp\left(-\frac{8.72}{kT_s}\right) \end{aligned} \tag{11}$$

respectively, where the activation energies in the exponents are eV/atom. The pre-exponential constant and activation energy parameters in the expressions in Eq. (11) contain significant uncertainties, roughly 60%. However, the range of bulk diffusion coefficient values resulting from these uncertainties are not considered in the present study; there are no clear data indicating that the expressions in Eq. (11) should be used to obtain more than an order of magnitude estimate for bulk diffusion coefficients. Further, the activation energy for grain boundary diffusion is less than two-third of the corresponding value for lattice vacancy diffusion, and as a result the diffusion coefficient for grain boundary transport is predicted to be eleven orders of magnitude greater than that for lattice vacancy at T_s = 1200 K. Consequently, grain-boundary diffusion is assumed to be the only diffusion mechanism for bulk transport of carbon atoms in the SiC intermediate layer.

Reproduced with permission of the copyright owner. Further reproduction prohibited without permission.

Assuming that the grain boundaries are oriented perpendicularly to the surface and that these boundaries are uniformly distributed throughout the bulk phase of the intermediate layer, the bulk diffusion coefficient, D_b, can be approximated as

$$D_b \approx D_g \frac{\delta_b}{l}, \quad (12)$$

where δ_b is the average width of grain boundaries, assumed to be 5 Å [86,87]. This value is also similar to the lattice constant of β-SiC (100), 4.36 Å. The average distance between individual grain boundaries, l, can be approximated as $l = d/f$, where $d \approx 3.08$ Å is the distance of nearest atoms on the β-SiC (100) face, and $f = 0.22$ represents the lattice mismatch between β-SiC and Si.

The bulk diffusion rate R_d of adsorbed carbon atoms into the β-SiC intermediate layer is predicted using Fick's first law of diffusion, assuming the bulk diffusion through a semi-infinite slab [88]:

$$R_d = C_s \sqrt{\frac{D_b}{\pi \cdot t}}, \quad (13)$$

where C_s (atom/cm^3) is the volume concentration of adsorbed carbon atoms in the bulk near the gas-solid interface and is given by $C_s = n_1/a_c$ [67], where $a_c = 1.54$ Å is the diameter of a carbon atom.

Given that the total number of carbon atoms diffusing into the β-SiC intermediate layer in time t is given by

$$M_t = \int_0^t R_d \, dt, \quad (14)$$

the β-SiC intermediate layer thickness, L, at any time t can be calculated as

Reproduced with permission of the copyright owner. Further reproduction prohibited without permission.

$$L = \frac{M_t}{C^*} = \frac{2 \cdot n_{1,s}}{a_C \cdot C^*} \sqrt{\frac{D_b \cdot t}{\pi}}, \quad (15)$$

where $C^* = 4.83\times10^{22}$ C atom/cm^2 is the surface density of carbon atoms necessary to form a stoichiometric β-SiC intermediate layer and $n_{1,s}$ is the surface density of adsorbed carbon atoms chosen at the saturation value of the surface density of stable nuclei, $n_1 = n_{1,s}$ and $n_x = N_s$ at $t = t_s$. When the surface diffusion length is of the same order of magnitude as the average distance between clusters and is decreased as the cluster size increases, the surface density of adsorbed carbon atoms is monotonously decreased as the cluster size increases after $t = t_s$ until nuclei coalesce. Nevertheless, since the nucleation regime terminates well before the onset of coalescence, and the stable nuclei are occupied very small portion of the surface during the nucleation, the dependence of the surface diffusion length on the cluster size increase is so small that n_1 is not appreciably changed during the nucleation and the intermediate layer growth concerned in this study.

There is evidence in support of the supposition that the intermediate layer growth effectively ceases during the early stages of diamond deposition [14,17,20,34]. To confi-rm that this hypothesis is reasonable, calculations are performed under different conditions to compare the time scales associated with intermediate layer growth and diamond nuclei growth. The time scale for diamond nuclei growth is represented by the time evolution of the surface area, S, covered by growing diamond nuclei. The van der Drift model [89,90] is applied to predict the S value. The time evolution of S is determined from the lateral growth velocity of diamond nuclei, V_l, the average distance between individual diamond nucleus, d_0, and the saturated surface density of stable nuclei. A value for V_l is calculated from a model based on the growth rate parameter, α_{3D}

Reproduced with permission of the copyright owner. Further reproduction prohibited without permission.

= $\sqrt{3}\, V_{100}/V_{111}$, where V_{100} and V_{111} are the growth velocities of the {100} and {111} faces on a diamond nucleus. In typical diamond CVD processes two crystal faces, {111} and {100}, are commonly observed, whereas the fastest growing {110} face is not as prevalent. Thus, the nuclei evolution model can be simplified to the growth of two-dimensional nuclei, where the appropriate growth rate parameter, α_{2D}, is related to the ratio of the growth velocities of the {10} and {11} faces on a diamond seed. The two-dimensional parameter is defined as $\alpha_{2D} = \sqrt{2}\, V_{10}/V_{11}$, where V_{10} and V_{11} are the growth velocities of the {10} and {11} faces [91]. Once V_{11} is calculated from known values of α_{2D} and V_{10} corresponding to specific growth conditions, the average growth velocity onto the lateral surface, V_l, is determined to be a same magnitude of V_{10}. Choosing the operating parameters such as T_s = 1200 K and the inlet mole fraction of CH_4 in H_2 X_{CH_4} = 0.02, the values of the growth velocity of the {10} face, V_{10}, [77] and the two-dimensional growth parameter, α_{2D}, [90] are adopted from the literature. The average distance between individual diamond nucleus, d_0, is calculated from the saturated surface density of stable nuclei N_s.

3.3 Results and Discussion

For the calculations carried out in this study, the operating conditions typical of diamond nucleation in HFCVD reactors are chosen as follows: reactor pressure P = 50 torr, inlet gas flow rate U_∞ = 300 sccm, distance from the substrate surface to the filament D = 0.5 cm, and filament temperature T_f = 2500 K. Calculations are performed for

Reproduced with permission of the copyright owner. Further reproduction prohibited without permission.

two different substrate temperatures, T_s = 1000 and 1200 K. The operating conditions used in the present calculations are summarized in Table 3.3. Calculations are also perfo-

Table 3.3 Operating conditions used in the present calculations.

Total gas pressure		50 torr	
Inlet gas velocity		1.0 cm/s	
Filament temperature		2500 K	
Distance from substrate surface to filament		0.5 cm	
Substrate temperature		1000, 1200K	
Inlet mole fraction	CH_4	H_2	H
	0.005	0.906	0.089
	0.010	0.935	0.055
	0.020	0.949	0.031
	0.040	0.943	0.017

rmed for different inlet compositions by varying the inlet mole fraction of CH_4 in H_2, X_{CH_4}, from 0.005 to 0.04. To obtain an estimate of the degree of heterogeneous H_2 dissociation on the surface of the 2500 K filament, a linear filament poisoning model is applied [92].

The mole fractions of the predominant gaseous hydrocarbon species at the deposition surface and the overall adsorption rate of carbon atoms are evaluated for different substrate temperatures and inlet compositions, and listed in Table 3.4. The mole fractions are determined by computing the gas-phase velocity, temperature, and concentration profiles in an idealized stagnation flow geometry [92]. It is predicted that hydrocarbon species such as CH_3 and C_2H_2 are present at the surface in sufficiently large con

Reproduced with permission of the copyright owner. Further reproduction prohibited without permission.

centrations to be considered as the predominant precursor species. For example, when the near-surface concentrations of CH_3 and C_2H_2 are compared to the other CH_x and C_2H_y

Table 3.4 Calculated mole fractions of predominant gaseous hydrocarbon species at the deposition surface and overall absorption rate of carbon atoms.

Operating parameters	Mole fraction		Overall adsorption rate R_a
Substrate temperature	CH_3	C_2H_2	
1000K	1.34×10^{-3}	5.47×10^{-3}	6.34×10^{18} cm^{-2}
1200K	1.22×10^{-3}	4.64×10^{-3}	5.15×10^{18} cm^{-2}
Inlet mole fraction of CH_4	CH_3	C_2H_2	
0.005	8.61×10^{-4}	2.59×10^{-3}	3.37×10^{18} cm^{-2}
0.02	1.62×10^{-3}	6.63×10^{-3}	7.01×10^{18} cm^{-2}
0.04	1.92×10^{-3}	6.67×10^{-3}	7.86×10^{18} cm^{-2}

hydrocarbon species, the concentrations of these other species are always at least an order of magnitude lower than those of CH_3 and C_2H_2. Because of this observation, hydrocarbon species other than CH_3 and C_2H_2 are not considered as growth precursors in this study. Once the total impingement rate of carbon atoms is known from Eq. (6), the overall adsorption rate may be calculated using Eq. (5).

The saturated surface density of stable nuclei, N_s, is calculated for different substrate temperatures, T_s, and adsorption energies, E_a, using Eq. (10) as shown in Figure 3.1. Two substrate temperatures, 1000 and 1200 K, are chosen to quantitatively probe the sensitivity of N_s to this parameter. For a specific substrate temperature, N_s decreases extensively as E_a is increased from 1.43 to 4.61 eV. For example, for T_s = 1200 K, N_s is predicted to be 4.2×10^{12} cm^{-2} for E_a = 1.43 eV, but the nuclei density drops almost seven

Reproduced with permission of the copyright owner. Further reproduction prohibited without permission.

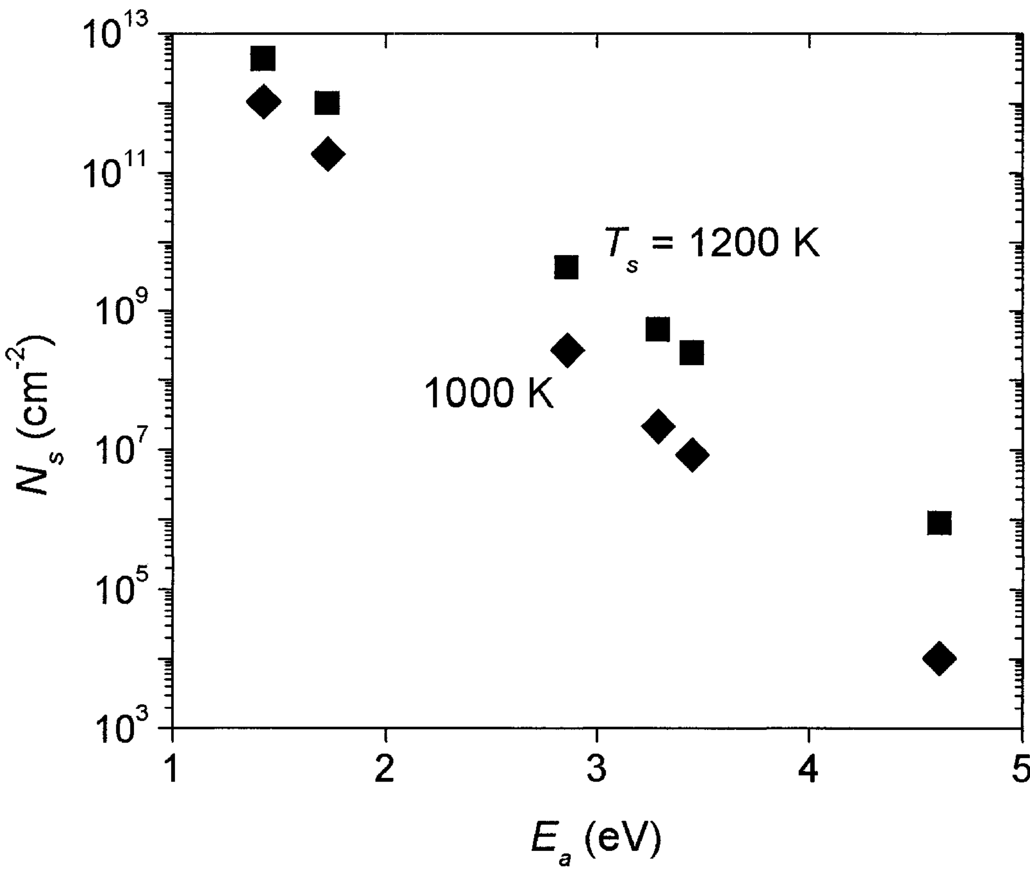

Figure 3.1 Saturated surface density of stable diamond nuclei, N_s, for different adsorption energies $E_a = 1.43$ to 4.61 eV and substrate temperatures $T_s = 1000$ and 1200 K.

Reproduced with permission of the copyright owner. Further reproduction prohibited without permission.

orders of magnitude, to 8.8×10^5 cm^{-2} when $E_a = 4.61$ eV. As the substrate temperature is decreased from 1200 to 1000 K, N_s also decreases because the surface diffusion rate of adsorbed carbon atoms is slower at the lower temperature. The saturated nucleation density of diamond obtained on untreated Si substrates is typically observed to be bellow ~10^6 cm^{-2} in diamond nucleation studies using HFCVD reactors [93]. For this upper bound of $N_s = 10^6$ cm^{-2}, the corresponding adsorption energy at 1200 K is calculated to be 4.6 eV by Eq. (10). However, it has also been observed in HFCVD experiments that the nucleation density of diamond monotonically increases with temperature until it reaches a maximum value at a substrate temperature of 1223 K, and then decreases with further increases in T_s [94]. The inverse relationship between nucleation density and temperature for $T_s > 1223$ K cannot be captured by the current model. In particular, the model is not applied to substrate temperatures above 1200 K because at these higher temperatures other carbon phases may appear, and the model is only applicable to describe the growth of the diamond phase.

Figure 3.2 shows the saturated surface density of adsorbed carbon atoms, $n_{1,s}$, and the time required to reach saturation, t_s, for different substrate temperatures and adsorption energies. Because of the uncertainty in the value of the adsorption energy, three different published adsorption energies for C_2H_2 are used in the calculations. For a specific adsorption energy, $n_{1,s}$ and t_s decrease extensively as T_s is increased from 1000 to 1200 K. At the higher substrate temperature, a larger surface diffusion rate, a larger saturated surface density of stable nuclei, and a shorter residence time are all predicted. The value of N_s is principally affected by the surface diffusion rate, and is expected to increase when the surface diffusion rate increases for a specific E_a. The value of $n_{1,s}$ incr-

Reproduced with permission of the copyright owner. Further reproduction prohibited without permission.

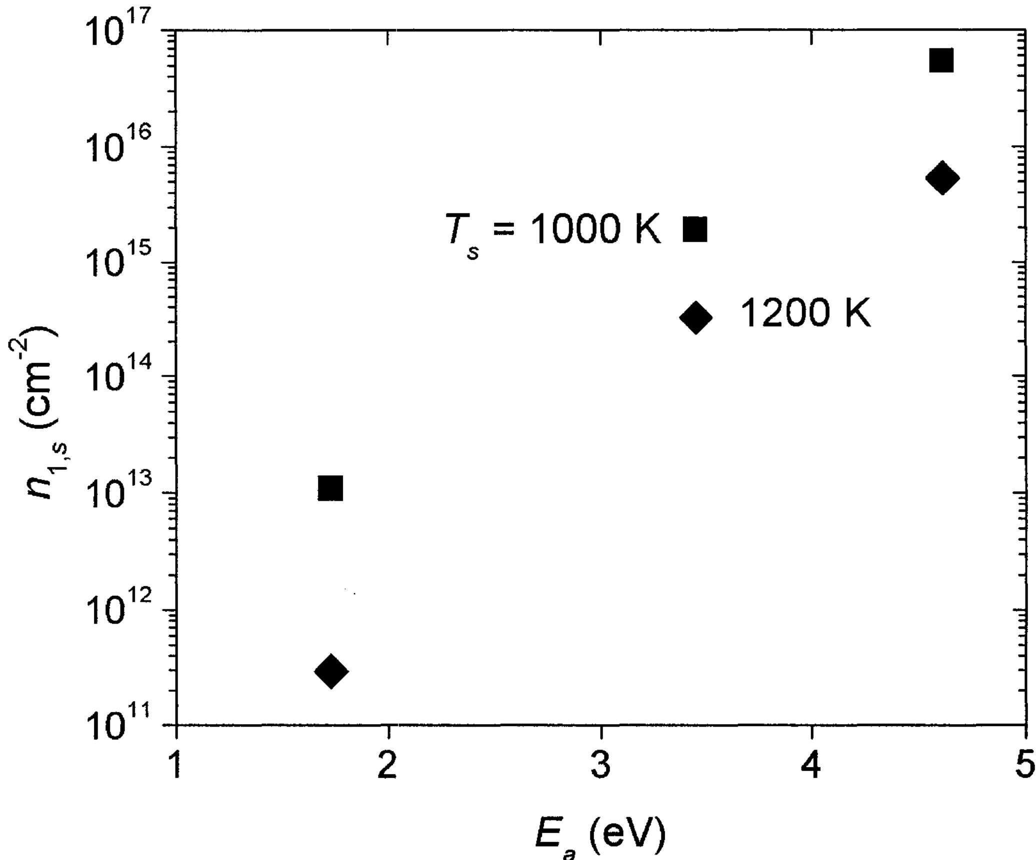

Figure 3.2a Saturated surface density of adsorbed carbon atoms, $n_{1,s}$, and time required to reach saturation, t_s, for different values of T_s, X_{CH_4}, and E_a. Figure shows $n_{1,s}$ vs. E_a for T_s = 1000 and 1200 K.

Reproduced with permission of the copyright owner. Further reproduction prohibited without permission.

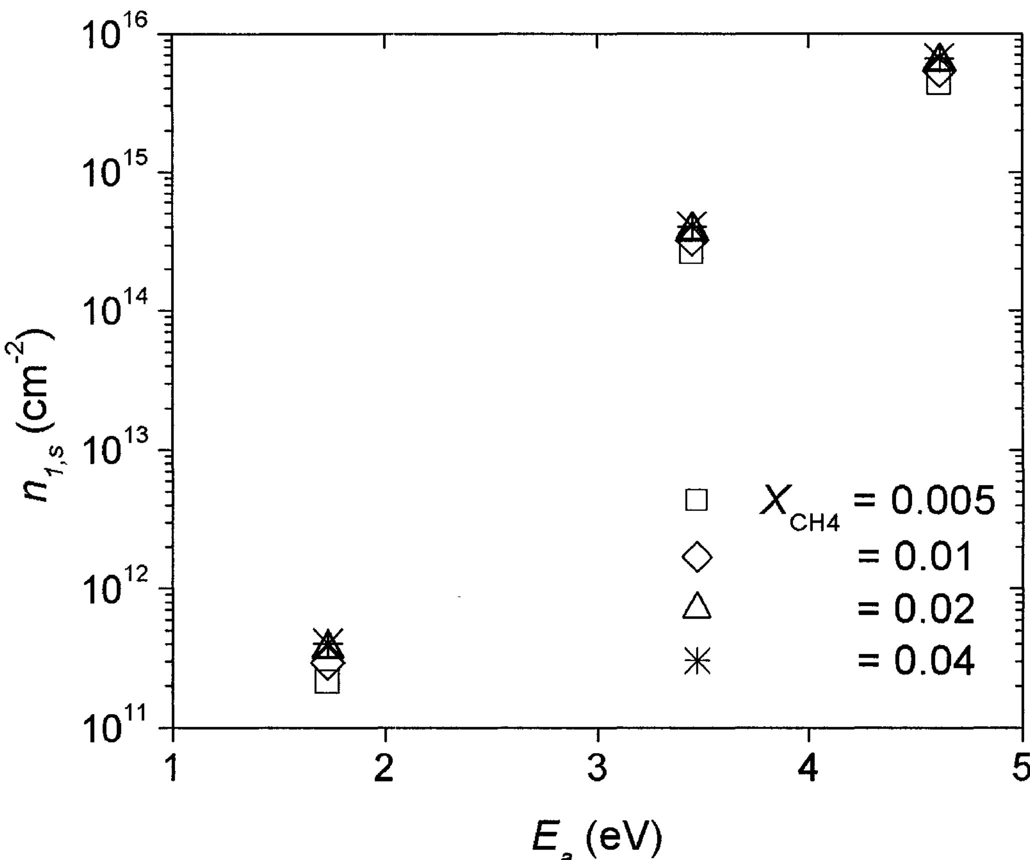

Figure 3.2b Saturated surface density of adsorbed carbon atoms, $n_{1,s}$, and time required to reach saturation, t_s, for different values of T_s, X_{CH_4}, and E_a. Figure shows $n_{1,s}$ vs. E_a for $X_{CH_4} = 0.005, 0.01, 0.02$, and 0.04.

Reproduced with permission of the copyright owner. Further reproduction prohibited without permission.

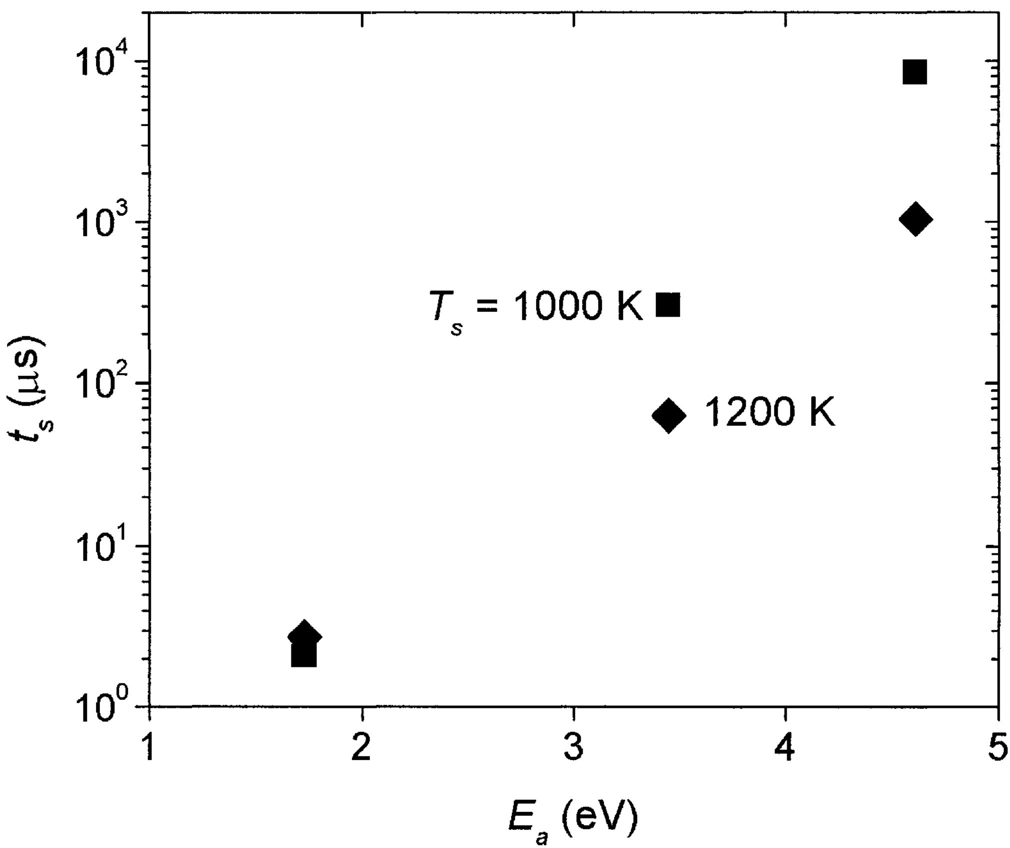

Figure 3.2c Saturated surface density of adsorbed carbon atoms, $n_{1,s}$, and time required to reach saturation, t_s, for different values of T_s, X_{CH_4}, and E_a. Figure shows t_s vs. E_a for T_s = 1000 and 1200 K.

Reproduced with permission of the copyright owner. Further reproduction prohibited without permission.

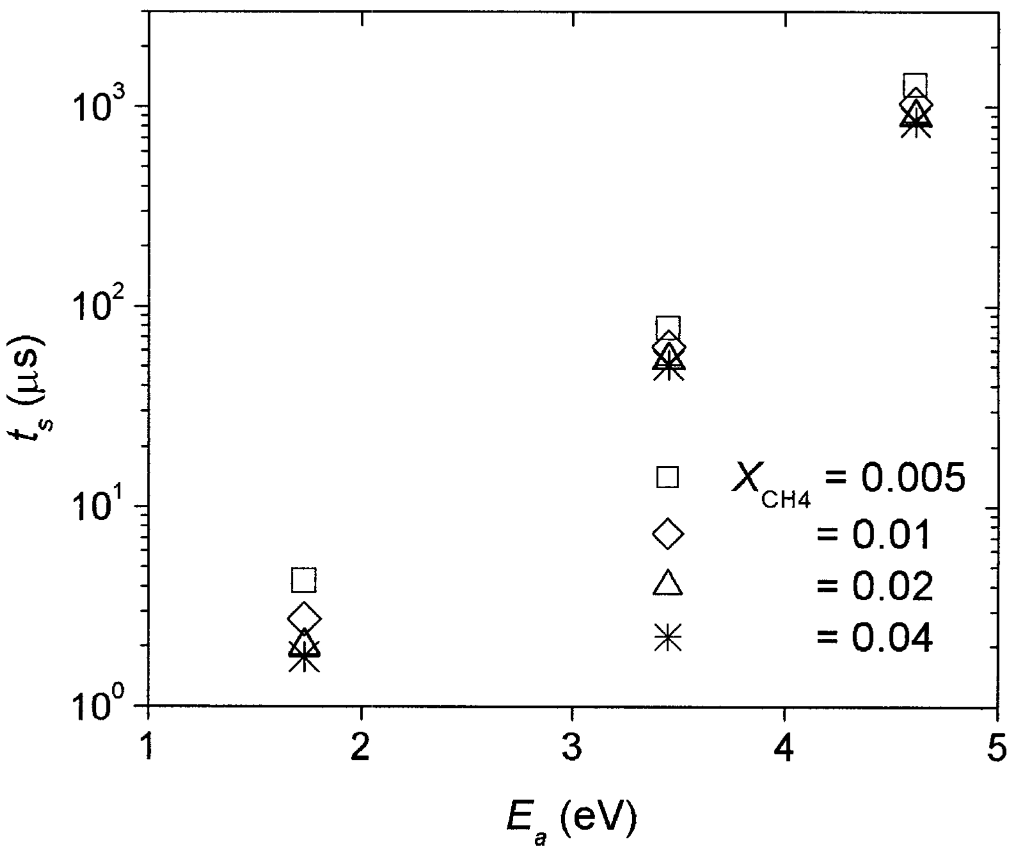

Figure 3.2d Saturated surface density of adsorbed carbon atoms, $n_{1,s}$, and time required to reach saturation, t_s, for different values of T_s, X_{CH_4}, and E_a. Figure shows t_s vs. E_a for X_{CH_4} = 0.005, 0.01, 0.02, and 0.04.

Reproduced with permission of the copyright owner. Further reproduction prohibited without permission.

eases with increasing E_a for constant operating conditions because longer residence times and lower surface diffusion rates are expected at larger E_a values, and these lead to larger $n_{1,s}$ values. The time required to reach saturation is very short (< 10^{-2} s) relative to the total growth time of the intermediate layer, and larger saturated surface density of stable nuclei leads to longer t_s. Further, the time depends on surface diffusion rate, residence time, saturated nucleation density, and operating conditions. However, the values of $n_{1,s}$ and t_s are not affected appreciably by changes in the inlet mole fraction of CH_4, as demonstrated in Figures 3.2c and 3.2d.

The time evolution of the intermediate layer thickness, L, is determined for the three different published E_a values for C_2H_2, as shown in Figure 3.3. The calculations indicate that a higher adsorption energy leads to a thicker intermediate layer due to a larger $n_{1,s}$ at the upper surface of the intermediate layer. For T_s = 1200 K and X_{CH_4} = 0.01, the intermediate layer reaches thickness of 10.5, 0.6, and 0.0006 nm for E_a = 4.61, 3.45, and 1.73 eV, respectively, during a 1h deposition time. There is evidence to support the hypothesis that the β-SiC intermediate layer thickness becomes saturated during nucleation and the early stages of diamond deposition [14,17,20,34]. Regarding the actual duration of intermediate layer growth, reported times vary from minutes to hours, and this wide range is attributed to implementation of different surface pretreatment methods and operating conditions. For example, Stoner et al. [20] measured the growth time of an intermediate layer in MW PACVD using x-ray photoelectron spectroscopy (XPS). The data indicated that the intermediate layer thickness saturated after 1 h, and did so before significant diamond nucleation could be detected. Belton et al. [17] also used XPS to monitor interlayer growth in a HFCVD reactor and they observed a continuous increase

Reproduced with permission of the copyright owner. Further reproduction prohibited without permission.

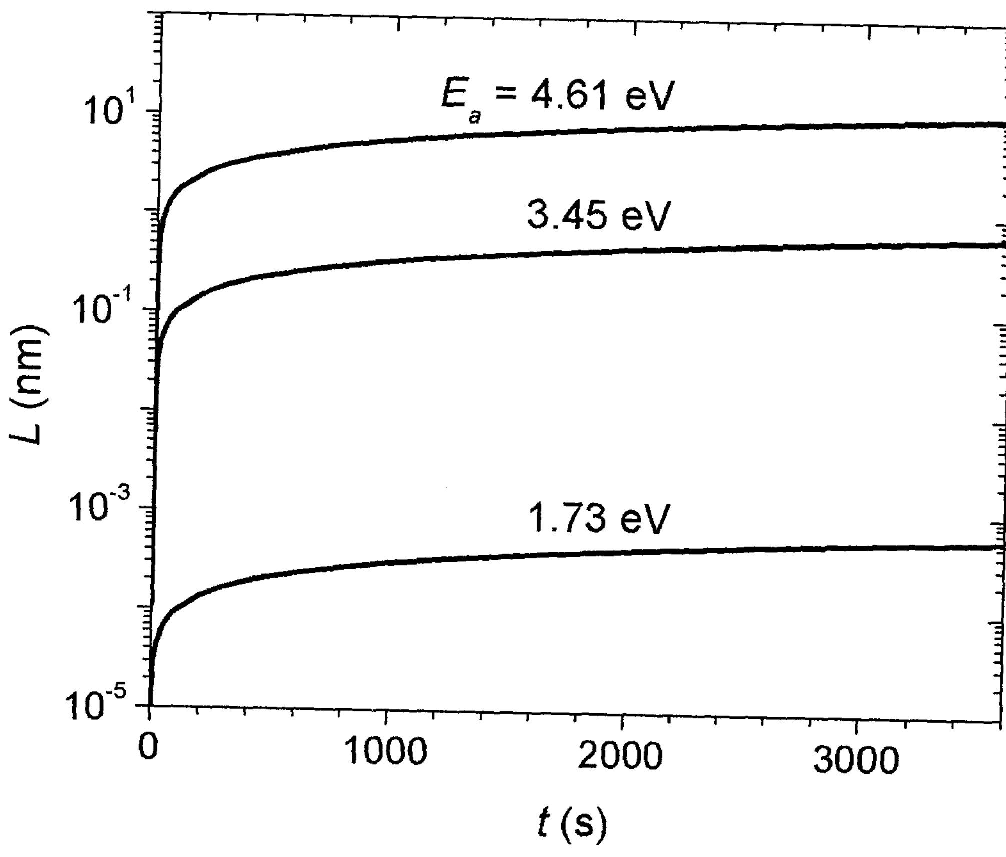

Figure 3.3 Time evolution of the intermediate layer for E_a = 1.73, 3.45, and 4.61eV during a 1 h deposition time. Operating conditions are T_s = 1200 K and $X_{CH_4} = 0.01$.

Reproduced with permission of the copyright owner. Further reproduction prohibited without permission.

in intermediate layer thickness for deposition times up to 4.5 h. However, Meilunas et al. [14] reported that the intermediate layer thickness reached 10 nm after 5 min, while diamond nanocrystallites were observed on the upper surface of the intermediate layer after 1 min. These disparate values for the saturation time of the intermediate layer thickness led to the choice of an intermediate value of 1 h in the present study. Based on the studies indicated above, a time of 1 h would appear reasonable for a bare silicon substrate with little or no pretreatment.

For E_a = 1.73 eV, the bulk diffusion rate of adsorbed carbon atoms is not sufficient to initiate the formation of a β-SiC monolayer during a 1 h deposition time. As E_a increases it is calculated that the thickness of the intermediate layer increases significantly. For E_a = 3.45 eV, however, the intermediate layer thickness is much larger than for E_a = 1.73 eV, and the thickness doesn't reach 1 nm during a 1 h deposition time. When E_a is further increased to 4.61 eV, the intermediate layer thickness is predicted to be 1 nm within 33 s, and reaches 10.5 nm during a simulated 1 h deposition time.

Figures 3.4 and 3.5 show the dependence of the time evolution of the intermediate layer on the substrate temperature and the inlet gas composition for two different E_a values, 3.45 and 4.61 eV. As may be inferred using Eq. (11), the intermediate layer thickness is strongly dependent on substrate temperature for both values of E_a due to a large increase in the bulk diffusion coefficient for carbon diffusion into the intermediate layer. When T_s increases from 1000 to 1200 K, the thickness increases 48 times for E_a = 3.54 eV and 28 times for E_a = 4.61 eV during a 1h deposition time. As X_{CH_4} is raised from 0.005 to 0.04 for a constant 1200 K substrate temperature, the thickness increases from 0.52 to 0.79 nm for E_a = 3.54 eV and from 8.53 to 13.03 nm for E_a = 4.61 eV for a 1 h

Reproduced with permission of the copyright owner. Further reproduction prohibited without permission.

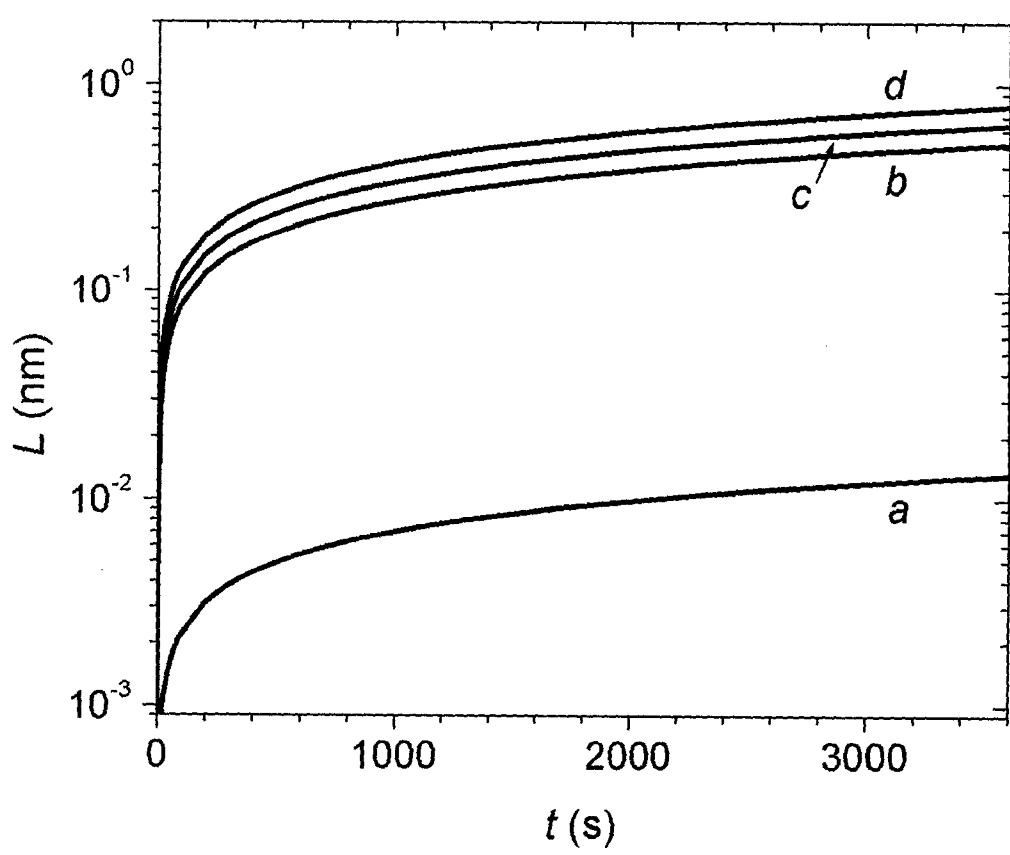

Figure 3.4 Dependence of the time evolution of the intermediate layer on T_s and X_{CH_4} for E_a = 3.45 eV during a 1 h deposition time. Operating conditions are (a) T_s = 1000 K and X_{CH_4} = 0.01, (b) T_s = 1200 K and X_{CH_4} = 0.005, (c) T_s = 1200 K and X_{CH_4} = 0.01, and (d) T_s = 1200 K and X_{CH_4} = 0.04.

Reproduced with permission of the copyright owner. Further reproduction prohibited without permission.

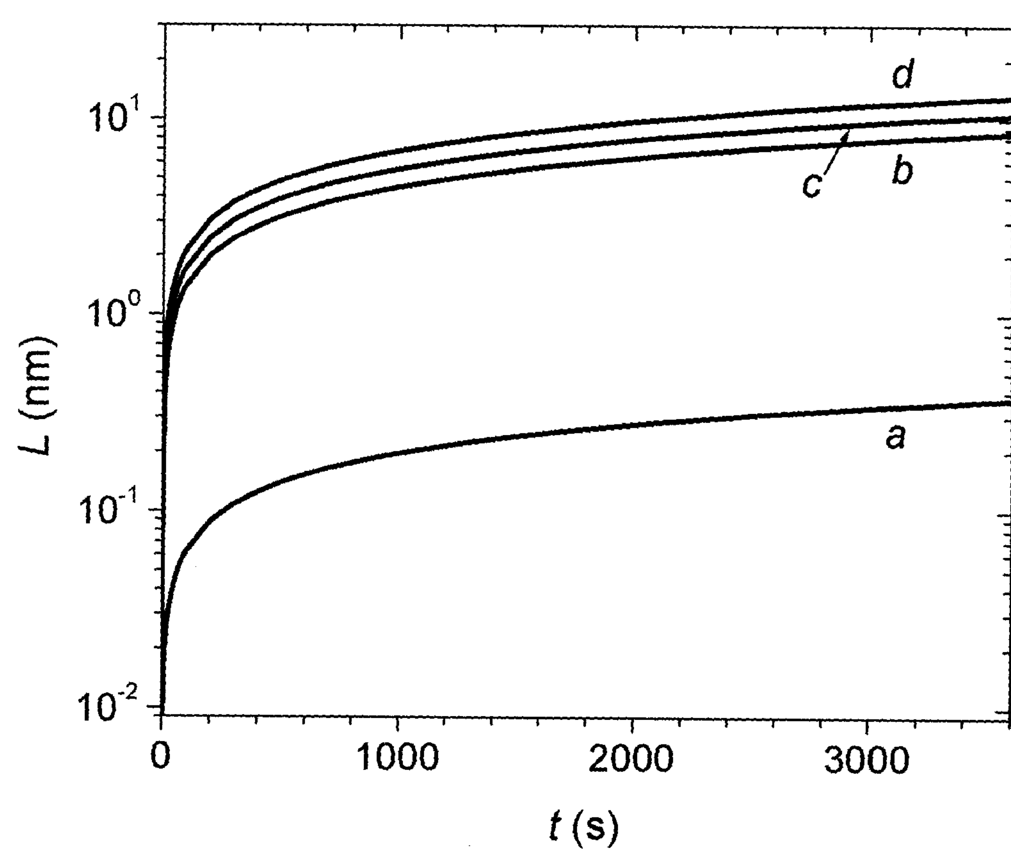

Figure 3.5 Dependence of the time evolution of the intermediate layer on T_s and X_{CH_4} for E_a = 4.61 eV during a 1 h deposition time corresponding to the operating conditions described in Figure 3.4.

Reproduced with permission of the copyright owner. Further reproduction prohibited without permission.

deposition time. Further, at the higher substrate temperature (1200 K) and inlet CH4 mole fractions (0.02 to 0.04) the intermediate layer thickness reaches 1 nm within 24 s for E_a =4.61 eV. However, the calculated thickness decreases considerably at lower substrate temperatures and higher diamond nucleation densities, and this result may readily explain direct heteroepitaxial diamond nucleation on the Si substrate surface without intermediate layer formation.

The time evolution of surface area, S, covered by growing diamond nuclei is determined from the lateral growth velocity, V_l, of diamond nuclei and the average initial distance, d_0, between individual diamond nuclei for the given N_s. The values of V_l and d_0 are estimated by determining the two-dimensional growth parameters, α_{2D}, and the growth velocity of the {10} crystal face, V_{10}. For T_s = 1200 K and X_{CH_4} = 0.02, a value for the growth velocity, V_{10} = 0.5 μm/h, is adopted from the literature [77]. The value for the two-dimensional growth parameter, α_{2D} = 1.86, is also obtained from the literature [90] for the same operating parameters. For this value of V_{10}, the calculated lateral growth velocity of diamond nuclei is V_l = 0.27 μm/h. Then, for the values of α_{2D} and V_{10} indicated above, the saturated surface number densities of stable nuclei, N_s = 9.9×10^{11}, 2.4×10^{8}, and 8.8×10^{5} cm^{-2}, corresponding to E_a = 1.73, 3.45, and 4.61 eV, respectively, may be used to calculate average initial distance between individual stable nuclei. For the three different adsorption energies E_a = 1.73, 3.45, and 4.61 eV, the distances are d_0 = 1×10^{-6}, 6.5×10^{-5}, and 1.1×10^{-3} cm, respectively.

Figure 3.6 shows the competition in rates associated with intermediate layer growth and surface coverage of growing diamond nuclei. The time evolution of the intermediate layer is determined assuming low surface area covered by diamond nuclei (≤ 1% surface

Reproduced with permission of the copyright owner. Further reproduction prohibited without permission.

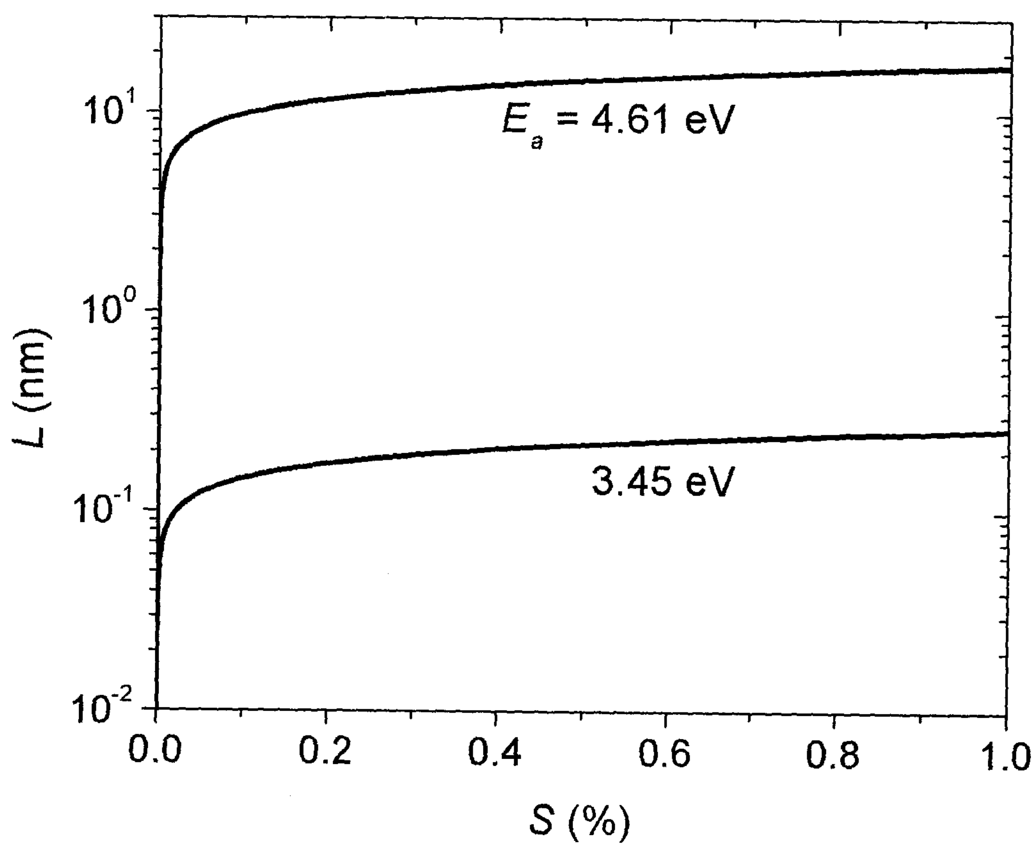

Figure 3.6 Competition in rates associated with intermediate layer growth and surface coverage of growing diamond nuclei for E_a = 3.45 and 4.61 eV. Operating conditions are T_s = 1200 K and $X_{CH_4} = 0.02$.

Reproduced with permission of the copyright owner. Further reproduction prohibited without permission.

area). For T_s = 1200 K and X_{CH_4} = 0.02, the time required to reach the point where diamond nuclei cover 1% surface area is calculated to be 7.2 and 119.1 min for E_a = 3.45 and 4.61 eV, respectively. At these times, the calculated intermediate layer thickness is 0.26 and 17.3 nm for E_a = 3.45 and 4.61 eV, respectively, as shown in Figure 3.6. The time evolution of the surface coverage determined for E_a = 1.73 eV is distinctly different than for the two higher E_a values, and at the lowest adsorption energy it is predicted that the diamond nuclei completely cover the intermediate layer within the first minute. However, such rapid nuclei growth has not been reported.

Comparing the present model results against a number of experimental studies [14,16-18,20,30,34,35], the reported range for the saturated thickness of the β-SiC intermediate layer, 1 to 10 nm, are reproduced by the present model if E_a is chosen to be in the range of 3.7 to 4.5 eV. The present model results also indicate that the β-SiC intermediate layer reaches its saturated thickness during the early stages of diamond deposition, and that this saturated thickness is reached before the growing diamond nuclei cover more than 1% of the intermediate layer surface. Because of this, it is possible to predict the saturated intermediate layer thickness as a function of the operating conditions without having to also consider the presence of the diamond nuclei on the upper surface of the intermediate layer.

3.4 Conclusion

In the present study, a model incorporating gas-phase and surface reactions, surface and bulk diffusion, and heterogeneous diamond nucleation kinetics is applied to predict the time evolution of a β-SiC intermediate layer during the nucleation and the early

Reproduced with permission of the copyright owner. Further reproduction prohibited without permission.

growth stages of diamond growth under the operating conditions typical of diamond nucleation in HFCVD reactors. The model also quantifies the dependence of the time evolution of the layer on operating parameters such as substrate temperature and inlet gas composition. The time scales associated with diamond nuclei growth and intermediate layer growth are compared by calculating the rate competition associated with intermediate layer growth and surface coverage of growing diamond nuclei. Different published adsorption energies of gaseous hydrocarbon species on the surface of the intermediate layer—ranging from 1.43 to 4.61 eV—are tested to determine an adsorption energy value consistent with the saturation times and final thicknesses (1 to 10 nm) reported in the literature. Moreover, the operating conditions that typically lead to intermediate layer formation prior to diamond deposition are compared with those conditions that yield heteroepitaxial diamond nucleation without intermediate layer formation.

The present model results confirm that higher adsorption energies—3.45 and 4.61 eV—lead to larger surface concentrations of carbon atoms, lower saturated nucleation densities, and, therefore, larger β-SiC intermediate layer thicknesses. The saturated nucleation density approximated for an adsorption energy of 4.61 eV is typically below 10^6 cm^{-2}, in agreement with the nuclei density values reported in the literature. For operating parameters typical of diamond nucleation in HFCVD reactors, T_s = 1200 K and X_{CH_4} = 0.01, the calculated intermediate layer thickness for E_a = 4.61 eV reaches 1 nm within 33 s and 10.5 nm during a 1h deposition time. However, for E_a = 3.45 eV, the intermediate layer thickness is much less than for E_a = 4.61 eV and does not reach 1 nm during the same 1h deposition time. The intermediate layer thickness increases at higher substrate temperatures and higher inlet hydrocarbon concentrations. The intermediate

Reproduced with permission of the copyright owner. Further reproduction prohibited without permission.

layer thickness dependence on substrate temperature is significant due to large increases in the magnitude of the bulk diffusion coefficient for carbon diffusion into the intermediate layer with increasing substrate temperature. The calculations of the rate competition associated with intermediate layer growth and surface coverage of growing diamond nuclei reveal that the intermediate layer thickness becomes saturated at the higher adsorption energies when growing diamond nuclei cover a very small fraction of the upper surface of the intermediate layer. Comparing these calculated results to the literature, the reported saturated thickness of the β-SiC intermediate layer, 1 to 10 nm, is predicted by the model if the true adsorption energy is in the range of 3.7 to 4.5 eV. Further, the significant decrease in the intermediate layer thickness at lower substrate temperatures and at higher diamond nucleation densities may provide the explanation for direct heteroepitaxial diamond nucleation on the Si substrate surface without intermediate layer formation.

Reproduced with permission of the copyright owner. Further reproduction prohibited without permission.

3.5 References

1. J. Singh, J. Mater. Sci. **29**, 2761 (1994).

2. K.V. Ravi and C.A. Koch, Appl. Phys. Lett. **57**, 348 (1990).

3. K.V. Ravi, J. Mater. Res. **7**, 384 (1992).

4. C. Trevor, D. Cherns, and P. Southworth, in proceedings of Institute Physics, Electron Microscopy and Analysis Group Conference, edited by F.J. Humphreys (IOP, Bristol, UK, 1991), pp.275.

5. J.J. Dubray, C.G. Pantano, M. Meloncelli, and E. Bertran, J. Vacuum Sci. & Technol. A **9**, 3012 (1991).

6. K. Tamaki, Y. Watanabe, Y. Nakamura, and S. Hirayama, Thin Solid Films **236**, 115 (1993).

7. P.N. Barnes and R.L.C. Wu, Appl. Phys. Lett. **62**, 37 (1993).

8. R. Csencsits, J. Rankin, R.E. Boekenhauer, M.K. Kundmann, and B.W. Sheldon, in Evolution of Surface and Thin Film Microstructure Symposium, edited by H.A. Atwater, E. Chason, M.H. Grabow, and M.G. Lagally (MRS, Pittsburgh, PA, 1993), pp. 695.

9. A.A. Smolin, S.M. Pimenov, V.G. Ralchenko, T.V. Kononenko, V.I. Konov, and E.N. Loubnin, Diamond Films and Technol. **3**, 1 (1993).

10. D.N. Belton and S.J. Schmieg, Thin Solid Films **212**, 68 (1992).

11. T.P. Ong, F. Xiong, R.P.H. Chang, and C.W. White, J. Mater. Res. **7**, 2429 (1992).

12. W.R.L. Lambrecht, C.H. Lee, B. Segall, J.C. Angus, Z. Li, and M. Sunkara, Nature **364**, 607 (1993).

Reproduced with permission of the copyright owner. Further reproduction prohibited without permission.

13. X. Peng and H. Li, Mater. Lett. **17**, 223 (1993).

14. R. Meilunas, M.S. Wong, K.C. Sheng, R.P.H. Chang, and R.P. VanDuyne, Appl. Phys. Lett. **54**, 2204 (1989).

15. A.R. Badzian and T. Badzian, Surf. Coat. Technol. **36**, 283 (1988).

16. B.E. Williams and J.T. Glass, J. Mater. Res. **4**, 373 (1989).

17. D.N. Belton, S.J. Harris, S.J. Schmieg, A.M. Weiner, and T.A. Perry, Appl. Phys. Lett. **54**, 416 (1989).

18. B.E. Williams, J.T. Glass, R.F. Davis, and K. Kobashi, J. Crystal Growth **99**, 1168 (1990).

19. S. Yugo, T. Kimura and T. Muto, Vacuum **41**, 1364 (1990).

20. B.R. Stoner, G.H.M. Ma, S.D. Wolter, and J.T. Glass, Phys. Rev. B **45**, 11067 (1992).

21. S.D. Wolter, B.R. Stoner, G.H.M. Ma, and J.T. Glass, in Novel Forms of Carbon Symposium, edited by C.L. Renschler, J.J. Pouch, and D.M. Cox (MRS, Pittsburgh, PA, 1992), pp. 347.

22. Y.H. Shing, F.S. Pool, and D.H. Rich, Thin Solid Films **212**, 150 (1992).

23. B.R. Stoner, S.R. Sahaida, J.P. Bade, P. Southworth, and P.J. Ellis, J. Mater. Res. **8**, 1334 (1993).

24. D. Kim, H. Lee, and J. Lee, J. Mater. Sci. **28**, 6704 (1993).

25. E.G. Wang, Physica B **185**, 85 (1993).

26. G.A. Hirata, L. Cota-Araiza, M. Avalos-Borja, M.H. Farias, O. Contreras, and Y. Matsumoto, J. Phys. A **5**, 305 (1993).

Reproduced with permission of the copyright owner. Further reproduction prohibited without permission.

27. K. Kobayashi, N. Mutsukura, Y. Machi, and T. Nakano, Diamond Relat. Mater. **2**, 278 (1993).

28. S.D. Wolter, B.R. Stoner, J.T. Glass, P.J. Ellis, D.S. Buhaenko, C.E. Jenkins, and P. Southworth, Appl. Phys. Lett. **62**, 1215 (1993).

29. M.C. Polo, J. Cifre, and J. Esteve, Diamond Relat. Mater. **3**, 492 (1994).

30. N. Jiang, B.W. Sun, Z. Zhang, and Z. Lin, J. Mater. Res. **9**, 2695 (1994).

31. S.D. Wolter, J.T. Glass, and B.R. Stoner, J. Appl. Phys. **77**, 5119 (1995).

32. T. Suesada, N. Nakamura, H. Nagasawa, and H. Kawarada, Jpn. J. Appl. Phys. **34**, 4898 (1995).

33. Y. Ma, T. Tsurumi, N. Shinoda, and O. Fukunaga, Diamond Relat. Mater. **4**, 1325 (1995).

34. Z. Sun, Y. Sun, X. Wang, and Z. Zheng, Mater. Sci. Eng. B **34**, L13 (1995).

35. G. Jubber and D.K. Milne, Phys. Stat. Sol. A **154**, 185 (1996).

36. W. Kulisch, L. Ackermann, and B. Sobisch, Phys. Stat. Sol. A **154**, 155 (1996).

37. E.J. Corat, N.G. Ferreira, V.J. Trava-Airoldi, N.F. Leite, R.C. Mendes de Barros, and K. Iha, J. Mat. Sci. Lett. **16**, 197 (1997).

38. L.C. Nistor, J.V. Landuyt, V.G. Ralchenko, E.D. Obraztsova, and A.A. Smolin, Diamond Relat. Mater. **6**, 159 (1997).

39. S.B. Iyer and S. Srinivas, Thin Solid Films **305**, 259 (1997).

40. G. Sánchez, W.L. Wang, M.C. Polo, and J. Esteve, Diamond Relat. Mater. **7**, 200 (1998).

41. M. Chiang and M. Hon, J. Crystal Growth **211**, 211 (2000).

Reproduced with permission of the copyright owner. Further reproduction prohibited without permission.

42. K.V. Ravi, C.A. Koch, H.S. Hu, and A. Joshi, J. Mater. Res. **5**, 2356 (1990).

43. D. Michau, B. Tanguy, G. Demazeau, M. Couzi, and R. Cavagnat, Diamond Relat. Mater. **2**, 19 (1993).

44. Z. Li, L. Wang, T. Suzuki, A. Argoitia, P. Pirouz, and J. Angus, J. Appl. Phys. **73**, 711 (1993).

45. J.A. Baglio, B.C. Fransworth, S. Hankin, C. Sung, J. Hefter, and M. Tabasky, in Diamond and Diamond-like Films and Coatings, edited by R.E. Clausing, L.L. Horton, J.C. Angus, and P. Koidl (Plenum Press, New York, 1991), pp. 635.

46. P. Mahalingam and D.S. Dandy, Thin Solid Films **322**, 108 (1998).

47. R. Haubner and B. Lux, Diamond Relat. Mater. **2**, 1277 (1993).

48. J. Graul and E. Wagner, Appl. Phys. Lett. **21**, 67 (1972).

49. C.J. Magab and H.J. Leamy, J. Appl. Phys. **45**, 1075 (1974).

50. A.J. Steckl and J.P. Li, Thin Solid Films **216**, 149 (1992).

51. J.P. Li, A.J. Steckl, I. Golecki, F. Reidinger, L. Wang, X.J. Ning, and P. Piroux, Appl. Phys. Lett. **62**, 3135 (1993).

52. J.P. Li and A.J. Steckl, J. Electrochem. Soc. **142**, 634 (1995).

53. B. Bahavar, M.I. Chaudhry, and R.J. Mccluskey, Appl. Phys. Lett. **63**, 914 (1993).

54. N. Bécourt, J.L. Ponthenier, A.M. Papon, and C. Jaussaud, Physica B **185**, 79 (1993).

55. G. Ferro, Y. Monteil, H. Vincent, V. Thevenot, M.D. Tran, F. Cauwet, and J. Bouix, J. Appl. Phys. **80**, 4691 (1996).

Reproduced with permission of the copyright owner. Further reproduction prohibited without permission.

56. G. Ferro, Y. Monteil, H. Vincent, F. Cauwet, J. Bouix, P. Durupt, J. Olivier, and R. Bisaro, Thin Solid Films **278**, 22 (1996).

57. V. Cimalla, J. Pezoldt, G. Ecke, and G. Eichhorn, Inst. Phys. Conf. Ser. **142**, 153 (1996).

58. H. Romanus, V. Cimalla, A. Kromka, J. Scheiner, L. Spieb, and J. Pezoldt, Mater. Sci. Eng. B **47**, 274 (1997).

59. C. Bittencourt, M. De Seta, and F. Evangelisti, J. Vac. Sci. Tchnol. B **16**, 1599 (1998).

60. C.A. Zorman, S. Roy, C.H. Wu, A.J. Fleischman, and M. Mehregany, J. Mater. Res. **13**, 406 (1998).

61. C.D. Stinespring and J.C. Wormhoudt, J. Appl. Phys. **45**, 1075 (1974).

62. M. Tomellini, R. Polini, and V. Sessa, J. Appl. Phys. **70**, 7573 (1991).

63. E. Molinari, R. Polini, M.L. Terranova, P. Ascarelli, and S. Fontana, J. Mater. Res. **7**, 1778 (1992).

64. E. Molinari, R. Polini, V. Sessa, M.L. Terranova, and M. Tomellini, J. Mater. Res. **8**, 785 (1993).

65. E. Molinari, R. Polini, and M. Tomellini, J. Mater. Res. **8**, 798 (1993).

66. M. Tomellini, J. Mater. Res. **8**, 1596 (1993).

67. H. Liu and D.S. Dandy, J. Electrochem. Soc. **143**, 1104 (1996).

68. M.H. Hon and R.F. Davis, J. Mater. Sci. **14**, 2411 (1979).

69. J.A. Venables, Philos. Mag. **27**, 697 (1973).

70. P. Mahalingam, H. Liu, and D.S. Dandy, J. Appl. Phys. **81**, 1966 (1997).

Reproduced with permission of the copyright owner. Further reproduction prohibited without permission.

71. M. Ohring, The Materials Science of Thin Films, (Academic Press, Harcourt Brace Jovanovich Publications, Boston, MA, 1992).

72. M.E. Coltrin, R.J. Kee, G.H. Evans, E. Meeks, F.H. Rupley, and J.F. Grear, Report No. SAND 91-8003 (1991).

73. R.J. Kee, F.M. Rupley, and J.A. Miller, Report No. SAND 89-8009B (1993).

74. M.E. Coltrin, R.J. Kee, and F.M. Rupley, Report No. SAND 90-8003B (1991).

75. R.J. Kee, G. Dixon-Lewis, J. Warnatz, M.E. Coltrin, and J.A. Miller, Report No. SAND 86-8246 (1986).

76. M.E. Coltrin and D.S. Dandy, J. Appl. Phys. **74**, 5803 (1993).

77. C.C. Battaile, D.J. Srolovitz, I.I. Oleinik, D.G. Pettifor, A.P. Sutton, S.J. Harris, and J.E. Butler, J. Chem. Phys. **111**, 4291 (1999).

78. M.D. Allendorf and R.J. Kee, J. Electrochem. Soc. **138**, 841 (1991).

79. R.B. Jackman, L.H. Chua, and J.S. Ford, Surf. Sci. **292**, 47 (1993).

80. K. Feng, Z.H. Liu, and Z. Lin, Surf. Sci. **329**, 77 (1995).

81. A.J. Dyson and P.V. Smith, Surf. Sci. **396**, 24 (1998).

82. J.A. Venables, G.D.T. Spiller, and M. Hanbücken, Rep. Prog. Phys. **47**, 399 (1984).

83. B. Lewis, Thin Solid Films **1**, 85 (1967).

84. G. Zinsmeister, Thin Solid Films **4**, 363 (1969).

85. B. Lewis and D.S. Campbell, J. Vac. Sci. Technol. **4**, 209 (1967).

86. J.C. Fisher, J. Appl. Phys. **22**, 74 (1951).

87. T. Suzuoka, Jpn. J. Phys. Soc. **19**, 839 (1964).

Reproduced with permission of the copyright owner. Further reproduction prohibited without permission.

88. J. Crank, The Mathematics of Diffusion, (Oxford University Press, Ely House, London, UK, 1975).

89. C. Wild, N. Herres, and P. Koidl, J. Appl. Phys. **68**, 973 (1990).

90. C. Wild, P. Koidl, W. Muller-Sebert, H. Walcher, R. Kohl, N. Herres, R. Locher, R. Samlenski, and R. Brenn, Diamond Relat. Mater. **2**, 158 (1993).

91. D.J. Srolovitz, D.S. Dandy, J.E. Bulter, C.C. Battaile, and Paritosh, JOM **49**, 42 (1997).

92. D.S. Dandy and M.E. Coltrin, J. Appl. Phys. **76**, 3102 (1994).

93. Y.S. Cheng, C.H. Sho, and G.F. Shu, J. Crystal Growth **99**, 1196 (1990).

94. J.W. Kim, Y.J. Baik, and K.Y. Eun, in Applications of Diamond Films and Relat. Mater., edited by Y. Tzeng, M. Yoshikawa, and A. Feldman (Elsevier Science Publications, Amsterdam, 1991), pp. 399.

Reproduced with permission of the copyright owner. Further reproduction prohibited without permission.

Chapter 4

A MODEL OF MORPHOLOGY EVOULTION IN THE GROWTH OF POLYCRYSTALLINE β-SiC FILMS

4.1 Introduction

One of silicon carbide polytypes, β-SiC, is considered as an excellent candidate for use in high-power electronic applications. However, the difficulty in achieving single crystal films and uniform surface texture via CVD has limited the possible application of β-SiC.

The surface morphology of a continuous polycrystalline β-SiC film is determined by the reactor operating conditions, including the substrate temperature and the inlet gas composition. At this time, the effects of these operating parameters on the resulting surface morphology are not fully understood. An understanding of the relationships between operating conditions and film morphology may lead to optimal yield of films that are highly <100>-textured, with {100} facets.

The van der Drift model [1,2] represents a growth mechanism of continuous polycrystalline films from randomly oriented nucleated seed crystals. This model calculates the crystallographic texture and the surface morphology of the continuous polycrystalline film resulting from growth competition between nucleated seed crystals. As the film thickness increases and a continuous film is formed, those crystals having their fastest

The text of Chapter 4 consists of an article which appears in Diamond and Related Materials 9 (2000).

Reproduced with permission of the copyright owner. Further reproduction prohibited without permission.

growth direction perpendicular to the substrate surface will overgrow all other orientations and the orientation of the crystals are represented on the surface. The model is expressed by the growth-rate parameter, $\alpha_{3D} = \sqrt{3}V_{100}/V_{111}$, where V_{100} and V_{111} are the growth velocities of the {100} and {111}-facets. The α_{3D} value can be determined from the texture of a continuous polycrystalline film, assuming the absence of secondary nucleation and twinned crystals [2]. After the film growth rate, V_{100}, is determined, the growth rate of {111} face, V_{111}, can be calculated from the known values of α_{3D} and V_{100}.

During the past several years X-ray diffraction (XRD) has been used to determine the effects of operating parameters on the polycrystalline β-SiC film orientation. Many investigators [3-12] have reported XRD data for the growth of β-SiC films on Si(100) substrates using atmospheric-pressure CVD and a SiH_4, C_3H_8, H_2 inlet gas mixture. Using XRD, these investigators have examined the dependence of β-SiC morphology on substrate temperature and inlet Si:C atom ratio. Among them, Wu et al. [3] reported a serial XRD pattern from polycrystalline β-SiC films grown at substrate temperatures from 1263 K to 1433 K and an inlet Si:C ratio of 0.42. They found that, while the preferred orientation of continuous polycrystalline films was (111) at 1323 K with negligible degree of (100) orientation, it changed to (100) by increasing the substrate temperature to 1433 K.

Since, two preferred surface orientations, {100} and {111}, are usually observed in β-SiC atmospheric pressure CVD (APCVD) growth on Si(100) substrates using a silane-propane-hydrogen inlet reactant gas mixture [3-12], the model can be simplified to the growth of two-dimensional crystals from the growth of three-dimensional crystals. In two-dimensional model, the growth-rate parameter, α_{2D}, is $\sqrt{2}V_{10}/V_{11}$, and V_{10} and V_{11}

Reproduced with permission of the copyright owner. Further reproduction prohibited without permission.

are the growth velocities of the {10} and {11} facets. This approach is restricted to the situation where SiC is deposited on Si(100) substrates; when SiC is grown on Si(111), {110} and {111} orientations are typically observed.

Although it has been possible in the present study to correlate the growth parameter α_{2D} with operating conditions using published experiments, it has proven difficult to extract consistent growth rate data from same body of work. In an attempt to quantify the dependence of growth rate on deposition conditions, Allendorf and Kee [13] calculated the SiC growth rate as a function of substrate temperature and Si:C inlet atom ratio through the use of a detailed gas-phase and surface chemical kinetic mechanisms. Allendorf and Kee considered steady-state, rotating disk APCVD of SiC from a SiH_4 and C_3H_8 mixture in H_2 carrier gas. Using the validated theoretical results of Allendorf and Kee, it has been possible to obtain realistic values for the growth rate of (100)β-SiC, and these are used, along with the experimentally-determined values of α_{2D}, in a morphology evolution model to study the effect of operating conditions on film texture and roughness.

The purpose of the present work is to predict the dependence of the surface morphology of β-SiC films grown by CVD on substrate temperature and inlet atomic ratio of Si to C, and to model the morphological evolution of the growing polycrystalline film. In this study, β-SiC APCVD films grown on Si(100) substrate with inlet gas mixture SiH_4-C_3H_8-H_2 are considered. The growth rates of the films are calculated from a numerical model applied to a pedestal reactor, using gas-phase momentum, mass, and energy conservation equations containing detailed homogeneous and heterogeneous chemistry. The growth rate parameter α_{2D} is determined empirically from the texture of continuous β-SiC films reported in the literature [3-12]. Finally, a two-dimensional numerical model

Reproduced with permission of the copyright owner. Further reproduction prohibited without permission.

based on the growth-rate parameter α_{2D} and the film growth rate is used to simulate the evolution of the surface morphology.

4.2 Model Description

A numerical model is applied to calculate growth rates of β-SiC films in stagnation flow (pedestal) reactors. Calculations are also performed to determine the effects of operating conditions such as substrate temperatures and Si:C inlet atom ratio on the growth rate. A computer program [14] is used to compute gas-phase composition, temperature and velocity profiles, and deposition rates. The Fortran chemical kinetic codes called Chemkin-III [15] and Surface Chemkin [16] are used for the analysis of gas-phase and surface chemical kinetics. The gas-phase reaction and surface reaction mechanisms used in the calculations are simplified from those reported by Allendorf and Kee [13]. The gas-phase multicomponent transport properties are calculated by using a computer package [17].

The evolution of surface morphology of two-dimensional polycrystalline β-SiC films is simulated by a two-dimensional numerical model, which is based on prescribed values of the growth rate parameter α_{2D} and the film growth rate, V_{10}. Initially, randomly oriented seed crystals are placed at random locations on the substrate, and each face of each crystal is propagated over a finite time step using the prescribed α_{2D} and V_{10}.

4.3 Results and Discussion

As stated in the Introduction, the values of α_{2D} used in the study are based on published XRD data taken from β-SiC films grown on Si(100) using SiH_4, C_3H_8, and H_2.

Reproduced with permission of the copyright owner. Further reproduction prohibited without permission.

Those data were taken at substrate temperatures ranging from 1323 K – 1673 K, and inlet Si:C atom ratios between 0.2 and 0.83. The experimental results indicate that the SiC films have (100)-preferred orientations at substrate temperatures above approximately 1423 K and for inlet Si:C ratios between 0.3 and 0.83. In those studies, as long as the inlet Si:C ratio was below unity, the resulting film orientation was relatively insensitive to that parameter when the substrate temperature was above 1423 K. These observations are consistent with thermodynamic calculations of the Si-C system, which predict that optimum values of Si:C in the gas phase will be slightly less than 1 for single-phase growth of SiC [18,19].

4.3.1 Simulations of Film Growth Rate

Although the surface reaction mechanism of β-SiC growth proposed by Allendorf and Kee [13] is somewhat complex, the mechanism can be simplified if the goal is solely to determine the growth rate. Numerical calculations have been performed to obtain a simplified surface reaction mechanism for β-SiC growth. The reaction rate of each elementary surface reaction has been evaluated to identify the predominant surface reactions from the detailed surface reaction mechanism. It is found that, among carbon-containing species, heterogeneous reactions involving CH_4, C_2H_2, and C_2H_4 are the most important, and among the Si-containing gas species, the heterogeneous reactions involving SiH_2 and Si are the most significant. The simplified surface reaction mechanism is listed in Table 4.1.

The growth rates have been calculated at different substrate temperatures that are to be used in the two-dimensional morphology evolution model. In the model the substrate temperature is varied between 1323 K and 1623 K. The upper limit of substrate temperat-

Reproduced with permission of the copyright owner. Further reproduction prohibited without permission.

Table 4.1 Simplified surface reaction mechanism.

Reaction	*A*	β	*E*
$H + Si(S) \rightarrow Si(S)\text{-}H$	2.180E+12	0.5	0.0
$H + C(S) \rightarrow C(S)\text{-}H$	2.180E+12	0.5	0.0
$2Si(S)\text{-}H \rightarrow 2Si(S) + H_2$	7.230E+24	0.0	61000.0
$2C(S)\text{-}H \rightarrow 2C(S) + H_2$	7.230E+24	0.0	61000.0
$CH_4 + Si(S) \rightarrow C(S) + Si(B) + 2H_2$	4.197E+07	0.5	0.0
$C_2H_4 + 2Si(S) \rightarrow 2C(S) + 2H_2 + 2Si(B)$	9.367E+17	0.5	0.0
$C_2H_2 + 2Si(S) \rightarrow 2C(S) + 2Si(B) + H_2$	1.216E+19	0.5	0.0
$SiH_2 + C(S) \rightarrow C(B) + SiH_2(S)$	6.120E+11	0.5	0.0
$Si + C(S) \rightarrow B_2(B) + Si(S)$	6.334E+11	0.5	0.0
$2CH(S) \rightarrow 2C(S) + H_2$	2.250E+24	0.0	61000.0
$2SiH(S) \rightarrow 2Si(S) + H_2$	2.250E+24	0.0	61000.0
$SiH_2(S) \rightarrow Si(S) + H_2$	2.912E+14	0.0	9000.0

Arrhenius parameters in form $k_i = AT^\beta \exp(-E/RT)$ in units (*A* in moles, cubic centimeters, and seconds; *E* in cal/mole). The surface radical sites and bulk species are represented by S and B.

ure 1623 K is chosen to avoid the melting point of the Si substrate, which is 1683 K [13]. Other operating conditions are chosen to match the experimental data of Wu, et al. [3]. The Si:C inlet atomic ratio is fixed at 0.42, a standard value. The inlet mole fractions of SiH_4 and C_3H_8 are set to 2.0×10^{-4} and 1.6×10^{-4}. The inlet mole fraction ratio of H_2:(SiH_4 + C_3H_8) is 2778.

The predicted growth rate of β-SiC as a function of substrate temperature is shown in Figure 4.1. At lower temperatures, the strong dependence of β-SiC growth rate on temperature indicates that the growth rate is surface reaction rate limited. The dominant rate-limiting mechanism changes from the surface reaction rate to the mass transfer rate as the substrate temperature increases. This growth rate dependence on the substrate temperature is in reasonable agreement with the results of Wu et al. [3].

Reproduced with permission of the copyright owner. Further reproduction prohibited without permission.

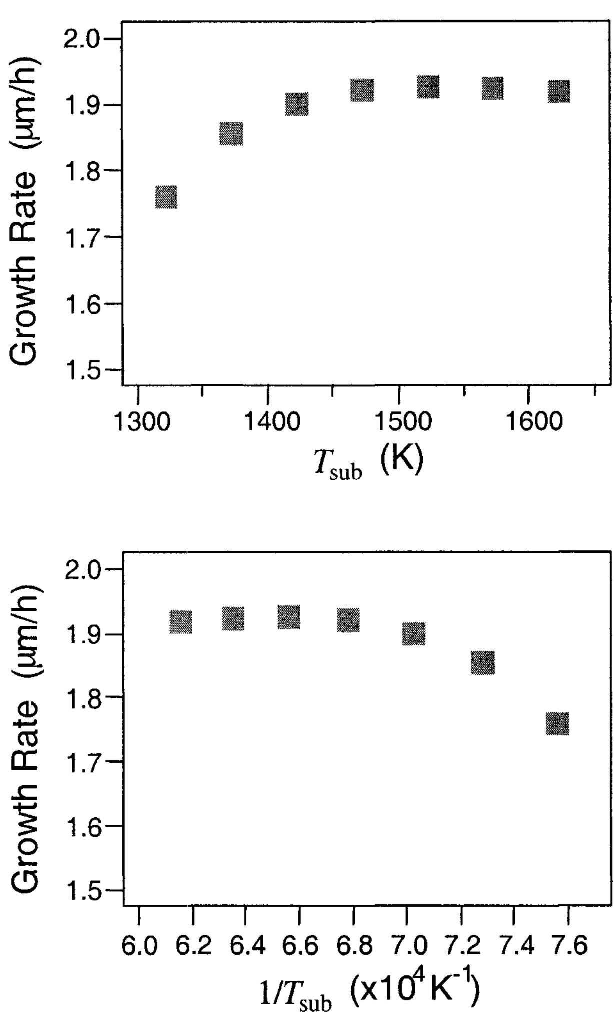

Figure 4.1 Growth rate of β-SiC film as a function of the substrate temperature for operating conditions: inlet gas temperature T_{inlet} = 300 K; reactor pressure P = 760 Torr; inlet axial velocity U_{inlet} = 2.49 cm/s; distance between the inlet and the substrate surface L = 3 cm, and inlet mole fractions: $X_{H_2} = 0.9964$; $X_{SiH_4} = 2\times10^{-4}$; $X_{C_3H_8} = 1.6\times10^{-4}$.

Reproduced with permission of the copyright owner. Further reproduction prohibited without permission.

4.3.2 Simulations of Surface Morphology Evolution

From experimental data [3], it is concluded that the increase of the growth rate parameter α_{2D} from 1 to 1.95 is due mainly to an increase in the substrate temperature from 1323 K to 1423 K. The effect of Si:C inlet atom ratio on the α_{2D} is not considered here because the experiments [3-12] indicate that, for inlet Si:C atom ratios ranging from 0.3 to 0.83, β-SiC films have (100) film texture for substrate temperatures above 1423 K. The two-dimensional numerical model has calculated the surface morphology of polycrystalline β-SiC films based on the growth rate parameter α_{2D} and the growth rate of β-SiC.

Figure 4.2 shows the surface morphologies and the film textures of continuous polycrystalline β-SiC films for two different α_{2D} values: 1.0 and 1.95. The film thickness in the Figure is normalized with respected to the average distance between initial nucleated seed crystals, d_0. When α_{2D} is unity at the substrate temperature of 1323 K as shown in Figures 4.2a and 4.2c, the facets on the thin film, 10 d_0, surface in Figure 4.2a are randomly orientated because, initially, nucleated seed crystals are placed with random rotations across on the substrate surface. However, the film texture has mainly <11> direction and this texture leads to mainly {11}-facets on the surface at the large film thickness, 260 d_0, in Figure 4.2c. When α_{2D} is 1.95 at the substrate temperature of 1423 K as shown in Figures 4.2b and 4.2d, small fraction of {10}-facets is observed at the thin film in Figure 4.2b. The formation of {10}-facets is increased as the film is thickening in Figure 4.2d.

Figure 4.3 shows the dependence of the surface roughness in the average peak-to-valley height on the film thickness and α_{2D} value. The surface roughness significantly in-

Reproduced with permission of the copyright owner. Further reproduction prohibited without permission.

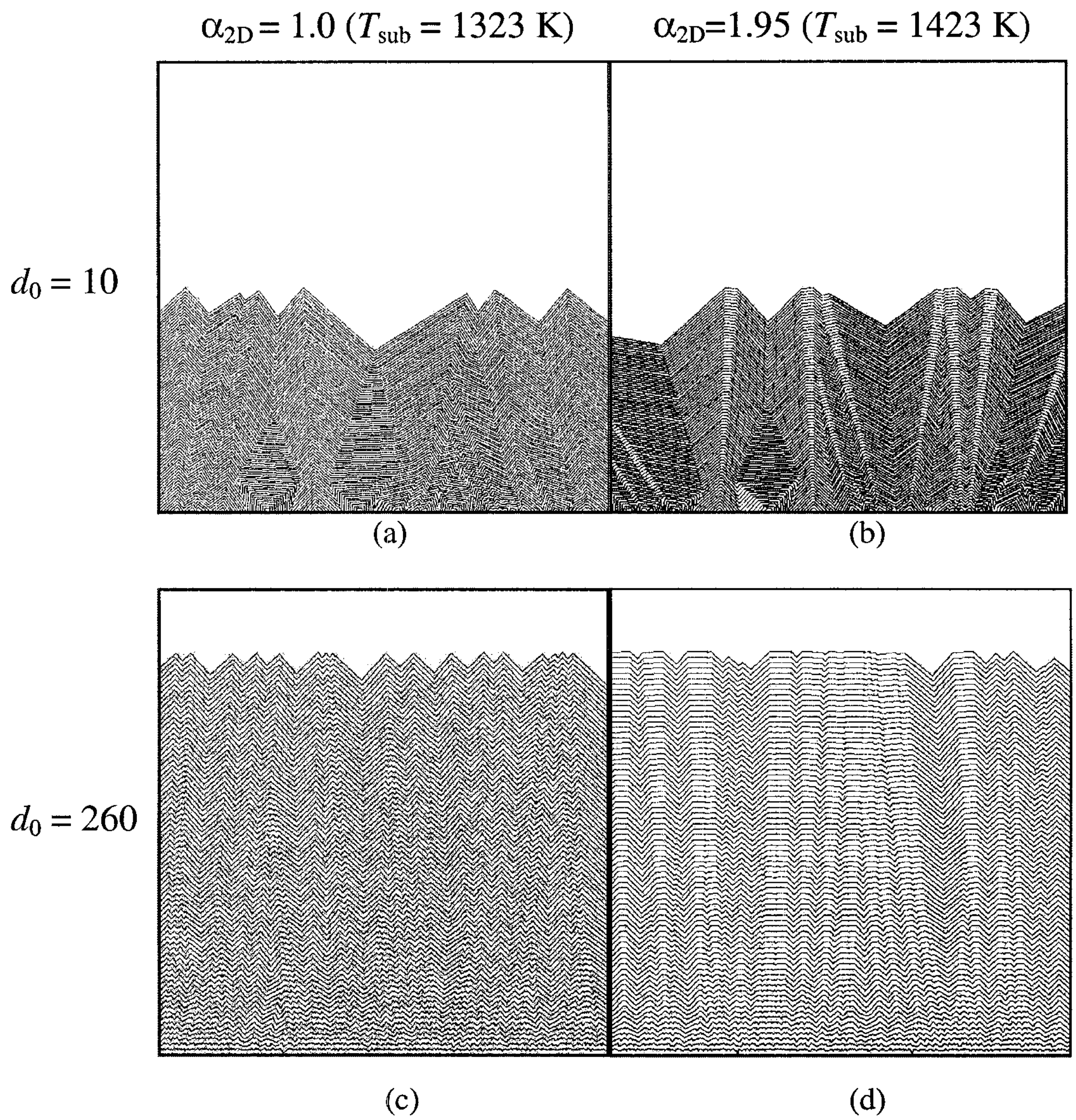

Figure 4.2 Film morphology predicted by two-dimensional numerical model. The average distance between nucleated seed crystals is represented as d_0. Figures (a) and (b) show the relatively thin film (thickness = 10 d_0) morphologies for two different growth parameter values: (a) α_{2D} = 1.0 and (b) α_{2D} = 1.95. Figures (c) and (d) show the relatively thick film (thickness = 260 d_0) morphologies for two different growth parameter values: (c) α_{2D} = 1.0 and (d) α_{2D} = 1.95.

Reproduced with permission of the copyright owner. Further reproduction prohibited without permission.

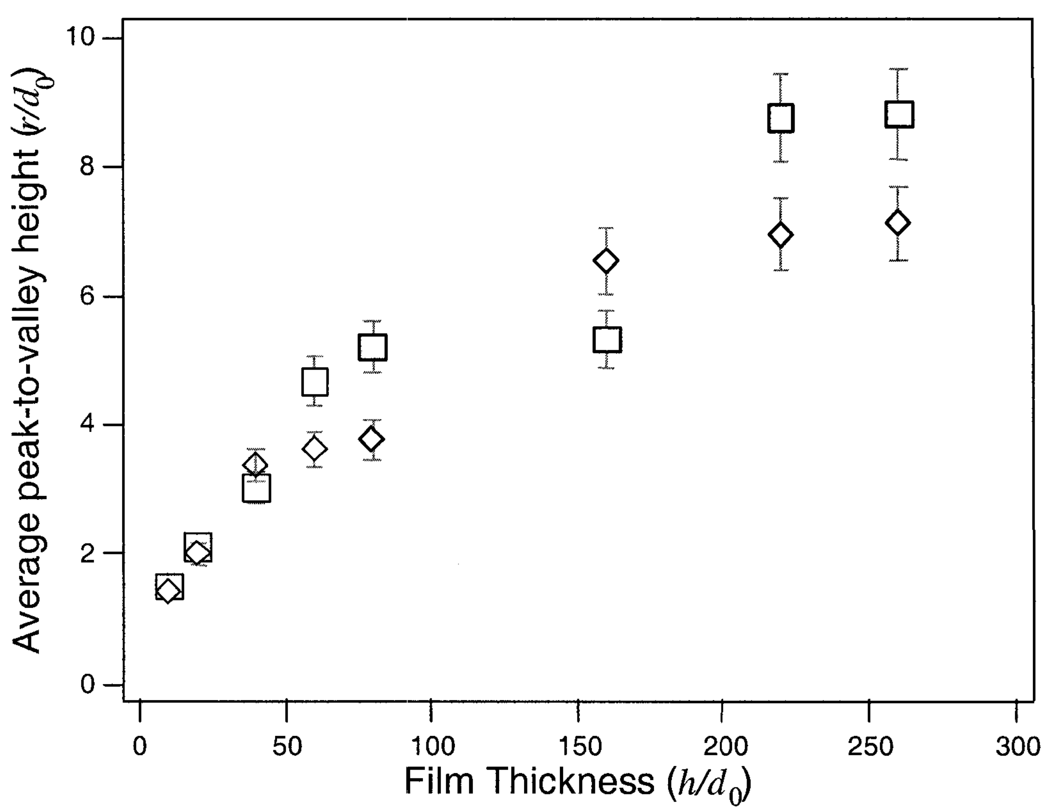

Figure 4.3 Surface roughness prediction for different film thickness and α_{2D} values.

Reproduced with permission of the copyright owner. Further reproduction prohibited without permission.

creases with increasing the film thickness for both α_{2D} values. However, when α_{2D} is 1.95, the surface morphology of the film is smoother than that of unity of α_{2D}. It is therefore suggested that the {10}-facets create an increasingly smoother surface morphology. The evolutions of the relative size of the <10> and <11>-orientated grain and average grain size are shown in Figure 4.4. When α_{2D} is 1.95, the average grain size increases with increasing the film thickness, and the grain size ratio <10>/<11> also increases with film thickness because the preferential orientation <10> of crystallite develops for the α_{2D} value. The increasing rates of the grain size ratio and average grain size with the film thickness are significantly decreased as the film is thickening.

The numerical calculations determining surface morphology and growth rate of β-SiC have been performed for different operating conditions. A two-dimensional morphology evolution model has been used to calculate the texture, surface roughness, and grain size of continuous polycrystalline β-SiC films. The results indicate that the surface morphology and the film texture of β-SiC are strongly affected by the substrate temperature. The results also determine the operating conditions optimizing the smoothness of surface morphology of β-SiC.

Reproduced with permission of the copyright owner. Further reproduction prohibited without permission.

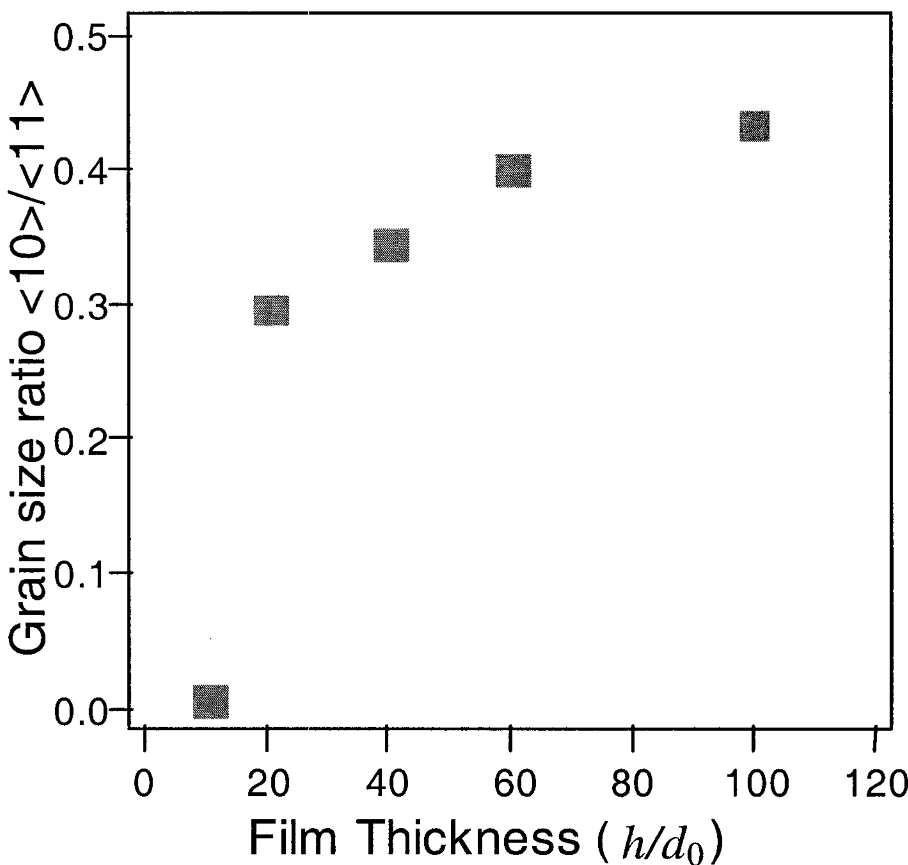

Figure 4.4a Evolutions of the relative sizes of the <10> and <11>-orientated grains with the film thickness when $\alpha_{2D} = 1.95$.

Reproduced with permission of the copyright owner. Further reproduction prohibited without permission.

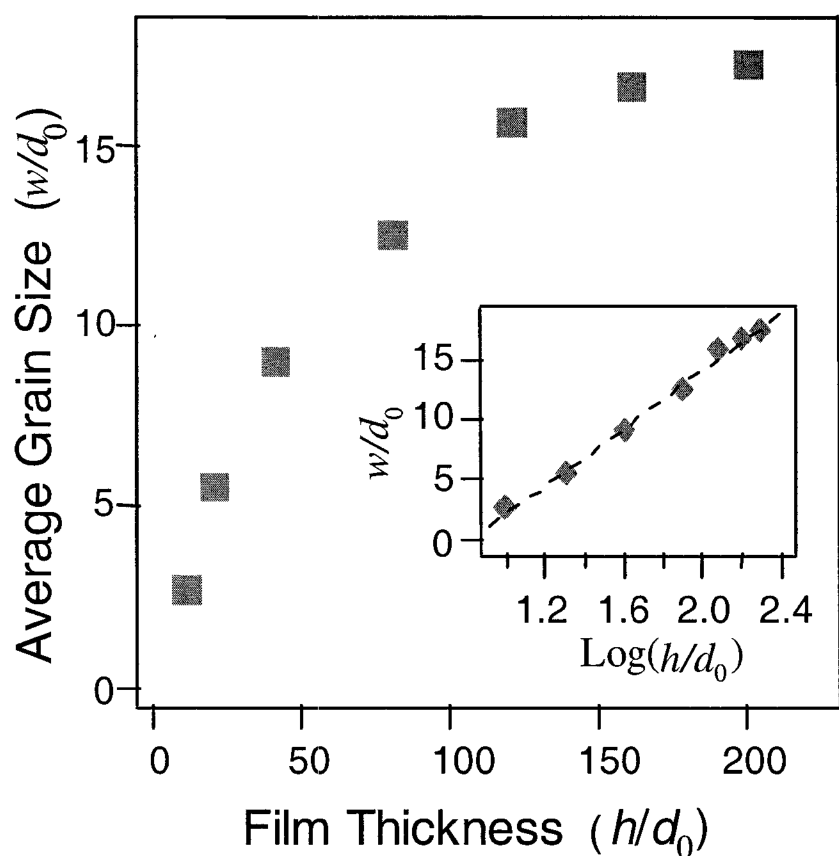

Figure 4.4b Evolutions of the average grain size with the film thickness when α_{2D} = 1.95.

Reproduced with permission of the copyright owner. Further reproduction prohibited without permission.

4.4 References

1. C. Wild, N. Herres, and P. Koidl, J. Appl. Phys. **68**, 973 (1990).
2. C. Wild, P. Koidl, W. Műller-Sebert, H. Walcher, R. Kohl, N. Herres, R. Locher, R. Samlenski, and R. Brenn, Diamond Relat. Mater. **2**, 158 (1993).
3. C. H. Wu, A. J. Fleischman, C. A. Zorman, and M. Mehregany, Mater. Sci. Forum **264-268**, 179 (1998).
4. M. I. Chaudhry and R. L. Wright, J. Mater. Res. **5**, 1595 (1990).
5. A. J. Steckl and J. P. Li, IEEE Transactions on Electron Devices **39**, 64 (1992).
6. C. A. Zorman, A. J. Fleischman, A. S. Dewa, M. Mehregany, C. Jacob, S. Nishino, and P. Pirouz, J. Appl. Phys. **78**, 5136 (1995).
7. S. Nishino, J. A. Powell, and H. A. Will, Appl. Phys. Lett. **42**, 460 (1983).
8. P. E. R. Nordquist, G. Kelner, M. L. Gipe, and P. H. Klein, Mater. Lett. **8**, 209 (1989).
9. O. Kordina, L. O. Björketun, A. Herry, C. Hallin, R. C. Glass, L. Hultman, J. E. Sundgren, and E. Janzen, J. Crystal Growth **154**, 303 (1995).
10. K. Shibahara, S. Nishino, and H. Matsunami, J. Crystal Growth **78**, 538 (1986).
11. M. I. Chaudhry, R. J. McCluskey, and R. L. Wright, J. Crystal Growth **113**, 120 (1991).
12. J. D. Hwang, Y. K. Fang, Y. J. Song, and D. N. Yaung, Thin Solid Films **272**, 4 (1996).
13. M. D. Allendorf and R. J. Kee, J. Electrochem. Soc. **138**, 841 (1991).

Reproduced with permission of the copyright owner. Further reproduction prohibited without permission.

14. M. E. Coltrin, R. J. Kee, G. H. Evans, E. Meeks, F. H. Rupley, and J. F. Grear, Report No. SAND 91-8003 (1991).

15. R. J. Kee, F. M. Rupley, and J. A. Miller, Report No. SAND 89-8009B (1993).

16. M. E. Coltrin, R. J. Kee, and F. M. Rupley, Report No. SAND 90-8003B (1991).

17. R. J. Kee, G. Dixon-Lewis, J. Warnatz, M. E. Coltrin, and J. A. Miller, Report No. SAND 86-8246 (1986).

18. H. J. Kim and R. F. Davis, J. Appl. Phys. **60**, 2897 (1986).

19. A. I. Kingon, L. J. Lutz, P. Liaw, and R. F. Davis, J. American Ceramic Soc. **66**, 558 (1983).

Reproduced with permission of the copyright owner. Further reproduction prohibited without permission.

Chapter 5

A MORPHOLOGICAL STUDY OF DIAMOND FILMS DEPOSITED ON PRETREATED Si SUBSTRATES

5.1 Introduction

When diamond films are deposited on non-diamond substrates—Si in the present study—via chemical vapor deposition (CVD), the island growth mode, or Volmer-Weber growth mode, occurs due to a large lattice mismatch ($\approx$ 41%) between diamond and the Si substrate, and this results in a significant degree of film structure defects that affect film qualities and consequently limit field applications of the material. For diamond films grown on Si substrates, the defects associated with grain boundaries and the undesirable consequences of surface roughness both result from the island growth mode. The grain boundary defect may decrease the thermal and electrical conductivities of diamond films, while the surface roughness negatively impacts the optical properties of diamond films [1-3].

Since the deposited film characteristics—surface roughness, film texture and orientation, and grain size—are strongly affected by the nucleation density, undesirable film morphologies may be minimized by promoting enhanced diamond nucleation on Si substrates. By initiating diamond deposition with a relatively high nucleation density, a continuous diamond film forms on a Si substrate within a relatively short time, with a

Reproduced with permission of the copyright owner. Further reproduction prohibited without permission.

smaller average grain size and a smoother surface than those deposited at a relatively low nucleation density [1,4,5]. A variety of substrate pretreatments, including intentional carbonization and the use of stepped substrate surfaces, may reduce the incubation period and enhance the nucleation density by providing favorable chemical properties and surface conditions for diamond nucleation on Si substrates [6].

For the carbonization of Si substrates under operating conditions conducive to diamond nucleation, a thin β-SiC layer, often 1 to 10 nm thick, may form by the bulk diffusion of carbon atoms through the evolving SiC layer towards the bulk Si [7-14]. The enhancement of diamond nucleation is then achieved on the β-SiC layer through the creation of chemically and structurally favorable sites for nucleation [15]. Thus, the texture and morphology of diamond films may be significantly improved when the films are subsequently grown on the β-SiC intermediate layer [4,16,17]. Regarding the enhancement of diamond nucleation on a β-SiC layer, the role of grain boundaries at the β-SiC layer surface has been identified as a key factor for enhancement [18-20]. The large lattice mismatch ($\approx$ 22%) between SiC and Si promotes dislocations at the interface between the two layers. Significant densities of grain boundaries then develop from dislocations at the interface and progress into the evolving β-SiC layer. The formation of grain boundaries at the β-SiC surface results a increase of the surface energy, and the presence of more vacancies, dislocations, and dangling bonds at grain boundaries provides more favorable sites for diamond nucleation on the β-SiC layer surface. Consequently, large densities of grain boundaries facilitate diamond nucleation on a SiC layer and increase the nucleation density. Experimental observations of diamond nucleation on a β-SiC layer show this significant enhancement in the nucleation density; nucleation

Reproduced with permission of the copyright owner. Further reproduction prohibited without permission.

densities of 5×10^6 and 1×10^7 cm^{-2} were observed on β-SiC (220) films for substrate temperatures of 1123 and 1258 K, respectively [15,21], and those densities are much larger than that on an untreated Si substrate, which has a nucleation density on the order of 10^4 to 10^5 cm^{-2}.

The stepped substrate is an alternative method for enhancing nucleation density, which is based on step-flow growth. Since the chemical bonding of adsorbed atoms at the step edges is more energetically favorable than on the step terraces, diamond nuclei are located preferentially along the step edges, and then adsorbed carbon atoms are incorporated into growing diamond nuclei if carbon atoms added to the surface reach the step edges via the surface diffusion [22-24]. Polini [24] carried out an experimental study of diamond nucleation on stepped substrates with a 1 μm terrace width and a 1 μm step height, and nucleation densities on the order of 10^7 to 10^8 cm^{-2} were observed for a substrate temperature of 873 K. It should be noted, however, that adsorbed atoms may be highly mobile at high substrate temperatures and diffuse across the step edges if the step height is less than a few atomic layers. In such a case, surface diffusion is not necessarily restricted by the step, and the mean diffusion length may be larger than the terrace width. For example, Arnault et al. [22] reported a diamond nucleation density of 2.0×10^8 cm^{-2}, similar to the values measured by Polini [24], for a substrate temperature of 1073 K, but with different surface conditions including a mean terrace width smaller than 10 nm and a step height of a monolayer.

In addition to substrate pretreatment, optimization of operating conditions—reactor pressure, inlet gas composition, and substrate temperature—is also critical for enhancing diamond nucleation. Of those operating conditions, the dependence of the nucleation

Reproduced with permission of the copyright owner. Further reproduction prohibited without permission.

density on substrate temperature is very significant because the adsorption state and surface diffusion length of adsorbed atoms depend strongly on this quantity. Experimental observations indicate that a maximum nucleation density can be obtained at a specific substrate temperature. However, there are conflicting reports as to the optimal temperature, and although it is known to lie somewhere between 1123 and 1273 K [8,25-27], its actual value depends on the specific deposition conditions chosen.

When diamond is grown on pretreated Si substrates via the island growth mode, the crystallographic texture and surface morphology can be described using a mechanistic approach, termed morphology evolution, of orientated crystals from randomly orientated nuclei [28]. In this approach, the texture and morphology of the diamond film are determined by the competition between evolving crystals. As growth proceeds, those crystals having their fastest growth direction perpendicular to the substrate surface overgrow crystals with different orientations, and the orientation of the surviving crystals are then manifested as the film surface [29,30]. The overall film misorientation decreases with increases in film thickness once a continuous film forms, and the misoriented crystals are eventually buried by growing diamond films out to greater thicknesses.

A two-stage CVD process including (1) a nucleation stage and (2) a continuous film growth stage has been successfully demonstrated for the deposition of highly textured diamond films on pretreated Si substrates [31]. The diamond nucleation stage is carried out at a higher substrate temperature and a higher inlet CH_4 mole fraction than the film growth stage [31,32]. The texture and morphology of diamond films are both strongly affected by the growth conditions, which include operating conditions of the nucleation and continuous film growth stages, nucleation density, and film thickness. Accordingly,

Reproduced with permission of the copyright owner. Further reproduction prohibited without permission.

the microstructural and morphological diamond film characteristics—surface roughness, film texture and orientation, and grain size—can be optimized by applying different combinations of the growth conditions. However, determination of the dependence of diamond film characteristics on the growth conditions is not yet sufficiently quantitative to the degree required for precise control of diamond film characteristics.

The present study addresses issues associated with the crystallographic texture and surface morphology of diamond films grown on pretreated Si substrates via a two-stage HFCVD process, consisting of diamond nucleation and continuous film growth stages. The overall goal of this theoretical study is to develop a fundamental understanding of the diamond nucleation and film growth mechanism on different pretreated Si substrates, including flat and stepped β-SiC layers, and apply this knowledge to optimize the texture and morphology of diamond films through control of the deposition conditions. This study thus provides an opportunity to predict quantitative, as well as qualitative, aspects of diamond deposition on pretreated Si substrates. This goal is achieved by accomplishing three objectives: (*i*) the saturated diamond nucleation density is calculated for different pretreated Si substrates under operating conditions representative of those used in diamond nucleation via a HFCVD system; (*ii*) the evolution of a thin β-SiC layer resulting from the Si substrate carbonization is calculated for operating conditions conducive to diamond nucleation; and (*iii*) a morphology evolution model is applied to calculate the texture and morphology of diamond films grown on flat and stepped β-SiC layers during diamond nucleation and continuous film growth stages, and the calculations also determine the dependence of the diamond characteristics on the growth conditions.

Reproduced with permission of the copyright owner. Further reproduction prohibited without permission.

5.2 Model Description

The initial stage of atomic nucleation on a substrate surface is normally described by dividing the nucleation stage into two regimes, termed initially incomplete condensation and complete condensation [33-35]. In the case of initially incomplete condensation, the desorption rate of atoms from the surface exceeds the capture rate of adsorbed atoms diffusing over the surface by growing nuclei. This regime occurs at high temperatures and/or low deposition rates. However, in the initially complete condensation regime the condensation is completed in the beginning through much greater the capture rate of adsorbed atoms by growing nuclei than the desorption rate of these atoms. This regime takes place at low temperatures and/or high deposition rates. The saturated nucleation density increases with the substrate temperature and is independent of the adsorption rate in the initially incomplete condensation regime, while the nucleation density increases with adsorption rate and decreases with the substrate temperature in the initially complete condensation regime. For diamond nucleation, the dependence of the saturated nucleation density on substrate temperature is significant, and the density increases as the substrate temperature is increased up to an optimal nucleation temperature [8,25-27]. Because of this, it is concluded that initially incomplete condensation occurs under operating conditions typical of diamond nucleation. In this condensation regime, the saturated nucleation density, N_s, is given by [33]

$$N_s = \frac{N_0 a^2}{\lambda^2} = 4N_0 \exp\left(-\frac{E_a}{2kT_s}\right), \tag{1}$$

where a is the lattice constant of the substrate, N_0, is the reactive site density and is equal to $2/a^2$ for a face centered cubic (fcc) lattice structure, E_a is the adsorption energy of a

Reproduced with permission of the copyright owner. Further reproduction prohibited without permission.

gaseous hydrocarbon precursor on the substrate, k is Boltzmann's constant, T_s is the substrate temperature, and λ is the mean surface-diffusion length of adsorbed atoms. When $2/a^2$ is substituted into Eq. (1) for N_0, the saturated nucleation density is then $N_s = 2/\lambda^2$. The mean surface-diffusion length can be calculated by [36]

$$\lambda = \sqrt{2D_s\tau_s} = \sqrt{\frac{a^2}{4}\exp\left(\frac{E_a}{2kT_s}\right)}, \qquad (2)$$

where D_s and τ_s are the surface diffusion coefficient and mean surface-residence time of adsorbed atoms, respectively.

The maximum observed value of N_s in diamond nucleation studies on stepped β-SiC layers is 2.0×10^8 cm^{-2} [22], and this corresponds to a predicted free path $\lambda = 1$ μm for the fcc structure. For diamond nucleation on stepped β-SiC layers at low substrate temperatures and/or small step heights, the surface diffusion length of adsorbed atoms is simply the terrace width, W_t, because the surface diffusion of adsorbed atoms would be restricted by the surface step. However, since $N_s = 2.0\times10^8$ cm^{-2} is the maximum observed diamond nucleation density on a stepped β-SiC layer, the N_s value may not increases further as the terrace width is decreased to below 1 μm. The fact suggests that diamond nucleation on stepped β-SiC layers via CVD requires not only the surface diffusion of adsorbed atoms over the terraces but also a particular atomic arrangement for diamond nucleus formation at the steps. In other words, diamond nucleation can be limited by either surface diffusion or nucleation kinetics. On this basis it can be concluded that if $\lambda < 1$ μm diamond nucleation is relevant to the nucleation kinetics limited growth at the steps with rapid surface diffusion of adsorbed atoms over the terraces to the steps.

Reproduced with permission of the copyright owner. Further reproduction prohibited without permission.

To calculate the saturated nucleation density of diamond on a β-SiC layer using Eq. (1), the adsorption energy of a hydrocarbon precursor on the β-SiC surface must be specified. In a previous kinetic modeling study [37], published values of adsorption energy were used to validate an interlayer growth model against the 1 to 10 nm β-SiC layer thicknesses typically observed during the nucleation stage. It was determined that the most probable value of E_a for a hydrocarbon molecule was in the range 3.7 to 4.5 eV. Further, the adsorption energy can be also estimated from diamond nucleation densities reported in the literature. These observations yield N_s values of 5×10^6 [21] and 1×10^7 cm^{-2} [15] for substrate temperatures of 1123 and 1258 K, respectively. Using Eq. (1) the adsorption energies determined from the nucleation densities are 3.9 and 4.5 eV for 1×10^7 and 5×10^6 cm^{-2}, respectively, and those adsorption energies are closely aligned with the predictions of the earlier kinetic modeling study [37].

Since CVD diamond primarily exhibits two crystal faces, {100} and {111}, the growth habit of diamond crystals is generally captured by the relative growth velocities of the {100} and {111} faces on a diamond nucleus [38,39]. Thus, a morphology evolution model, which is described in a previous paper [40], can be geometrically simplified to a mode of the growth of two-dimensional nuclei using the growth-rate parameter, $\alpha_{2D} = \sqrt{2}V_{10}/V_{11}$, where V_{10} and V_{11} are the growth velocities of the {10} and {11} faces. Once V_{10} is determined, V_{11} may be calculated using the α_{2D} value prescribed from the texture of continuous polycrystalline diamond films [30,41-46]. The results show that the predominant face changes from {10} to {11} as either the substrate temperature is increased or the inlet CH_4 mole fraction is decreased. However, the published results are inconsistent regarding the influence of the substrate temperature on the predominant

Reproduced with permission of the copyright owner. Further reproduction prohibited without permission.

facet, and the shift of the predominant facet from {11} to {10} with increases in substrate temperature has been also reported in the literature [47-52].

The growth velocity of the {10} face is computed using a stagnation flow model [53], which contains the necessary detailed homogeneous and heterogeneous kinetics, as well as multicomponent gas phase transport. Chemkin-III [54] and Surface Chemkin [55] are used for analysis of gas-phase and surface chemical kinetics, respectively. The multicomponent transport properties of the gas phase are calculated using a rigorous kinetic theory model [56]. The reversible gas-phase reactions used in the present study are based on an established pyrolysis mechanism [57], and the surface reactions are taken from a published surface reaction mechanism [58].

5.3 Results and Discussion

Calculations are performed to investigate diamond growth accomplished via a two-stage HFCVD process, consisting of a diamond nucleation stage followed by a continuous film growth stage. Operating conditions conducive to diamond nucleation are chosen to yield a high nucleation density, while those conditions for film growth are selected to obtain a high growth rate of a high quality diamond film. To investigate the formation and subsequent growth of diamond nuclei on a β-SiC layer during diamond nucleation, operating conditions typical of diamond nucleation in a HFCVD system are chosen, and these are listed in Table 5.1. The inlet mole fractions are $X_{CH_4} = 0.02$ and $X_{H+H_2} = 0.98$, where a specific degree of heterogeneous H_2 dissociation, $X_H = 0.03$, at the filament temperature is approximated by a linear filament-poisoning model [59]. Calculations are performed for different values of the substrate temperature between 1073 and 1273 K.

Reproduced with permission of the copyright owner. Further reproduction prohibited without permission.

Table 5.1 Operating conditions used in diamond nucleation and continuous film growth stages.

Operating conditions growth	Nucleation		Epitaxial	
Reactor pressure P (torr)		50		
Inlet gas velocity U_∞		1.0 cm/s		
Total volume flow rate Q_t		300 sccm		
Distance from substrate to filament D (cm)		0.5		
Filament temperature T_f (K)		2500		
Substrate temperature T_s (K)	1073 – 1273		1023 – 1173	
Inlet mole fraction				
CH_4 X_{CH_4}	0.02		0.004	0.01
H_2 X_{H_2}	0.95		0.896	0.93
H X_H	0.03		0.1	0.06

Once a continuous diamond film forms, the diamond nucleation stage is terminated through transition to a different set of operating conditions. Since the substrate temperature and the inlet gas composition are the two predominant parameters governing film characteristics, continuous film growth is carried out at lower substrate temperatures and lower inlet CH_4 mole fractions than those used for the diamond nucleation stage [31,32]. For the continuous film growth stage the dependence on operating conditions were examined using the model through variation of the substrate temperature from 1023 to 1173 K and the inlet CH_4 mole fraction from 0.004 and 0.01. Operating conditions used in the film growth stage are also listed in Table 5.1.

5.3.1 Diamond Nucleation Process

Calculations using a kinetic model [37] are carried out to resolve whether operating conditions representative of those used in diamond nucleation on Si substrates, T_s = 1073 to 1273K and X_{CH_4} = 0.02, are necessary and sufficient for β-SiC layer formation as a

Reproduced with permission of the copyright owner. Further reproduction prohibited without permission.

result of substrate carbonization, during the initial stages of diamond nucleation. If the lattice constant of β-SiC, 4.35 Å, is chosen as the minimum thickness necessary for identification of a distinct β-SiC layer, the formation time, τ_f, of this layer is shown in Figure 5.1 as a function of T_s for two different E_a values, 3.9 and 4.5 eV. The results indicate that τ_f decreases with increasing T_s and E_a, and the β-SiC layer forms within minutes for T_s = 1273 K and E_a = 4.5 eV. For example, the predicted τ_f values corresponding to E_a = 3.9 and 4.5 eV are 18 and 1 s, respectively, for T_s = 1273 K. However, for T_s = 1073 K, those values corresponding to E_a = 3.9 and 4.5 eV are 178 and 7 min, respectively. Since experimental observations suggest that the incubation period and diamond nucleation take from several minutes up to hours [60], the results readily explain the formation of the β-SiC layer during the initial stages of diamond nucleation for an appropriate choice of operating conditions.

The saturated nucleation density, N_s, and the {10}-face growth velocity, V_{10}, are treated as parameters in the morphology evolution model used in the present study. The saturated nucleation density is calculated for two different pretreated Si substrates, including flat and stepped β-SiC layers, as shown in Figure 5.2. For the flat β-SiC layer, N_s is also determined for two different E_a values of 3.9 and 4.5 eV, as a function of T_s in the range between 1073 and 1273 K. Since the value of N_s is dependent primarily on the surface diffusion rate of adsorbed atoms, N_s increases considerably by increasing T_s and/or decreasing E_a. However, for the stepped β-SiC layer, the value of N_s is controlled by changes in the terrace width, W_t, rather than T_s and E_a, for the values considered here. For W_t > 1 μm, the surface diffusion length of adsorbed atoms decreases as W_t is decreased, and as a result the value of N_s increases as W_t is decreased. Nevertheless, the

Reproduced with permission of the copyright owner. Further reproduction prohibited without permission.

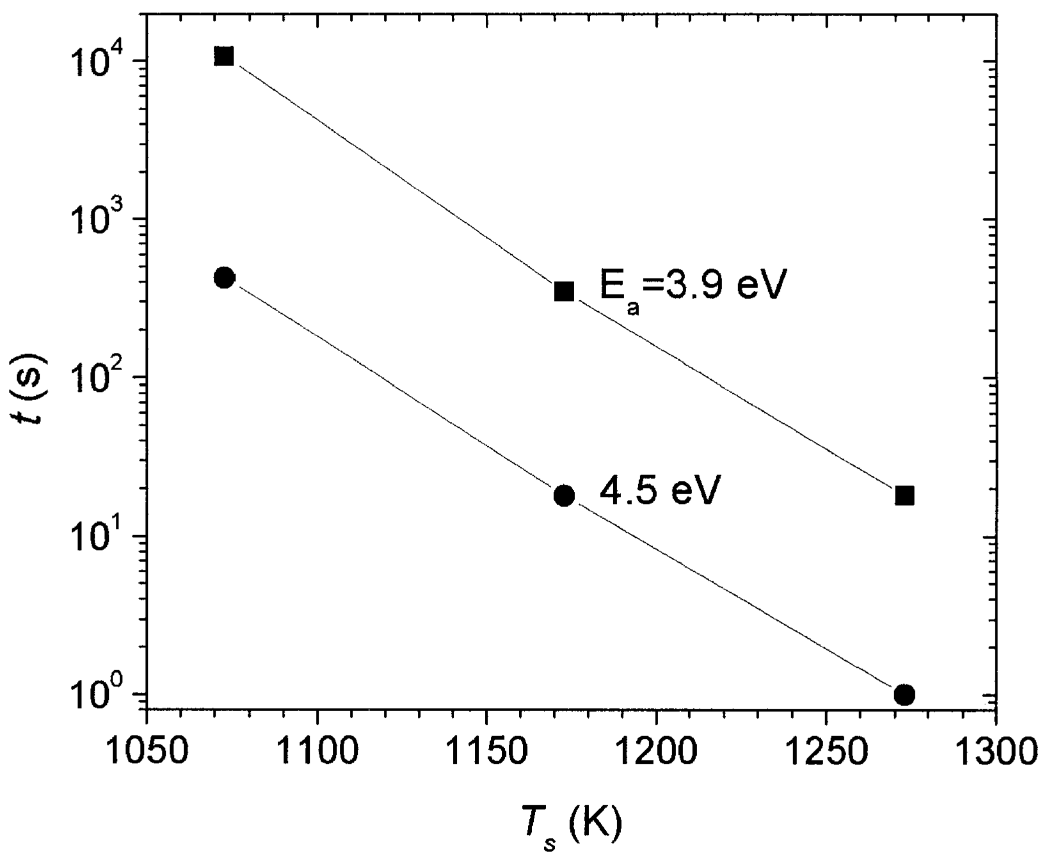

Figure 5.1 Formation time of the β-SiC layer as a function of the substrate temperature for two different hydrocarbon adsorption energies, 3.9 and 4.5 eV, under HFCVD operating conditions conductive to diamond nucleation, as listed in Table 5.1.

Reproduced with permission of the copyright owner. Further reproduction prohibited without permission.

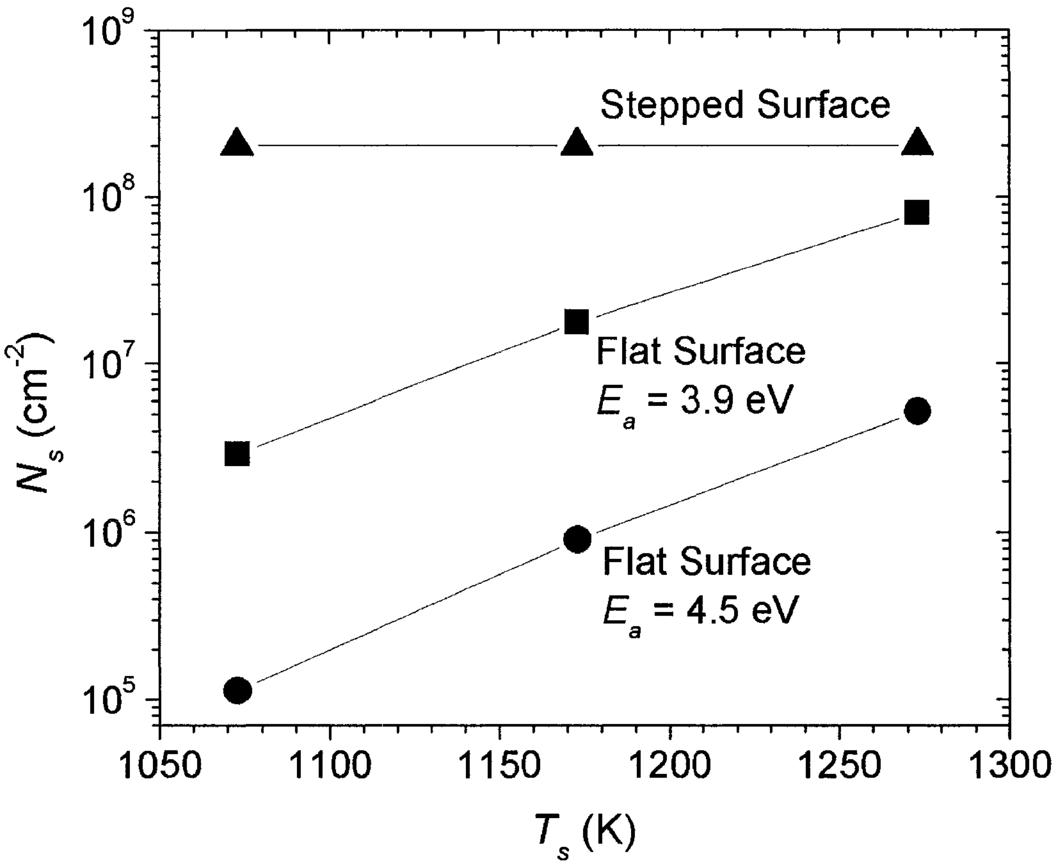

Figure 5.2 Saturated nucleation density as a function of the substrate temperature for three different pretreated Si substrates, including stepped β-SiC surface with W_t = 1 μm, flat β-SiC surface with E_a = 4.5 eV, and flat β-SiC surface with E_a = 3.9 eV.

Reproduced with permission of the copyright owner. Further reproduction prohibited without permission.

value of N_s reaches a maximum at 2.0×10^8 cm^{-2} when W_t = 1 μm, and this does not change with further decreases in W_t because diamond nucleation may be limited by the nucleation kinetics rather than the surface diffusion when W_t < 1 μm. The predicted values for V_{10} as a function of T_s are shown in Figure 5.3 for X_{CH_4} between 0.005 and 0.02. The dependence of V_{10} on T_s is qualitatively similar for all three values of X_{CH_4}, such that V_{10} increases with T_s, reaching a maximum at the highest T_s value of 1273 K. Figure 5.3 demonstrates that, except at T_s = 1273 K, the value of V_{10} is usually higher when more atomic hydrogen is produced because this species leads to CH_3 formation, and a high enough flux of atomic hydrogen on the substrate prepares sites for CH_3 adsorption. The values of X_H calculated by the filament-poisoning model are 0.1, 0.06, and 0.03 for the X_{CH_4} values of 0.004, 0.01, and 0.02, respectively.

The morphology evolution model is used to capture the dependence of the diamond film characteristics—mean surface roughness, average peak-to-valley height, grain size ratio <10>/<11>, and average grain size—on different pretreated substrates under operating conditions conducive to diamond nucleation. The calculations are performed at T_s = 1073 K and X_{CH_4} = 0.02 for two different E_a values of 3.9 and 4.5 eV. The values of α_{2D} and N_s determined at those growth conditions are summarized in Table 5.2. When different β-SiC layers are compared, diamond grown on a stepped β-SiC layer has largely {10} faces than that on a flat β-SiC layer because the stepped layer leads to a high nucleation density. Further, when the textures for two probable adsorption energies of hydrocarbon precursors on the flat β-SiC surface are compared, the lower E_a = 3.9 eV value leads to the formation of a large fraction of {10} faces with a relatively smaller film thickness

Reproduced with permission of the copyright owner. Further reproduction prohibited without permission.

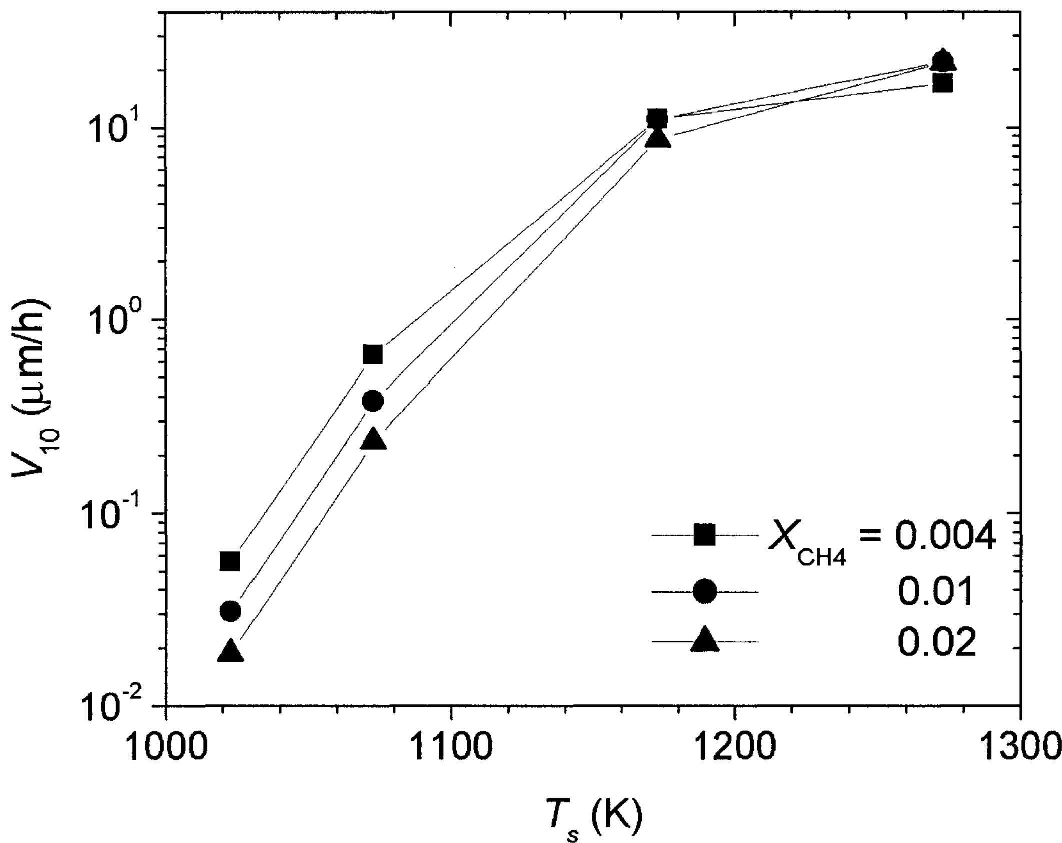

Figure 5.3 Growth velocity of {10} face, V_{10}, determined for different substrate temperatures and inlet gas compositions under the operating conditions corresponding to Figure 5.1.

Reproduced with permission of the copyright owner. Further reproduction prohibited without permission.

Table 5.2 The calculated maximum mean surface roughness R_m and film thickness L_m corresponding to the saturated nucleation density N_s and growth-rate parameter α_{2D}, which are predicted by applying different combinations of the growth conditions.

	Growth conditions				N_s (cm^{-2})	α_{2D}	R_m (μm)	L_m (μm)
β-SiC surface	W_t (μm)	E_a (eV)	T_s (K)	X_{CH_4}				
(*a*) Stepped	1.0		1073	0.02	2×10^8	1.95	3.3	400
(*b*) Flat		3.9	1073	0.02	2.9×10^6	1.95	27	3000
(*c*) Flat		4.5	1073	0.02	1.1×10^5	1.95	119	9000
(*d*) Flat		3.9	1273	0.02	8×10^7	1.8		

than that for 4.5 eV, since smaller adsorption energies lead to larger nucleation densities. Calculations are also carried out to investigate the dependence of the texture on the growth-rate parameter α_{2D}, which is dependent on substrate temperature. The growth-rate parameter decreases from 1.95 to 1.8 as the substrate temperature is increased from 1073 to 1273 K for fixed X_{CH_4} = 0.02, and the lower of α_{2D} value results in a transition of the film growth axis from <10> to <11>. Upon a further decrease in α_{2D}, <11>-textured diamond with largely {11} faces are formed.

Figure 5.4 illustrates the dependence of the mean surface roughness on film thickness, the saturated nucleation density, and the growth-rate parameter. The saturated nucleation density and the growth-rate parameter are predicted by applying different combinations of the growth conditions, as listed in Table 5.2. When the mean surface roughnesses for cases (*a*), (*b*), and (*c*) are compared to investigate the effects of different pretreated substrates on the mean surface roughness, it is readily seen that the increase in the saturated nucleation density due to substrate pretreatment significantly reduces the mean surface roughness of deposited diamond films. The mean surface roughness increases as film thickness increases and eventually asymptotes to a maximum value. The

Reproduced with permission of the copyright owner. Further reproduction prohibited without permission.

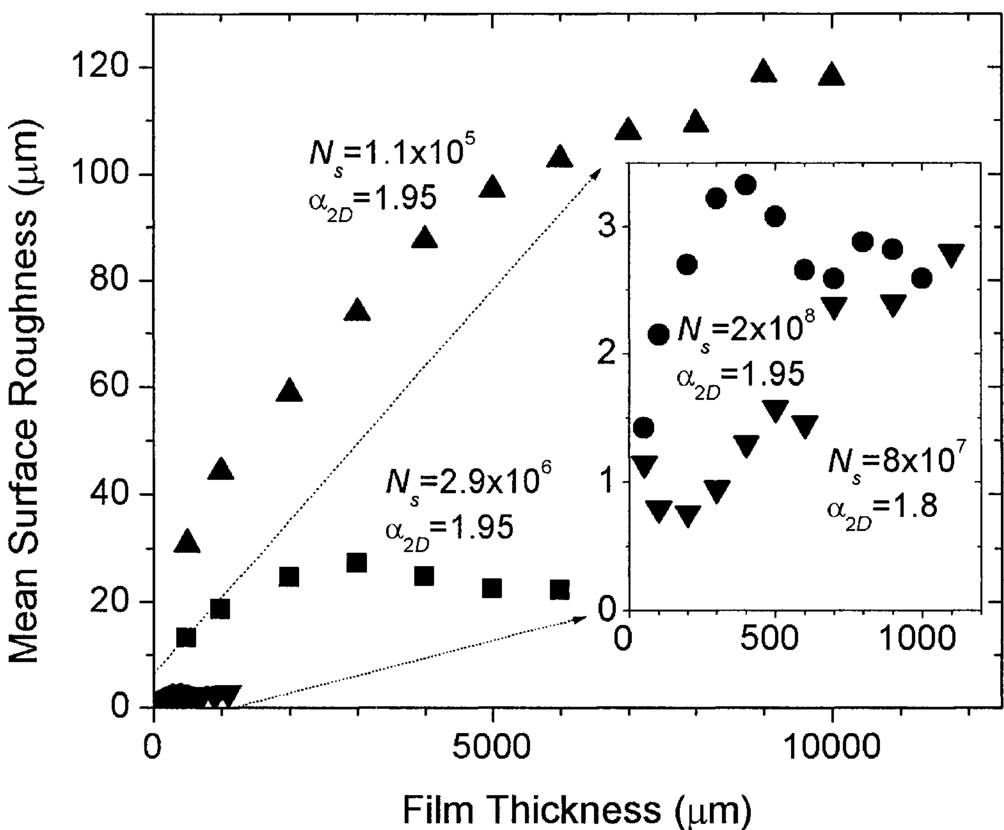

Figure 5.4 Mean surface roughness as a function of the film thickness for different saturated nucleation densities and growth rate parameters listed in Table 5.2.

Reproduced with permission of the copyright owner. Further reproduction prohibited without permission.

calculated values of the maximum mean surface roughness, R_m, corresponding to the saturated nucleation densities and the growth-rate parameters are also listed in Table 5.2. The film thickness, L_m, needed to achieve the maximum mean surface roughness decreases as the saturated nucleation density increases, indicating that a higher nucleation density will yield a better surface morphology at a relatively small film thickness. Nucleation densities on the order of 10^5 to 10^8 cm^{-2} are, however, not sufficient for producing very thin, smooth diamond films that can be used in field applications. As the saturated nucleation density is varied from 2.0×10^8 to 1.1×10^5 cm^{-2}, the film thickness needed to reach the maximum mean roughness increases approximately 23 fold.

Similar tendencies for the dependence of the surface roughness on the saturated nucleation density as a function of film thickness are expected for the average peak-to-valley height, as demonstrated in Figure 5.5. However, the calculated maximum values of the average peak-to-valley height are considerably greater than those of the mean surface roughness; for cases (*a*), (*b*), and (*c*) these are 8.7, 61.7, and 228 μm at film thicknesses of 500, 3000, and 9000 μm, respectively.

To illustrate the dependence of the surface roughness on substrate temperature, a set of calculations are performed for two different substrate temperature values, 1073 and 1273 K. When the substrate temperature is increased from 1073 to 1273 K at a fixed value of $X_{CH_4} = 0.02$, the value of α_{2D} decreases from 1.95 to 1.8, while the saturated nucleation density increases from 2.9×10^6 to 8×10^7 cm^{-2}, as listed in Table 5.2. Diamond films having{10}-faces tilted to <11> develop for T_s = 1273 K and α_{2D} = 1.8. The mean surface roughness and average peak-to-valley height of diamond films grown at T_s = 1273 K are much smaller than those grown at 1073 K, and the values are

Reproduced with permission of the copyright owner. Further reproduction prohibited without permission.

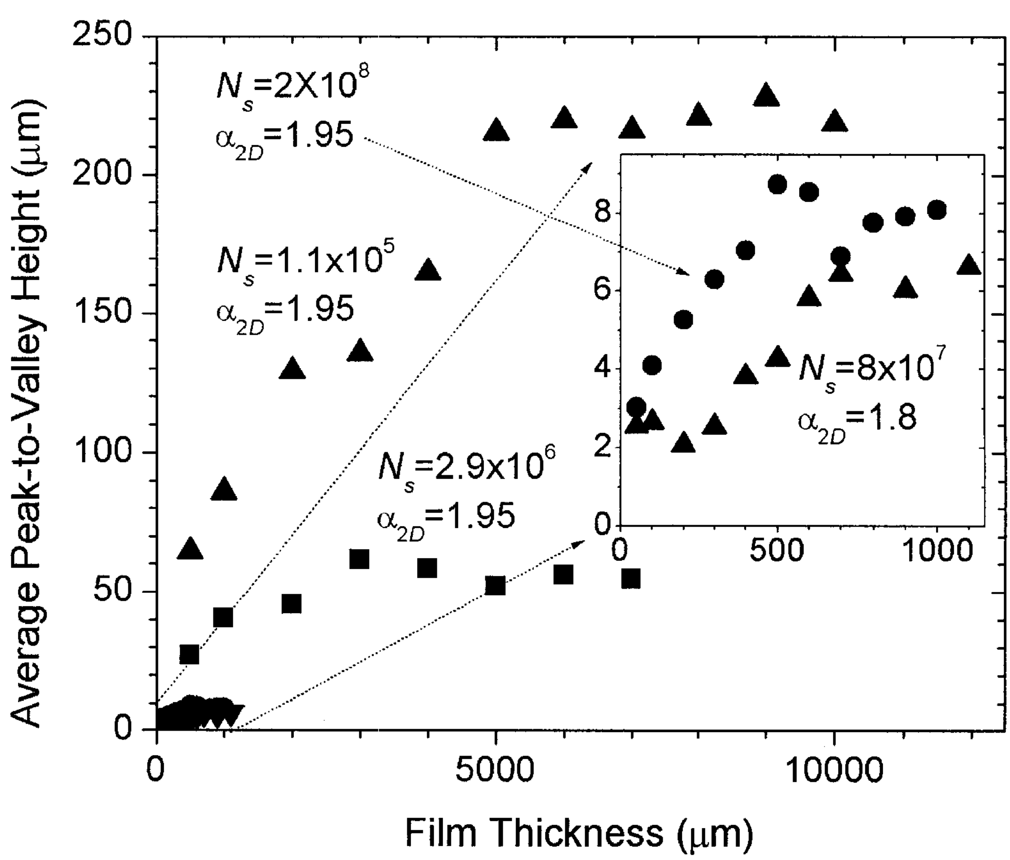

Figure 5.5 Average peak-to-valley height as a function of film thickness for the growth conditions corresponding to Figure 5.4.

Reproduced with permission of the copyright owner. Further reproduction prohibited without permission.

comparable to those of diamond films grown on stepped β-SiC layers with T_s = 1073 K, as shown in Figures 5.4 and 5.5. However, the mean surface roughness and the average peak-to-valley height are observed to monotonically increase with increases in film thickness, and do not reach a maximum within the range of film thickness considered in the present calculations.

The dependence of the grain size ratio <10>/<11> and the average grain size on the saturated nucleation density are also quantitatively investigated as a function of film thickness, and these results are presented in Figures 5.6 and 5.7. Figure 5.6 demonstrates that the grain size ratio <10>/<11> increases by increasing either the saturated nucleation density or the film thickness at a fixed α_{2D} = 1.95. The calculated grain size ratio <10>/<11> corresponding to a film thickness of 1000 μm is 1.63 for N_s = 2.0×10^8 cm^{-2}, while the ratio corresponding to the same film thickness decreases to 0.48 and 0.2 for nucleation densities of 2.9×10^6 and 1.1×10^5 cm^{-2}, respectively. When the films are thin, all of the curves in Figure 5.6 have steep slopes and the ratio varies linearly with film thickness; the slope increases as the nucleation density is increased. The reason for these steep increases is that, for α_{2D} = 1.95, the disappearance rate of <11>-textured grains is high for thin films because an increasing fraction of <11>-textured grains are overgrown by fast growing <10>-textured grains. However, for thick films, the disappearance rate gradually decreases because the degree of the <10> texture improves with film thickness.

Figure 5.7 shows that the average grain size is also strongly affected by the nucleation density and film thickness, and a smaller nucleation density leads to a larger grain at a given film thickness. At 1000 μm, the calculated average grain size approaches 240 μm for a nucleation density of 1.1×10^5 cm^{-2}, while the average size is 35 μm for a

Reproduced with permission of the copyright owner. Further reproduction prohibited without permission.

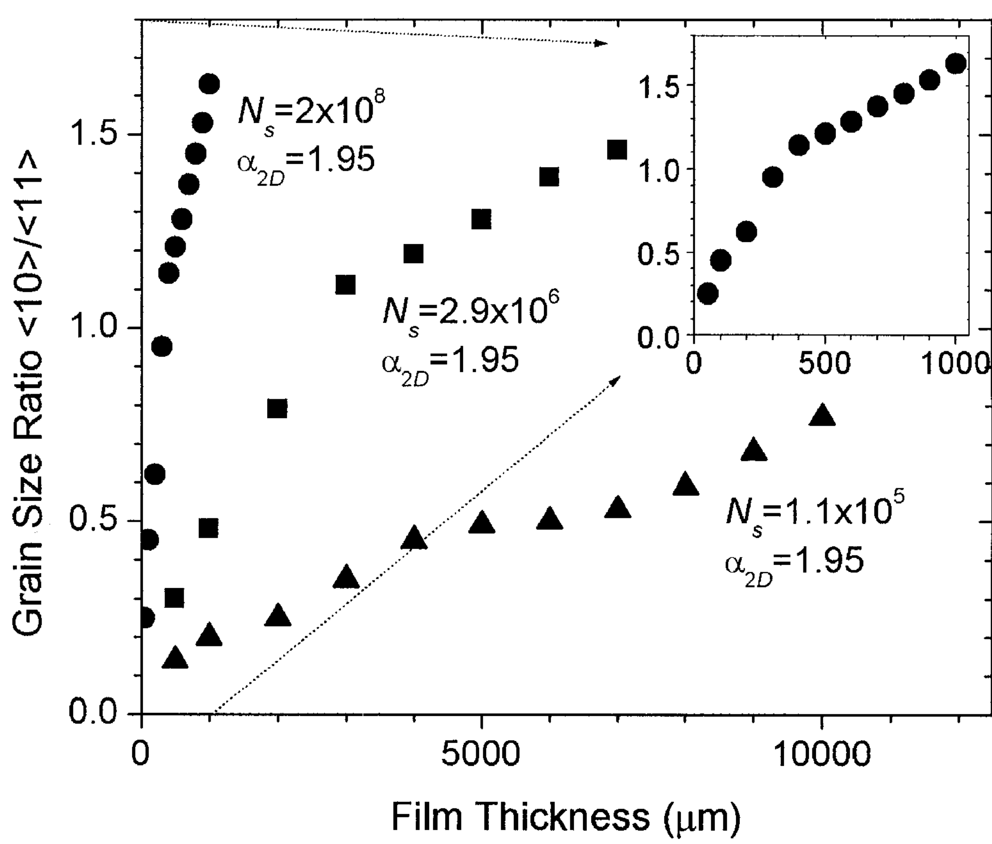

Figure 5.6 Relative grain size ratio <10>/<11> as a function of film thickness for the growth conditions corresponding to Figure 5.4.

Reproduced with permission of the copyright owner. Further reproduction prohibited without permission.

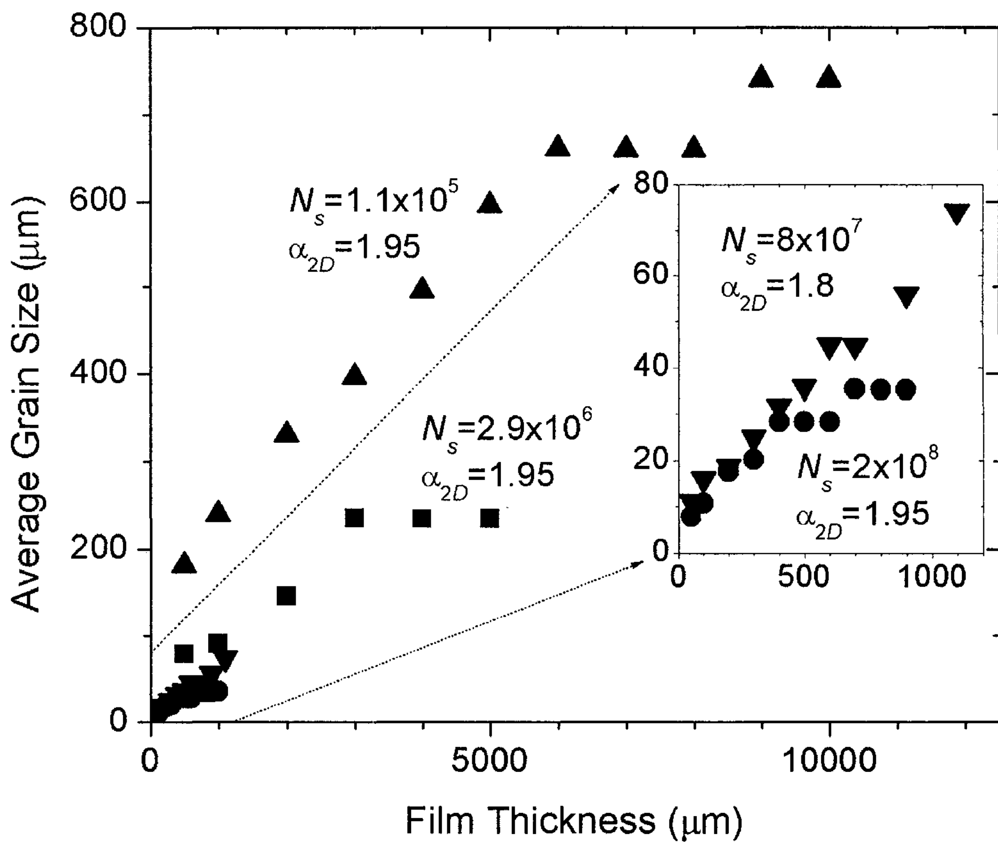

Figure 5.7 Average grain size as a function of film thickness for the growth conditions corresponding to Figure 5.4.

Reproduced with permission of the copyright owner. Further reproduction prohibited without permission.

nucleation density of 2.0×10^{8} cm^{-2}. The average grain size increases as film thickness increases because the misorientated grains are gradually buried, and thus the number of remaining grains continuously decreases. However, the rate of increase the average grain size with film thickness significantly decreases as the film grows.

5.3.2 Continuous Film Growth Process

The processes for enhancing diamond nucleation on pretreated substrates are important steps in the deposition of high quality diamond films. However, since the quality of these films is often limited due to the inability to obtain a desired texture, a further improvement of these film properties requires an extensive investigation of the crystallographic texture and surface morphology of diamond films during the film growth stage. Calculations are performed to determine the dependence of the characteristics of films grown during the film growth stage on the α_{2D} value, as well as on the texture and morphology of diamond grown during the nucleation stage.

The value of α_{2D} is chosen from the literature [61] for different combinations of the substrate temperature and the inlet CH_4 mole fraction. For the calculations carried out in this study, two different values of T_s, 1023 and 1173 K, are used for the film growth stage with $X_{CH_4} = 0.01$. The values of α_{2D} reported in the literature are approximately 1.9 and 1.6 for 1023 and 1173 K, respectively. Further, α_{2D} decreases from 1.9 to 1.3 as X_{CH_4} is decreased from 0.01 to 0.004 at $T_s = 1023$ K.

To investigate the sensitivity of the film's texture and morphology to the terminal diamond thickness during the nucleation stage, three different thicknesses, $L_t = 1$, 10, and 50 μm, are chosen. A film of thickness L_t is grown on a flat β-SiC layer during the nucleation stage for $T_s = 1273$ K, $X_{CH_4} = 0.02$, and $E_a = 3.9$ eV. The $L_t = 1$ μm is chosen

Reproduced with permission of the copyright owner. Further reproduction prohibited without permission.

to be representative of the thickness required for the formation of a continuous film under growth conditions typical of diamond nucleation. Since the optimal values of operating conditions for continuous film growth may not be identical to those for nucleation, a much poorer-quality diamond film is grown if the operating conditions for nucleation are continually applied after the formation of a continuous film. Other two large L_t values, 10 and 50 μm, are chosen to investigate the negative effects of thick film growth during the nucleation stage on the film's final characteristics.

Figure 5.8 illustrates the mean surface roughness of films for different α_{2D} and L_t values. The predicted mean surface roughness as a function of film thickness is shown in Figures 5.8a and 5.8b for three different α_{2D} values of 1.3, 1.6, and 1.9. The dependence of the mean surface roughness on film thickness is qualitatively similar for α_{2D} = 1.9 and 1.3. Both sets of the mean surface roughness calculations exhibit a maximum, 7.7 and 10.6 μm, for α_{2D} =1.9 and 1.3, respectively, indicating that a further increase in film thickness after the maximum is necessary to attain a smoother surface. The decrease in the mean surface roughness as film thickness is increased is significant for both α_{2D} values, but as can be seen in Figure 5.8b, the film surface is smoother for α_{2D} = 1.9. Since the film has a near <10> texture for α_{2D} = 1.9, a relatively flat surface with predominantly {10} faces develops for film thicknesses larger than 900 μm, while the film surface for α_{2D} = 1.3 does not become flat until the film thickness reaches 1100 μm. In contrast, at an intermediate value of α_{2D} = 1.6, no maximum value of the mean surface roughness is reached. Although the mean surface roughness for α_{2D} = 1.6 in Figure 5.8a is smaller than that for α_{2D} = 1.9 and 1.3 at small film thicknesses, the predicted mean surface roughness increases almost linearly with increases in film thickness, and does not

Reproduced with permission of the copyright owner. Further reproduction prohibited without permission.

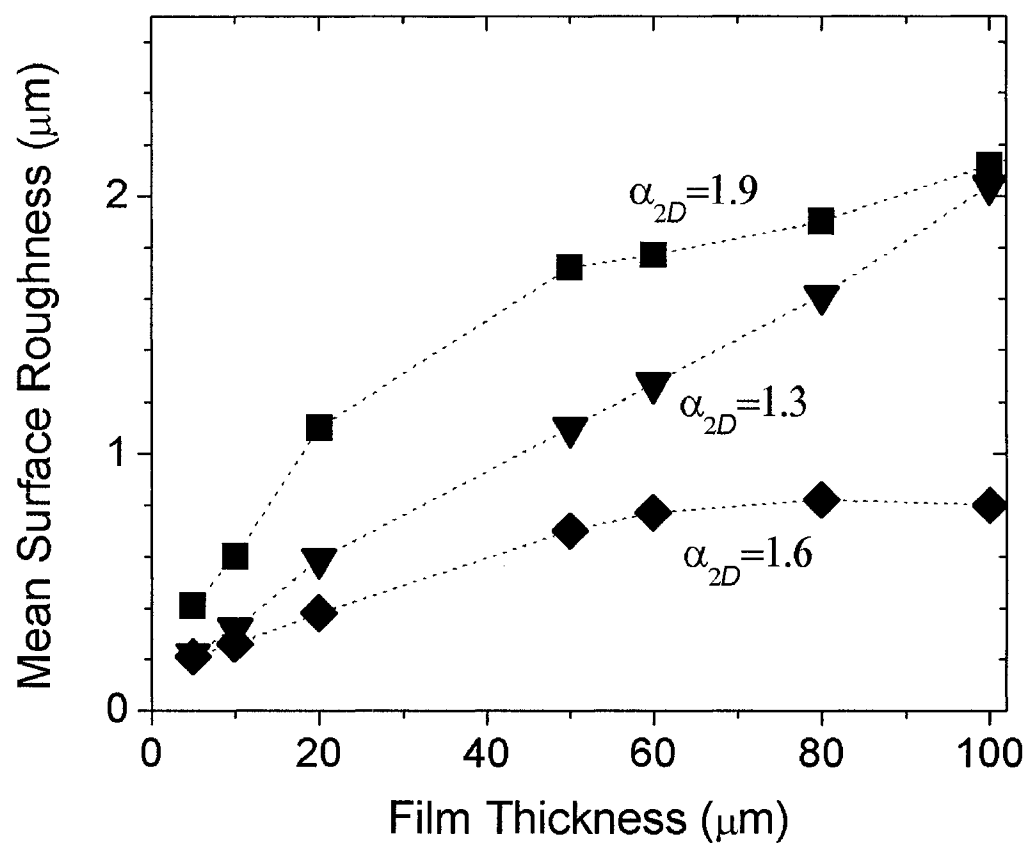

Figure 5.8a Mean surface roughness of films grown during the continuous film growth stage as a function of overall film thickness up to 100 μm. Plot show the mean surface roughness for different growth-rate parameters, α_{2D} = 1.3, 1.6, and 1.9, at a fixed L_t value of 1 μm.

Reproduced with permission of the copyright owner. Further reproduction prohibited without permission.

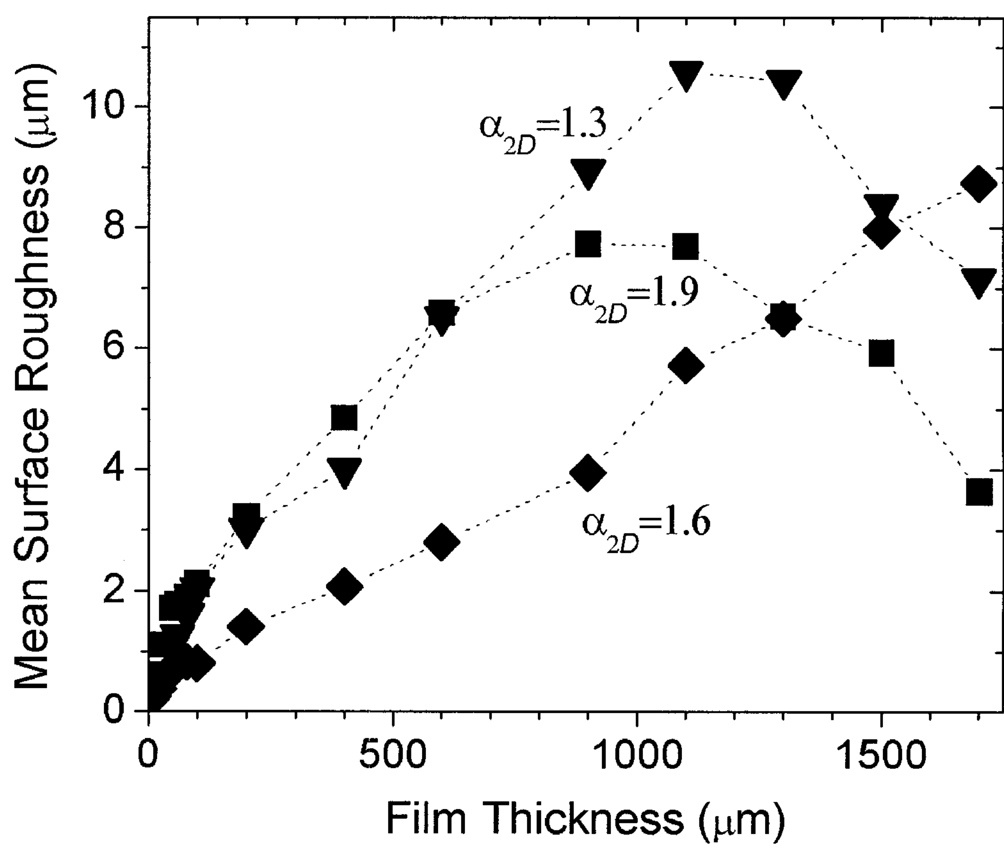

Figure 5.8b Mean surface roughness of films grown during the film growth stage as a function of overall film thickness up to 1700 μm. Plot show the mean surface roughness for different growth-rate parameters, α_{2D} = 1.3, 1.6, and 1.9, at a fixed L_t value of 1 μm.

Reproduced with permission of the copyright owner. Further reproduction prohibited without permission.

reach a maximum. Figure 5.8b shows that, since a large fraction of {11} faces is present on the film surface at large film thickness, the mean surface roughness for α_{2D} = 1.6 is larger than those for α_{2D} = 1.9 and 1.3 if the film is thicker than 1500 μm.

Another factor that is important in determining the surface morphology of films is the value of L_t. A reduction of the mean surface roughness of films can be achieved by decreasing L_t, as shown in Figures 5.8c and 5.8d. Assigning α_{2D} values of 1.8 and 1.9 for the diamond nucleation and continuous film growth stages, respectively, Figure 5.8c indicates that a small L_t value of 1 μm prevents the formation of a smooth surface morphology for thin films, while the value of L_t favors the smooth, {10}-faced surface as film thickness is increased, as shown in Figure 5.8d. The film growth for α_{2D} = 1.8 leads to a smoother surface at small film thicknesses than that for α_{2D} = 1.9 because a growing direction tilted from <10> promotes coalescence between randomly orientated grains, while a nearly {10}-faced surface is eventually present during the film growth stage for α_{2D} = 1.9. When the value of L_t is reduced from 10 to 1 μm, a significant decrease in the maximum roughness, from 12.7 to 7.7 μm, results.

The evolution of average grain size with film thickness for different α_{2D} and L_t values is illustrated in Figure 5.9. The average grain size increases monotonically with increases in film thickness, because the odds of a particular grain surviving depend on its fastest growth-orientation, which is determined by the value of α_{2D}. Figure 5.9a demonstrates that the average grain size increases with α_{2D} in the following order: α_{2D} =1.9 > 1.3 > 1.6, and further, the increase of average grain size leads to an increase in the surface roughness, as depicted schematically in Figure 5.8a. Interestingly, Figure 5.9b shows that the average grain size for α_{2D} =1.9 increases sharply as film thickness increases because

Reproduced with permission of the copyright owner. Further reproduction prohibited without permission.

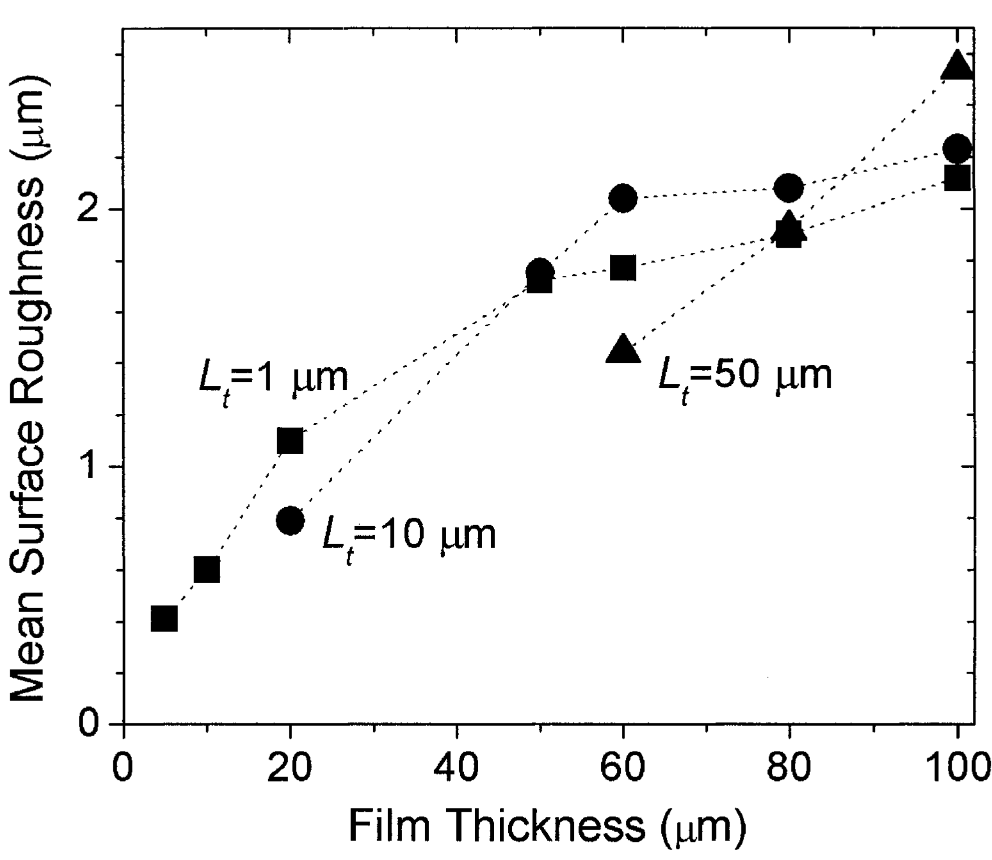

Figure 5.8c Mean surface roughness of films grown during the film growth stage as a function of overall film thickness up to 100 μm. Plot display the mean surface roughness for different underlying diamond film thicknesses, L_t = 1, 10, and 50 μm, at a fixed α_{2D} value of 1.9.

Reproduced with permission of the copyright owner. Further reproduction prohibited without permission.

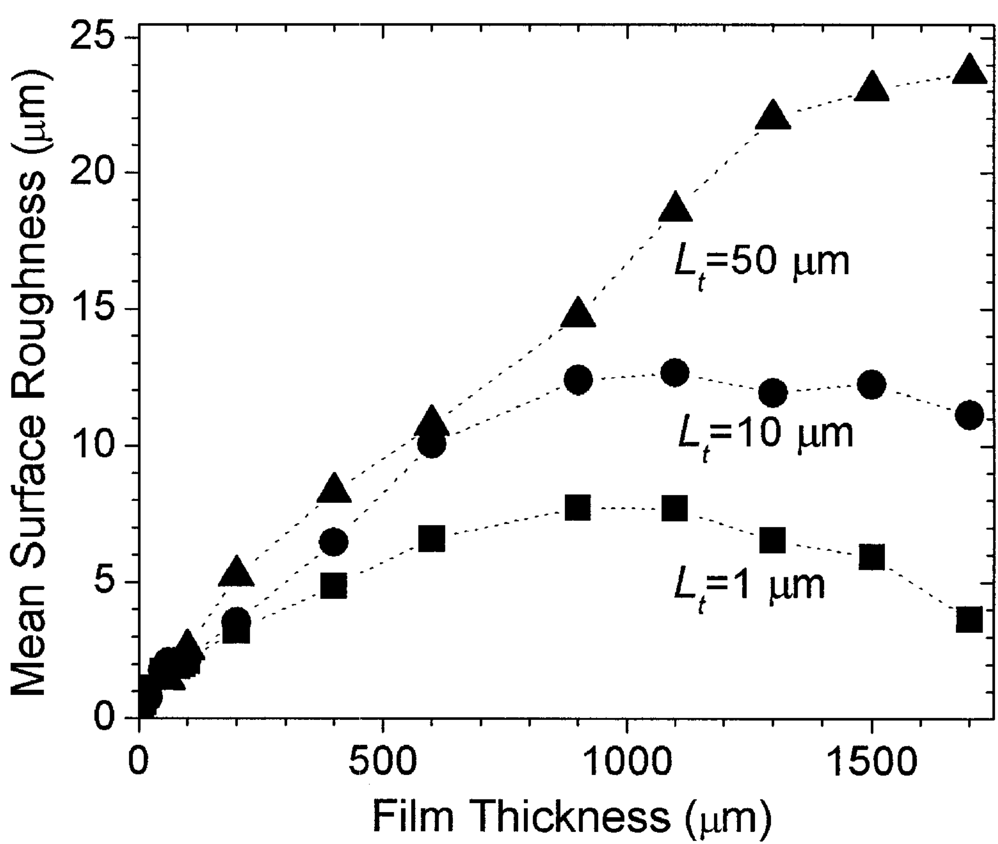

Figure 5.8d Mean surface roughness of films grown during the film growth stage as a function of overall film thickness up to 1700 μm. Plot display the mean surface roughness for different underlying diamond film thicknesses, L_t = 1, 10, and 50 μm, at a fixed α_{2D} value of 1.9.

Reproduced with permission of the copyright owner. Further reproduction prohibited without permission.

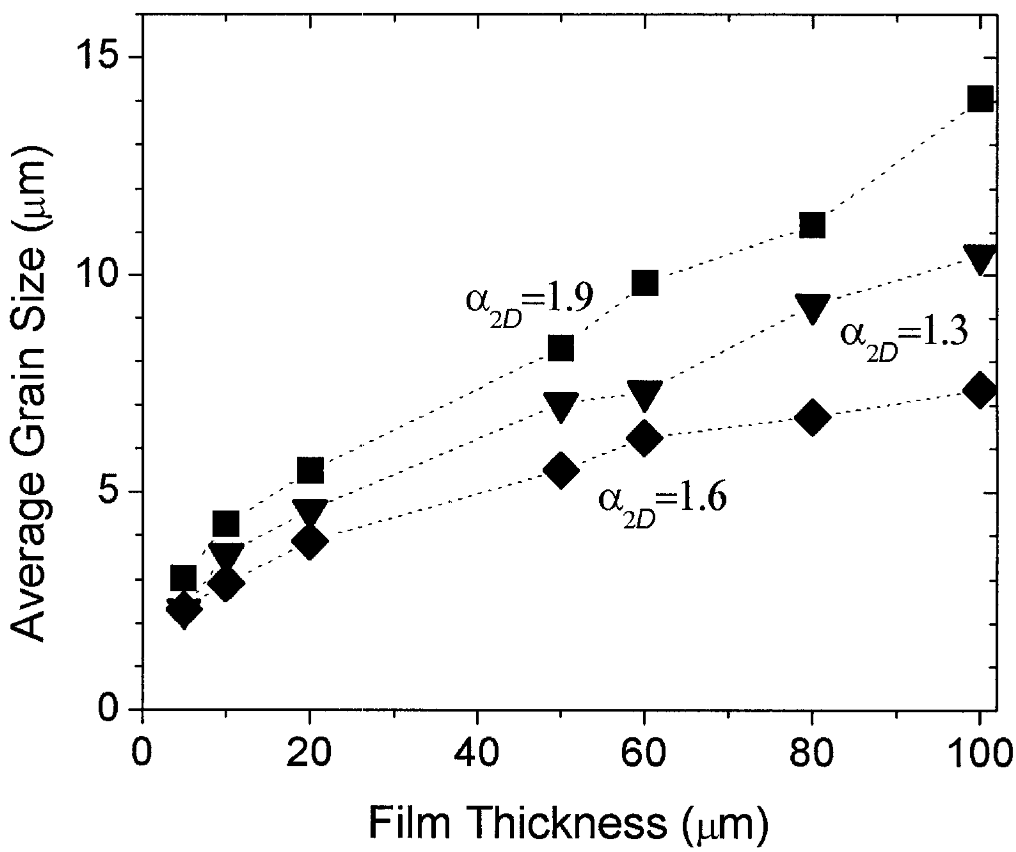

Figure 5.9a Average grain size of films grown during the film growth stage as function of overall film thickness up to 100 μm. Plot show the mean surface roughness for different growth-rate parameters, α_{2D} = 1.3, 1.6, and 1.9, at a fixed L_t value of 1 μm.

Reproduced with permission of the copyright owner. Further reproduction prohibited without permission.

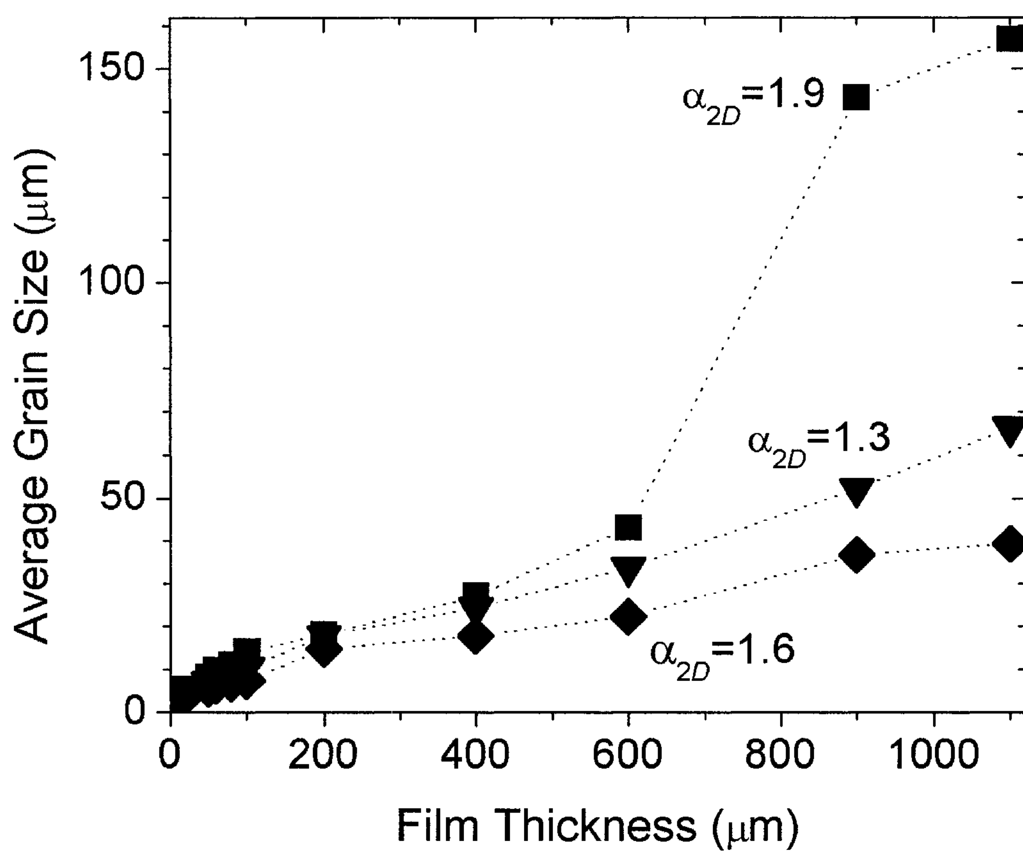

Figure 5.9b Average grain size of films grown during the film growth stage as function of overall film thickness up to 1200 μm. Plot show the mean surface roughness for different growth-rate parameters, α_{2D} = 1.3, 1.6, and 1.9, at a fixed L_t value of 1 μm.

Reproduced with permission of the copyright owner. Further reproduction prohibited without permission.

misorientated grains are eventually buried as growth proceeds, and the rate of increase in grain size, however, decreases significantly once the mean surface roughness reaches a maximum at a film thickness of 900 μm. The grain sizes for two other α_{2D} values of 1.6 and 1.3 increase almost linearly with increases in film thickness, since the maximum mean surface roughness is not reached for the film thickness used in the calculations. Figures 5.9c and 5.9d illustrate the dependence of average grain size on L_t. A smaller L_t value translates to a larger average grain size as film thickness is increased, and this leads to the rapid development of large {10} faced grains for $\alpha_{2D} = 1.9$.

5.4 Conclusion

A model based on the morphology evolution is employed to study the crystallographic texture and surface morphology of diamond films deposited on pretreated Si substrates, including flat and stepped β-SiC layers, in HFCVD systems. Diamond film growth via a two-stage HFCVD process comprised of (1) diamond nucleation and (2) continuous film growth is examined. For the diamond nucleation stage, the effects of substrate pretreatment and the growth rate parameter on the diamond film characteristics—surface roughness, film texture and orientation, and grain size—are investigated under operating conditions conducive to diamond nucleation. Further, for the film growth stage, the crystallographic texture and surface morphology of films are determined for different α_{2D} and L_t values, and the growth conditions are optimized to achieve highly <10>-textured films with smooth, {10}-faced surfaces.

It is predicted that a β-SiC layer readily forms on the Si substrate surface during the initial stages of diamond nucleation as a result of substrate carbonization. When the sat-

Reproduced with permission of the copyright owner. Further reproduction prohibited without permission.

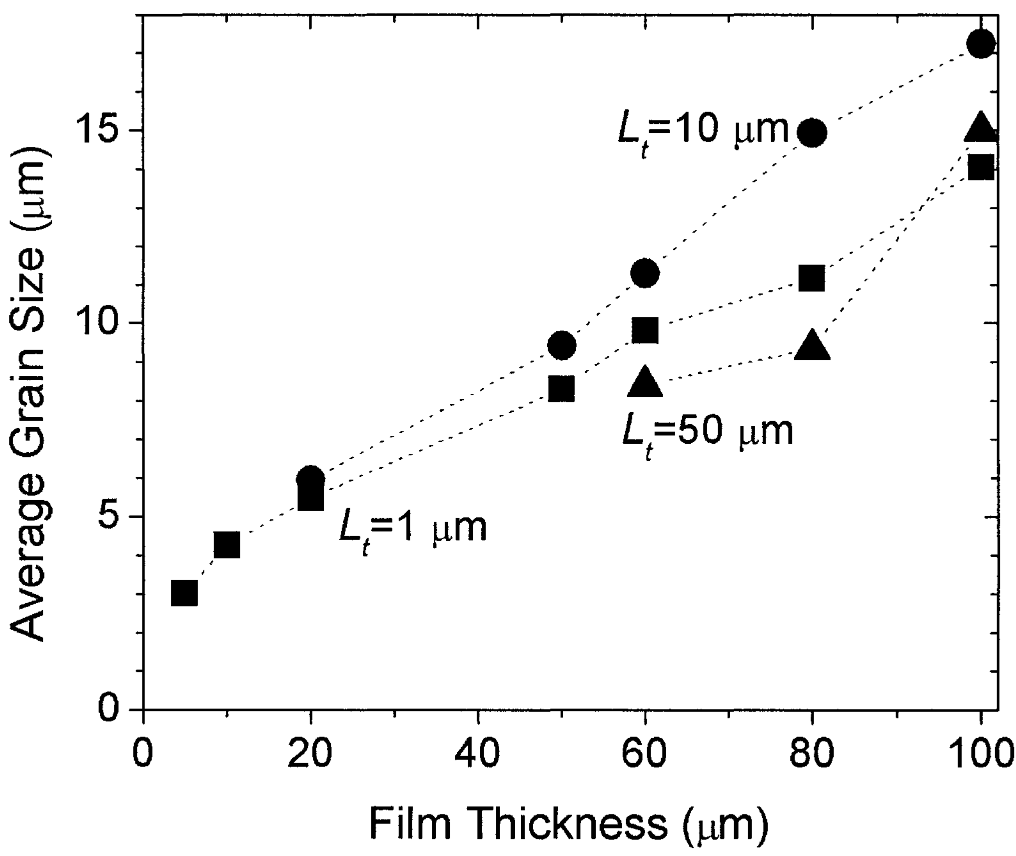

Figure 5.9c Average grain size of films grown during the film growth stage as function of overall film thickness up to 100 μm. Plot display the mean surface roughness for different underlying diamond film thicknesses, L_t = 1, 10, and 50 μm, at a fixed α_{2D} value of 1.9.

Reproduced with permission of the copyright owner. Further reproduction prohibited without permission.

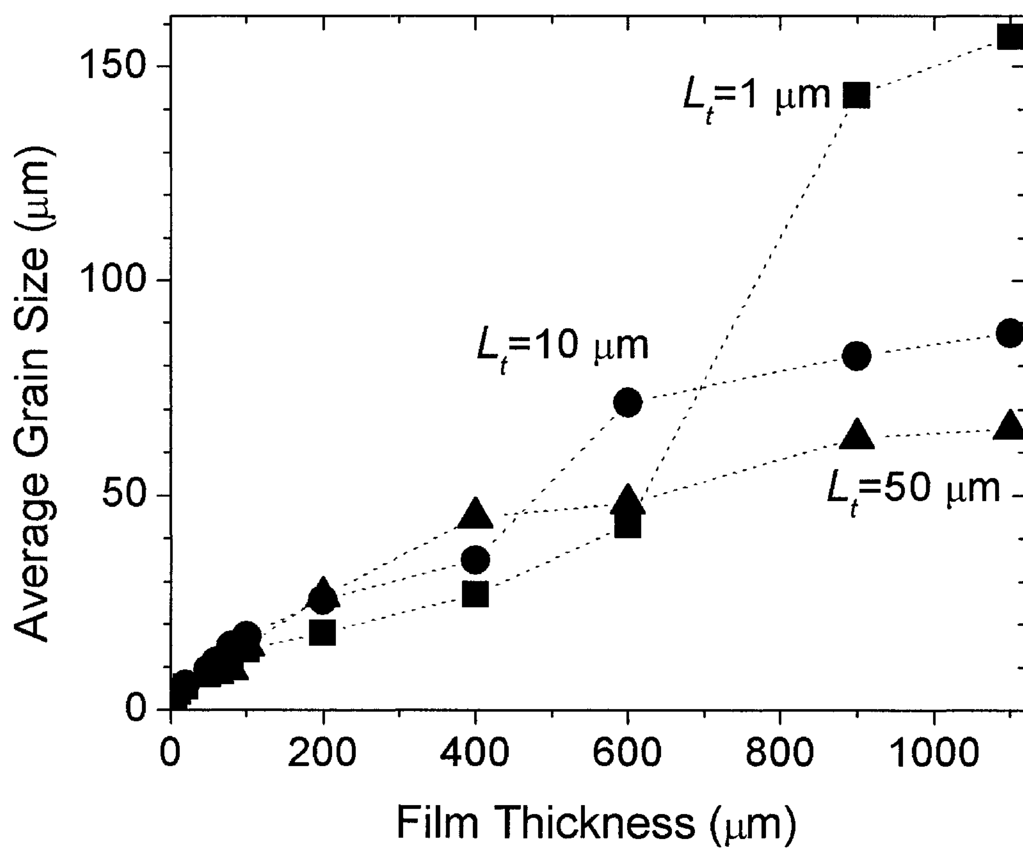

Figure 5.9d Average grain size of films grown during the film growth stage as function of overall film thickness up to 1200 μm. Plot display the mean surface roughness for different underlying diamond film thicknesses, L_t = 1, 10, and 50 μm, at a fixed α_{2D} value of 1.9.

Reproduced with permission of the copyright owner. Further reproduction prohibited without permission.

urated nucleation density is calculated for diamond nucleation on a flat β-SiC layer, it is seem that the density increases with an increase in the substrate temperature and a decrease in the adsorption energy for substrate temperatures between 1073 and 1273 K and adsorption energies of 3.9 and 4.5 eV. The nucleation density is predicted to be 8×10^{7} cm^{-2} at a 1273 K substrate temperature and a 3.9 eV adsorption energy. It is further seen that the nucleation density reaches a maximum of 2×10^{8} cm^{-2} when diamond nucleates on a stepped β-SiC layer having a 1 μm terrace width. However, decreasing the terrace width below 1 μm has negligible impact on the saturated nucleation density because the nucleation process may be dominated by nucleation kinetics rather than surface diffusion when the terrace width is small.

When diamond film characteristics are determined for different pretreated Si substrates and growth rate parameters under operating conditions conducive to diamond nucleation, results indicate that the increase in the saturated nucleation density due to substrate pretreatment reduces the mean surface roughness and the average peak-to-valley height. For α_{2D} = 1.95, the surface roughness values increase with increases in film thickness, eventually asymptoting to maximum values. It is further seen that, as a higher substrate temperature leads to a higher saturated nucleation density and a lower α_{2D} value for the flat β-SiC layer, the mean surface roughness and the average peak-to-valley height are initially comparable to those calculated for the stepped β-SiC layer having a 1 μm terrace width. However, the values increase monotonically without bound with as film thickness increases. The grain size ratio <10>/<11> increases with increases in the saturated nucleation density and film thickness, and the average grain size increases with decreases in the saturated nucleation density at a given film thickness. Further, while the

Reproduced with permission of the copyright owner. Further reproduction prohibited without permission.

dependence of film characteristics on nucleation densities between 1.1×10^5 and 2×10^8 cm^{-2} are discussed in the present work, insights gained from this study can be readily applied to other systems, for example, diamond nucleation on scratched or biased substrates in which the nucleation densities are on the order of 10^{11} cm^{-2} (or higher).

During the film growth stage, results indicate that the dependence of the mean surface roughness of films on both the α_{2D} and L_t is significant. The substantial drop in the mean surface roughness with increasing film thickness once a maximum is reached for α_{2D} = 1.3 and 1.9. The calculated mean surface roughness for α_{2D} = 1.6, however, increases monotonically as film thickness is increased, and does not reach a maximum. Further, it is seen that, as L_t is decreased, the film surfaces become smoother for a given final thickness. The maximum rough-ness drops significantly as L_t is decreased. When the average grain size is calculated for different α_{2D} and L_t values large grain size as well as rapid development of {10} faces, are predicted for either α_{2D} = 1.9 or L_t = 1 μm.

Reproduced with permission of the copyright owner. Further reproduction prohibited without permission.

5.5 References

1. B.R. Stoner, B.E. Williams, S.D. Wolter, K. Nishimura, and G.T. Glass, J. Mater. Res. **7**, 257 (1992).

2. S. Barrat, P. Pigeat, and E. BauerGrosse, Diamond Relat. Mater. **5**, 276 (1996).

3. Y. Von Kaenel, J. Stiegler, E. Blank, O. Chauvet, C.H. Hellwig, and K. Plamann, Phys. Stat. Sol. A **154**, 219 (1996).

4. D. Michau, B. Tanguy, G. Demazeau, M. Couzi, and R. Cavagnat, Diamond. Relat. Mater. **2**, 19 (1993).

5. G. Papovici and M.A. Prelas, Phys. Stat. Sol. A **132**, 233 (1992).

6. B. Lux and R. Haubner, in Diamond and Diamond-like Films and Coatings, edited by R.F. Clausing, L.L. Horton, J.C. Angus, and P. Koidl (Plenum Press, New York, 1991), pp. 579.

7. D.N. Belton, S.J. Harris, S.J. Schmieg, A.M. Weiner, and T.A. Perry, Appl. Phys. Lett. **54**, 416 (1989).

8. R. Meilunas, M.S. Wong, K.C. Sheng, R.P.H. Chang, and R.P. VanDuyne, Appl. Phys. Lett. **54**, 2204 (1989).

9. B.E. Williams and J.T. Glass, J. Mater. Res. **4**, 373 (1989).

10. B.E. Williams, J.T. Glass, R.F. Davis, and K. Kobashi, J. Crystal Growth **99**, 1168 (1990).

11. B.R. Stoner, G.H.M. Ma, S.D. Wolter, and J.T. Glass, Phys. Rev. B **45**, 11067 (1992).

12. N. Jiang, B.W. Sun, Z. Zhang, and Z. Lin, J. Mater. Res. **9**, 2695 (1994).

Reproduced with permission of the copyright owner. Further reproduction prohibited without permission.

13. Z. Sun, Y. Sun, X. Wang, and Z. Zheng, Mater. Sci. Eng. B **34**, L13 (1995).

14. G. Jubber and D.K. Milne, Phys. Stat. Sol. A **154**, 185 (1996).

15. T. Hartnett, R. Miller, D. Mantanari, C. Willingham, and R. Tustison, J. Vac. Sci. Technol. A **8**, 2129 (1990).

16. K.V. Ravi, C.A. Koch, H.S. Hu, and A. Joshi, J. Mater. Res. **5**, 2356 (1990).

17. Z. Li, L. Wang, T. Suzuki, A. Argoitia, P. Pirouz, and J. Angus, J. Appl. Phys. **73**, 711 (1993).

18. H. Itoh, T. Osaki, H. Iwahara, and H. Sakamoto, J. Mater. Res. **5**, 2367 (1990).

19. G.F. Zhang, X. Zhang, and Z.T. Liu, J. Crystal Growth **133**, 117 (1993).

20. S.D. Wolter, B.R. Stoner, J.T. Glass, P.J. Ellis, D.S. Buhaenko, C.E. Jenkins, and P. Southworth, Appl. Phys. Lett. **62**, 1215 (1993).

21. T. Hartnett, Master Thesis, Penn. State Univ. (1988).

22. J.C. Arnault, S. Pecoraro, J. Werckmann, F. Le Normand, N. Motta, and R. Polini, Diamond Relat. Mater. **10**, 1612 (2001).

23. A. Köpf, B. Lux, and R. Haubner, New Diamond and Frontier Carbon Technol. **11**, 11 (2001).

24. R. Polini, J. Appl. Phys. **72**, 2517 (1992).

25. S. Haq, J.A. Savage, and D.L. Tunnicliffe, in Applications of diamond films and related materials, edited by Y. Tzeng, M. Yoshikawa, M. Murakawa, and A. Feldman (Elsevier Science Publishers, Amsterdam, 1991), pp. 405.

26. Y. Hayashi, W. Drawl, and R. Messier, Jpn. J. Appl. Phys. **69**, 6400 (1991).

27. J.W. Kim, Y.J. Baik, and K.Y. Eun, in Applications of diamond films and

Reproduced with permission of the copyright owner. Further reproduction prohibited without permission.

related materials, edited by Y. Tzeng, M. Yoshikawa, M. Murakawa, and A. Feldman (Elsevier Science Publishers, Amsterdam, 1991), pp.399.

28. A. van der Drift, Philips Res. Repts. **22**, 267 (1967).
29. C. Wild, N. Herres, and P. Koidl, J. Appl. Phys. **68**, 973 (1990).
30. C. Wild, P. Koidl, W. Műller-Sebert, H. Walcher, R. Kohl, N. Herres, R. Locher, R. Samlenski, and R. Brenn, Diamond Relat. Mater. **2**, 158 (1993).
31. B.R. Stoner, S.R. Sahaida, J.P. Bade, P. Southworth, and P.J. Ellis, J. Mater. Res. **8**, 1334 (1993).
32. X. Jiang and C.P. Klages, Phys. Stat. Sol. A **154**, 175 (1996).
33. B. Lewis and D.S. Campbell, J. Vac. Sci. Technol. **4**, 209 (1967).
34. V.N.E. Robinson and J.L. Robins, Thin Solid Films **20**, 155 (1974).
35. J.A. Venables, G.D.T. Spiller, and M. Hanbűcken, Rep. Prog. Phys. **47**, 399 (1984).
36. M. Ohring, The materials science of thin films, (Academic Press, Harcourt Brace Jovanovich Pub., Boston, MA, 1992).
37. J. Yun and D.S. dandy, submitted to Thin Solid Films (2003).
38. F.G. Celii and J.E. Bulter, Ann. Rev. Phys. Chem. **42**, 643 (1991).
39. K.E. Spear, J. Amer. Ceram. Soc. **72**, 171 (1989).
40. J. Yun and D.S. Dandy, Diamond Relat. Mater. **9**, 439 (2000).
41. W. Zhu, R. Messier, and A.R. Badzian, in proceedings of the First International Symposium on Diamond and Diamond-like Films, edited by J.P. Dismukes (The Electrochemical Society, Pittsburgh, PA, 1988), pp. 3.
42. W.A. Yarbrough and R. Messier, Science **247**, 688 (1990).

Reproduced with permission of the copyright owner. Further reproduction prohibited without permission.

43. S. Khatami and J. Asmussen, Proceedings of the 1996 IEEE International Conference on Plasma Science, 1996, pp. 139.

44. T. Bacci, E. Borchi, M. Bruzzi, M. Santoro, and S. Sciortino, Mat. Sci. Eng. B-Solid **48**, 268 (1997).

45. S. Sakiyama, O. Fukumasa, T. Murakami, and T. Kobayashi, Jpn. J. Appl. Phys. **1-36**, 5003 (1997).

46. I. Garcia and A.J. Vázquez, Thin Solid Films **325**, 99 (1998).

47. B.V. Spitsyn and L.L. Bouilov, in Diamond and Diamond-like Materials Synthesis, Spring MRS Meeting Extended Abstracts, Symposium D, edited by G.H. Johnson, A.R. Badzian, and M.N. Geis (MRS, Pittsburgh, PA, 1988), pp. 3.

48. B.V. Spitzyn, L.L. Bouilov, and B.V. Derjaguin, Prog. Crystal Growth Charact. **17**, 79 (1988).

49. S. Matsumoto, Y. Sato, M. Tsutsumi, and N. Setaka, J. Mater. Sci. **17**, 3106 (1982).

50. K. Kobashi, K. Nishimura, Y. Kawate, and T. Horuchi, Phys. Rev. B **38**, 4067 (1988).

51. K. Kobashi, K. Nishimura, K. Miyata, K. Kumagai, and A. Nakaui, J. Mater. Res. **5**, 2469 (1990).

52. Z.P. Lu, J. Heberlein, and E. Pfender, Plasma Chem. Plasma Proc. **12**, 35 (1992).

53. M.E. Coltrin, R.J. Kee, G.H. Evans, E. Meeks, F.H. Rupley, and J.F. Grear, Report No. SAND 91-8003 (1991).

Reproduced with permission of the copyright owner. Further reproduction prohibited without permission.

54. R.J. Kee, F.M. Rupley, and J.A. Miller, Report No. SAND 89-8009B (1993).

55. M.E. Coltrin, R.J. Kee, and F.M. Rupley, Report No. SAND 90-8003B (1991).

56. R.J. Kee, G. Dixon-Lewis, J. Warnatz, M.E. Coltrin, and J.A. Miller, Report No. SAND 86-8246 (1986).

57. M.E. Coltrin and D.S. Dandy, J. Appl. Phys. **74**, 5803 (1993).

58. M. Okkerse, M.H.J.M. de Croon, C.R. Kleijn, H.E.A. van den Akker, and G.B. Marin, J. Appl. Phys. **84**, 6387 (1998).

59. D.S. Dandy and M.E. Coltrin, J. Appl. Phys. **76**, 3102 (1994).

60. H. Liu and D.S. Dandy, Diamond Chemical Vapor Deposition Nucleation and Early Growth Stages, (Noyes Publications, Park Ridge, NJ, 1995).

61. C. Wild, R. Kohl, N. Herres, W. Műller-Sebert, and P. Koidl, Diamond Relat. Mater. **3**, 373 (1994).

Reproduced with permission of the copyright owner. Further reproduction prohibited without permission.

Chapter 6

CONCULSIONS AND RECOMMENDATIONS

6.1 Overall Conclusions

The fundamental phenomena associated with nucleation and continuous film growth of covalent materials—including diamond, silicon carbide, and carbon nitride—in CVD processes has become subjects of intensive study in an effort to improve film characteristics such as crystallographic texture and surface morphology. This research involves a study of the nucleation and subsequent film growth of covalent materials through numerical modeling and simulations. Numerical models have been developed:

- to examine the chemical vapor deposition of polycrystalline carbon nitride in stagnation flow reactors.
- to investigate the formation of the β-SiC intermediate layer during nucleation and the early stages of diamond deposition in CVD reactors.
- to understand the polycrystalline growth of β-SiC films on Si (100) substrates in stagnation flow reactors.
- to study the crystallographic texture and surface morphology of diamond films deposited on pretreated Si substrates, including flat and stepped β-SiC layers, via a two-stage CVD process comprised of (1) diamond nucleation and (2) continuous film growth.

Reproduced with permission of the copyright owner. Further reproduction prohibited without permission.

6.1.1 Analysis of Carbon Nitride Growth in Pedestal Reactors by Chemical Vapor Deposition

The chemical vapor deposition of polycrystalline carbon nitride in stagnation flow reactors has been simulated. A model was used to predict the gas phase chemistry, temperature and velocity profiles, potential gaseous film growth precursors, and to evaluate the likelihood of bond rearrangement occurring in the bulk phase or on the deposition surface once the gaseous precursors are adsorbed. Numerical studies have been carried out to predict the effects of inlet and substrate temperatures, reactor pressure, and inlet gas composition on the gas phase chemistry. Potential gaseous film growth precursors of carbon nitride have been determined by quantitatively comparing the calculated results against existing experimental data.

Results of the model indicate that the gas phase chemistry, including the gas composition at the deposition surface, is strongly affected by reactor pressure and inlet gas composition. However, the gas composition at the deposition surface does not depend strongly on the inlet temperature, while it is found to be strongly dependent on the substrate temperature. Since no correlation is found between the predicted near-surface concentrations of potential film growth precursors and experimentally measured bond types in the carbon nitride films, the experimentally measured bond types in the films must therefore result from chemical bond rearrangement occurring on the deposition surface or in the bulk phase once the gaseous precursors have been adsorbed. Comparison between the calculated film growth rate using potential growth precursors and experimental data indicates that the C, CH_2, CH_3, C_2H_2, N, NH, NH_2, HCN, and H_2CN species are the most probable crystalline carbon nitride growth species. Among these, C and CH_3

Reproduced with permission of the copyright owner. Further reproduction prohibited without permission.

dominate the carbon contribution to the film growth, and N is the primary nitrogen bearing species responsible for the film growth. The sum of predicted film growth rates for carbon bearing species is comparable to the experimentally determined film growth rate.

6.1.2 A Kinetic Model of Diamond Nucleation and Silicon Carbide Interlayer Formation during Chemical Vapor Deposition

The presence of thin silicon carbide intermediate layers on silicon substrates during nucleation and the early stages of diamond deposition have been frequently reported. It is generally accepted that the intermediate layer is formed by the bulk diffusion of carbon atoms into the silicon carbide layer, and the morphology and orientation of the diamond film subsequently grown on the intermediate layer are strongly affected by that layer. While there have been considerable attempts to explain the mechanism for intermediate layer formation, limited quantitative data are available for the layer formation under the operating conditions conducive to diamond nucleation.

This study employs a kinetic model to predict the time evolution of a β-SiC intermediate layer under the operating conditions typical of diamond nucleation in hot filament chemical vapor deposition reactors. The evolution of the layer is calculated by accounting for gas-phase and surface reactions, surface and bulk diffusions, the mechanism for intermediate layer formation, and heterogeneous diamond nucleation kinetics and of its dependence on the operating conditions such as substrate temperature and inlet gas composition. A comparison between the time scales for intermediate layer growth and diamond nuclei growth is also performed. Discrepancies in published adsorption energies of gaseous hydrocarbon precursors on the intermediate layer—ranging from 1.43 to 4.61

Reproduced with permission of the copyright owner. Further reproduction prohibited without permission.

eV—are examined to determine the most reasonable value of the adsorption energy consistent with observed saturated thicknesses, 1 to10 nm, of the intermediate layer reported in the literature. The operating conditions that lead to intermediate layer growth followed by diamond deposition versus those that yield heteroepitaxial diamond nucleation without intermediate layer formation are discerned quantitatively.

The calculations show that higher adsorption energies, 3.45 and 4.61 eV, lead to larger surface number densities of carbon atoms, lower saturated nucleation densities, and larger intermediate layer thicknesses. The observed saturated thicknesses of the intermediate layer may be reproduced if the true adsorption energy is in the range 3.7 to 4.5 eV. The intermediate layer thickness increases by increasing substrate temperature and inlet hydrocarbon concentration, and the dependence of the thickness on substrate temperature is especially significant. Heteroepitaxial diamond nucleation without intermediate layer formation reported in experimental results can be readily explained by the significant decrease of the intermediate layer thickness at lower substrate temperatures and at higher diamond nucleation densities. Further, the present model results indicate that the intermediate layer thickness becomes saturated when growing diamond nuclei cover a very small surface area of that layer.

6.1.3 A Model of Morphology Evolution in the Growth of Polycrystalline β-SiC Films

The growth of β-SiC films via chemical vapor deposition (CVD) has been under intensive investigation because this is viewed to be an enabling material for a variety of new semiconductor devices in areas where silicon devices cannot effectively compete. However, the difficulty in achieving single-crystal or highly textured surface morphology

Reproduced with permission of the copyright owner. Further reproduction prohibited without permission.

in films with low bulk defect density has limited the use of β-SiC films in electronic devices. While several researchers have reported results relating the morphology of β-SiC films to deposition parameters, including substrate temperature and gas composition, detailed knowledge of the effects of deposition parameters on film morphology and crystallographic texture is still lacking. If these relationships between deposition parameters and film morphology can be quantified, then it may be possible to obtain optimal β-SiC film morphologies via CVD for specific applications such as electronic devices.

The purpose of this study is to predict the dependence of the surface morphology of β-SiC films grown by CVD on substrate temperature and inlet atom ratio of Si:C, and to model the morphological evolution of the growing polycrystalline film. The Si:C ratio is determined by the composition of the reactant gases, propane (C_3H_8) and silane (SiH_4). A two-dimensional numerical model based on growth rate parameters has been developed to predict the evolution of the surface morphology. The model calculates the texture, surface roughness, and grain size of continuous polycrystalline β-SiC films resulting from growth competition between nucleated seed crystals of known orientation. Crystals with the fastest growth direction perpendicular to the substrate surface are allowed to overgrow all other crystal orientations. When a continuous polycrystalline film is formed, the facet orientations of crystals are represented on the surface. In the model, the growth parameter, α_{2D}, the ratio of the growth rates of the {10} and {11} faces, determines the crystal shapes and, thus, the facet orientations of crystals. The growth rate parameter α_{2D} used in the model has been derived empirically from the textures of continuous β-SiC films reported in the literature.

Reproduced with permission of the copyright owner. Further reproduction prohibited without permission.

6.1.4 A Morphological Study of Diamond Films Deposited on Pretreated Si Substrates

This study focuses on the crystallographic texture and surface morphology of diamond films grown on pretreated Si substrates, including flat and stepped β-SiC layers, via a two-stage chemical vapor deposition process, comprised of (1) diamond nucleation and (2) film growth. A model is developed to provide a complete understanding of the dependence of diamond film characteristics—surface roughness, film texture and orientation, and grain size—on the differences in nucleation densities and operating conditions. The film characteristics are optimized by quantifying the dependence of film characteristics on the deposition conditions for diamond nucleation and film growth stages.

It is predicted that smooth, highly textured surfaces can be obtained by enhancing the saturated nucleation density on pretreated Si substrates. For film growth after diamond nucleation, the mean surface roughness of diamond films increases with increases in film thickness, and the value attains a maximum for two growth-rate parameters, 1.3 and 1.9. The growth-rate parameter, which is previously described in the chapter 3, is strongly dependent on operating conditions. However, the mean surface roughness increases monotonically for a growth-rate parameter of 1.6, and does not reach a maximum. Further, the mean surface roughness of thick films can be also reduced by decreasing the terminal diamond thickness during the nucleation stage. Using either a high growth-rate parameter of 1.9 or small terminal diamond thicknesses of 1 μm, predominantly {100}-faced epitaxial films with large grains can be prepared.

Reproduced with permission of the copyright owner. Further reproduction prohibited without permission.

6.2 Recommendations for Future Research

The nucleation and growth processes involved in the formation of thin films of covalent materials have been explored in this dissertation, and general principles of the covalent material deposition have been provided. Several aspects of those processes, however, still need to be resolved through more theoretical and experimental studies before more reproducible and predictable results can be obtained through a complete understanding of the detailed nucleation and growth mechanisms of covalent materials. Thus, future work should concentrate on the following aspects:

1. A more complete understanding of surface reactions, through extracting the information of thermodynamics and kinetics from suitable experiments and theories in combination, is needed to lead to the successful synthesis of β-C_3N_4 and other metastable carbon nitrides with well-crystallized phases.
2. Since the present model, which describes diamond nucleation and intermediate layer formation, does not explain the experimentally observed incubation period, the model improvement will help in estimating the incubation period before diamond nucleation begins and in controlling its magnitude with different operating conditions, substrate materials, and substrate surface conditions.
3. The model of diamond nucleation and intermediate layer formation needs to be modified to take into account processes occurring on time scales from ranging atomistic nucleation to continuous diamond film formation. Such a modified model will help to provide the information of the surface concentration change of single carbon atoms after the saturated nucleation density is attained. Further improvement

Reproduced with permission of the copyright owner. Further reproduction prohibited without permission.

of the model is needed to capture the time dependence of the crystal size distribution during the extended time scale.

4. Further work is required to validate assumptions in the model of diamond nucleation and intermediate layer formation, such as the values of the capture numbers, the sticking coefficients of hydrocarbon species with Si, C, and β-SiC surfaces, and the surface diffusion energies assumed to be one-half of hydrocarbon adsorption energies.
5. Although the present model does not capture the effects of surface coverage on the nucleation process, the influence of surface coverage on the nucleation parameters—including adsorption and desorption, sticking, and surface diffusion—needs to be better understood.
6. Theoretical development is needed to provide more complete descriptions of the equation that can predict the saturated nucleation density of covalent materials deposited on a variety of substrates, and as a result it may result in a single generalized equation computing the saturated nucleation density of covalent materials. For a variety of covalent materials, energy values of adsorption and surface diffusion can be exacted from experimental data for the saturated nucleation density.
7. A better understanding of the effects of surface defects on the nucleation process is needed to conduct the selected nucleation on pretreated and pre-patterned substrates with a very high nucleation density. Since the nucleation process sometimes comprises the deliberate use of a variety of substrate surface defects, the investigation of the nucleation of covalent materials on substrate surfaces with extended surface defects provides good opportunities to elucidate the detailed chemistry and physics

Reproduced with permission of the copyright owner. Further reproduction prohibited without permission.

of a complicated nucleation process and to improve the properties of polycrystalline covalent materials.

8. During diamond nucleation on a variety of substrates, the structure of the intermediate layer, as well as the dependence of the structure on operating conditions, substrate materials, and substrate surface conditions, should be determined.
9. The morphology evolution model should be extended to three dimensions for better control of morphology and crystallite grain structure in polycrystalline covalent materials.

Reproduced with permission of the copyright owner. Further reproduction prohibited without permission.